

CO Emission, Molecular Gas, and Metallicity in Main-sequence Star-forming Galaxies at $z \sim 2.3^*$

Ryan L. Sanders^{1,10} , Alice E. Shapley² , Tucker Jones¹ , Irene Shavai³ , Gergö Popping⁴ , Naveen A. Reddy⁵ , Romeel Davé⁶ , Sedona H. Price⁷ , Bahram Mobasher⁵, Mariska Kriek⁸ , Alison L. Coil⁹ , and Brian Siana⁵

¹ Department of Physics and Astronomy, University of California, Davis, One Shields Avenue, Davis, CA 95616, USA; rlsand@ucdavis.edu

² Department of Physics & Astronomy, University of California, Los Angeles, 430 Portola Plaza, Los Angeles, CA 90095, USA

³ Steward Observatory, University of Arizona, Tucson, AZ 85721, USA

⁴ European Southern Observatory, Karl-Schwarzschild-Str. 2, D-85748, Garching, Germany

⁵ Department of Physics & Astronomy, University of California, Riverside, 900 University Avenue, Riverside, CA 92521, USA

⁶ Institute for Astronomy, University of Edinburgh, James Clerk Maxwell Building, Peter Guthrie Tait Road, Edinburgh, EH9 3FD, UK

⁷ Max-Planck-Institut für Extraterrestrische Physik, Postfach 1312, Garching, D-85741, Germany

⁸ Leiden Observatory, Leiden University, P.O. Box 9513, NL-2300 AA Leiden, The Netherlands

⁹ Center for Astrophysics and Space Sciences, University of California, San Diego, 9500 Gilman Drive, La Jolla, CA 92093-0424, USA

Received 2022 April 11; revised 2022 October 25; accepted 2022 November 18; published 2023 January 3

Abstract

We present observations of CO(3–2) in 13 main-sequence $z = 2.0$ –2.5 star-forming galaxies at $\log(M_*/M_\odot) = 10.2$ –10.6 that span a wide range in metallicity (O/H) based on rest-optical spectroscopy. We find that $L'_{\text{CO}(3-2)}/\text{SFR}$ decreases with decreasing metallicity, implying that the CO luminosity per unit gas mass is lower in low-metallicity galaxies at $z \sim 2$. We constrain the CO-to-H₂ conversion factor (α_{CO}) and find that α_{CO} inversely correlates with metallicity at $z \sim 2$. We derive molecular gas masses (M_{mol}) and characterize the relations among M_* , SFR, M_{mol} , and metallicity. At $z \sim 2$, M_{mol} increases and the molecular gas fraction (M_{mol}/M_*) decreases with increasing M_* , with a significant secondary dependence on SFR. Galaxies at $z \sim 2$ lie on a near-linear molecular KS law that is well-described by a constant depletion time of 700 Myr. We find that the scatter about the mean SFR– M_* , O/H– M_* , and $M_{\text{mol}}-M_*$ relations is correlated such that, at fixed M_* , $z \sim 2$ galaxies with larger M_{mol} have higher SFR and lower O/H. We thus confirm the existence of a fundamental metallicity relation at $z \sim 2$, where O/H is inversely correlated with both SFR and M_{mol} at fixed M_* . These results suggest that the scatter of the $z \sim 2$ star-forming main sequence, mass–metallicity relation, and $M_{\text{mol}}-M_*$ relation are primarily driven by stochastic variations in gas inflow rates. We place constraints on the mass loading of galactic outflows and perform a metal budget analysis, finding that massive $z \sim 2$ star-forming galaxies retain only 30% of metals produced, implying that a large mass of metals resides in the circumgalactic medium.

Unified Astronomy Thesaurus concepts: Molecular gas (1073); CO line emission (262); High-redshift galaxies (734); Galaxy evolution (594); Metallicity (1031)

1. Introduction

The cold gas mass and abundance of heavy elements (i.e., metallicity) are fundamental properties of galaxies that are key to understanding galaxy formation and evolution. Molecular gas clouds are the sites of star formation such that galaxy star formation rates (SFRs) depend on the mass of molecular gas (M_{mol}) available in the interstellar medium (ISM). This close tie is manifested in a tight correlation between the surface densities of SFR (Σ_{SFR}) and molecular gas mass (Σ_{mol}) known as the molecular Kennicutt–Schmidt relation (e.g., Kennicutt 1998; Bigiel et al. 2008; Leroy et al. 2008; de los Reyes & Kennicutt 2019; Kennicutt & De Los Reyes 2021). Likewise, metallicity is connected to star formation as new metals are

produced via nucleosynthesis and returned to the ISM through the processes of stellar evolution and death, such that the trend of increasing metallicity over time traces the buildup of galaxy stellar mass (M_*).

Galaxy-integrated SFR, metallicity, and M_{mol} have been found to depend strongly on M_* in star-forming populations, resulting in a number of scaling relations: the star-forming main sequence (MS) in which SFR increases with increasing M_* (e.g., Brinchmann et al. 2004; Noeske et al. 2007); the mass–metallicity relation (MZR) in which ISM metallicity, traced by the gas-phase oxygen abundance, increases with increasing M_* (e.g., Tremonti et al. 2004; Andrews & Martini 2013; Curti et al. 2020); and the $M_{\text{mol}}-M_*$ relation in which more massive galaxies have larger molecular gas reservoirs (e.g., Bothwell et al. 2014; Saintonge et al. 2017). At $z \sim 0$, these scaling relations display secondary dependences that connect these properties in three-dimensional parameter spaces. At fixed M_* , O/H decreases with increasing SFR, forming the SFR–O/H– M_* “Fundamental Metallicity Relation” (SFR–FMR; e.g., Mannucci et al. 2010; Cresci et al. 2019; Curti et al. 2020). Similarly, O/H and M_{mol} are inversely related at fixed M_* in the $M_{\text{mol}}-O/H-M_*$ relation, or “Gas–FMR” (Bothwell et al. 2016a, 2016b). A Gas–FMR has also been found at $z \sim 0$ using atomic hydrogen gas masses (Bothwell et al. 2013; Hughes et al. 2013; Lara-Lopez et al. 2013; Brown et al. 2018). Because SFR is determined by the amount of cold gas

* The data presented herein were obtained at the W. M. Keck Observatory, which is operated as a scientific partnership among the California Institute of Technology, the University of California, and the National Aeronautics and Space Administration. The Observatory was made possible by the generous financial support of the W. M. Keck Foundation.

¹⁰ NHFP Hubble Fellow.

present, it is likely that the Gas–FMR is a more fundamental relation from which the SFR–FMR emerges. These higher-order relations are realized as correlated scatter around pairs of scaling relations: the SFR–FMR is represented by an anticorrelation between residuals around the MS and residuals around the MZR, while a signature of the Gas–FMR is that residuals around the $M_{\text{mol}}-M_*$ relation are anticorrelated with those about the MZR.

Characterizing the interrelation between M_* , SFR, M_{mol} , and metallicity is of central importance to understanding the cycle of baryons that governs galaxy growth. The class of gas-regulator, equilibrium, or bathtub models of galaxy formation indicate that the gas fraction (M_{gas}/M_*) and ISM metallicity of a galaxy is governed by the rates of gas accretion (\dot{M}_{in}) and outflow (\dot{M}_{out}) relative to the SFR (e.g., Peebles & Shankar 2011; Davé et al. 2012; Lilly et al. 2013; Peng & Maiolino 2014), such that the mass-loading factor of outflows ($\eta_{\text{out}} = \dot{M}_{\text{in}}/\text{SFR}$) can be constrained using measurements of both metallicity and gas fraction. Such models suggest that the SFR–FMR and Gas–FMR arise as a direct result of baryon cycling. Freshly accreted unenriched gas will expand the gas reservoir, leading to a larger SFR, while simultaneously diluting metals in the ISM, leading to lower O/H. The SFR–FMR and Gas–FMR are also ubiquitous features of numerical simulations of galaxy formation in a cosmological context that include feedback (e.g., Davé et al. 2017; De Rossi et al. 2017; Torrey et al. 2018; Davé et al. 2019; Torrey et al. 2019). The existence of both an SFR–FMR and a Gas–FMR, and the associated correlated residuals around scaling relations, is thus a signature of a self-regulated baryon cycle governing galaxy growth.

Searching for the SFR–FMR and Gas–FMR at high redshift presents an opportunity to understand baryon cycling during an epoch when galaxy formation was proceeding rapidly, when gas inflows and outflows are expected to be more intense than locally on average. There has been great progress in characterizing metallicity scaling relations at high redshift in the past several years, thanks to extensive rest-optical spectroscopic surveys of representative star-forming galaxies at $z \sim 1-3$ (e.g., Steidel et al. 2014; Kriek et al. 2015; Momcheva et al. 2016; Kashino et al. 2019). The MZR has been found to exist out to $z \sim 3.5$, evolving toward lower O/H at fixed M_* with increasing redshift (e.g., Erb et al. 2006a; Maiolino et al. 2008; Cullen et al. 2014; Troncoso et al. 2014; Sanders et al. 2015; Cullen et al. 2021; Sanders et al. 2021; Topping et al. 2021). The existence of an SFR–FMR has also been confirmed at $z = 1.5-2.5$ (Zahid et al. 2014; Sanders et al. 2018; Henry et al. 2021; Sanders et al. 2021).

M_{mol} is commonly inferred from indirect tracers, including CO line emission and dust continuum emission. The former requires a conversion factor between CO luminosity and M_{mol} (α_{CO} ; e.g., Wolfire et al. 2010; Schruba et al. 2012; Bolatto et al. 2013; Accurso et al. 2017), while the latter requires an assumed dust-to-gas ratio (e.g., Sandstrom et al. 2013; De Vis et al. 2019) or an empirical calibration between Rayleigh–Jeans tail dust emission and M_{mol} (Scoville et al. 2016). These conversion factors have been found to depend strongly on ISM metallicity in the local universe, such that knowledge of the metallicity is key to accurate inferences of M_{mol} . Progress in understanding the cold gas properties of high-redshift galaxies has been challenging due to the difficulty of detecting these tracers at cosmological redshifts.

CO line emission is the most common tracer of molecular gas in the nearby universe, but has proven difficult to measure in high-redshift main-sequence galaxies. Early work at $z > 1$ was limited to extreme sources including submillimeter galaxies (SMGs) and ultraluminous infrared galaxies (ULIRGs; e.g., Greve et al. 2005; Tacconi et al. 2008), and more typical galaxies could only be reached with strong gravitational lensing (Baker et al. 2004; Coppin et al. 2007; Danielson et al. 2011; Saintonge et al. 2013). The sensitive IRAM NOEMA interferometer enabled targeted surveys to reach main-sequence galaxies at $z \sim 1-2$ (Daddi et al. 2010; Magnelli et al. 2012; Daddi et al. 2015), culminating with the PHIBSS survey that measured CO for ~ 50 main-sequence galaxies at $z = 1-2.5$ (Tacconi et al. 2010, 2013, 2018).

More recently, the Atacama Large Millimeter Array (ALMA) has provided further improvement in sensitivity at millimeter wavelengths. Using ALMA, the ASPECS blind spectral scan survey has detected CO(3–2) and CO(2–1) for dozens of main-sequence galaxies at $z = 1-3$ in the Hubble Ultra Deep Field (Boogaard et al. 2019; Decarli et al. 2019; González-López et al. 2019), while targeted campaigns measured CO for a number of other $z > 1$ galaxies (e.g., Silverman et al. 2015, 2018). Main-sequence CO(1–0) detections at $z = 2-3$ have also been obtained with deep VLA observations (Pavesi et al. 2018; Riechers et al. 2020). However, these existing samples of main-sequence CO-detected galaxies at high redshift still only probe the most massive main-sequence galaxies, with nearly all targets at $z > 2$ having stellar masses above $10^{10.7} M_\odot$. This fact highlights an important disconnect between high-redshift galaxies with cold gas information and the large samples at $z \sim 1-3$ with detailed rest-optical spectroscopy spanning $\log(M_*/M_\odot) = 9.0-10.5$, for which robust metallicity constraints are available. It is necessary to obtain CO observations of lower-mass galaxies that are more typical of high-redshift star-forming populations, and critically, that have metallicity measurements, in order to search for a Gas–FMR at high redshift, improve constraints on baryon cycling in early galaxies, and understand how to reliably estimate M_{mol} in main-sequence high-redshift galaxies when CO and dust tracers are not available.

In this work, we analyze CO(3–2) observations obtained with ALMA for 13 near main-sequence galaxies at $z \sim 2.3$ with a mean stellar mass of $10^{10.4} M_\odot$. These targets also have deep rest-optical spectroscopy from the MOSDEF survey (Kriek et al. 2015), providing robust determinations of gas-phase metallicity and SFR. This unique combination of measurements allows us to carry out a systematic analysis of the relations among M_* , SFR, M_{mol} , and metallicity for typical star-forming galaxies at $z \sim 2$, and to place constraints on gas flows and baryon cycling in these early galaxies.

This paper is organized as follows. In Section 2, we present the observations and describe how derived properties are calculated. The results are presented in Section 3. The sample properties are described in Section 3.1. Empirical relations between CO(3–2) luminosity and galaxy properties are explored in Section 3.2. We place constraints on the relation between α_{CO} and O/H at $z \sim 2$ in Section 3.3. In Section 3.4, we derive molecular gas masses and characterize the relationships between M_* , SFR, M_{mol} , and metallicity. We discuss these results in Section 4, and we summarize our conclusions in Section 5.

Throughout, we assume a standard Λ CDM cosmology with $H_0 = 70 \text{ km s}^{-1} \text{ Mpc}^{-1}$, $\Omega_m = 0.3$, and $\Omega_\Lambda = 0.7$. Magnitudes are in the AB system (Oke & Gunn 1983) and wavelengths are given in air. Stellar masses and SFRs are on the Chabrier (2003) initial mass function (IMF) scale. The term metallicity refers to the gas-phase oxygen abundance unless otherwise stated, where solar metallicity is $12 + \log(\text{O/H})_\odot = 8.69$ (Asplund et al. 2021). Molecular gas masses include a 36% contribution from helium and metals.

2. Observations

2.1. Sample Selection and Rest-optical Spectroscopic Observations

Our sample was selected from the MOSFIRE Deep Evolution Field (MOSDEF) survey (Kriek et al. 2015), a deep near-infrared (rest-frame optical) spectroscopic survey of ~ 1500 galaxies at $1.4 \leq z \leq 3.8$ using the MOSFIRE instrument (McLean et al. 2012) on the 10 m Keck I telescope. Survey targets were selected in the five CANDELS extragalactic legacy fields (Grogin et al. 2011; Koekemoer et al. 2011) from the photometric catalogs of the 3D-HST survey (Brammer et al. 2012; Skelton et al. 2014; Momcheva et al. 2016) down to fixed H -band magnitude measured from HST/WFC3 F160W imaging in three redshift intervals, with limits of $H_{\text{AB}} \leq 24.0$, 24.5, and 25.0 for targets at $1.37 \leq z \leq 1.70$, $2.09 \leq z \leq 2.61$, and $2.95 \leq z \leq 3.80$, respectively. These redshift intervals were chosen such that the strong rest-frame optical emission lines $[\text{O II}]\lambda\lambda 3726, 3729$, $\text{H}\beta$, $[\text{O III}]\lambda\lambda 4959, 5007$, $\text{H}\alpha$, $[\text{N II}]\lambda 6584$, and $[\text{S II}]\lambda\lambda 6716, 6731$ fall in windows of atmospheric transmission in the near-infrared. Targets were selected based on pre-existing spectroscopic or HST grism redshifts when available, and photometric redshifts otherwise. The completed MOSDEF survey measured robust redshifts for ~ 1300 targeted galaxies. See Kriek et al. (2015) for a full description of the survey design, observations, and data reduction.

Using the MOSDEF catalogs, we selected a sample of 14 star-forming galaxies in the middle redshift interval at $z \sim 2.3$, where the CO(3–2) emission line can be observed in Band 3 with ALMA. Targets were required to be in the COSMOS field for accessibility with ALMA, have spectroscopic redshifts in the range $2.0 \leq z \leq 2.6$, have detections at $\text{S/N} \geq 3$ for the $\text{H}\beta$, $[\text{O III}]\lambda 5007$, $\text{H}\alpha$, and $[\text{N II}]\lambda 6584$ lines to ensure robust metallicity and SFR constraints, and have stellar masses within ± 0.1 dex of $\log(M_*/M_\odot) = 10.5$.¹¹ Active galactic nuclei (AGN) were removed from the sample, having been identified based on their X-ray and IR properties (Coil et al. 2015; Azadi et al. 2017, 2018; Leung et al. 2019) and when $\log([\text{N II}]/\text{H}\alpha) > -0.3$. This selection yielded a sample of 14 star-forming galaxies at $z = 2.08\text{--}2.47$ for follow-up ALMA observations, the properties of which are presented in Table 1.

2.2. ALMA Observations and CO(3–2) Measurements

These 14 targets were observed in ALMA Cycle 6 Program 2018.1.01128.S (PI: R. Sanders) with the Band 3 receiver in 21

scheduling blocks over 2018 November 7 to 2018 December 29. The observations were designed such that the CO(3–2) line ($\nu_{\text{rest}} = 345.796 \text{ GHz}$) fell within one spectral window in Band 3, between 99 and 113 GHz at the redshifts of our targets. The requested spectral configuration provided a bandpass of 1.875 GHz per spectral window with a native resolution of 7.8125 MHz, corresponding to $\approx 22 \text{ km s}^{-1}$ at $z \sim 2.3$. Observations were carried out with 43 12 m antennas in the C43-3 to C43-5 configurations, providing beam major axes of $0''.7\text{--}2''.5$ with a mean beam size of $1''.5$. On-source integration times were 10–170 minutes per target reaching sensitivities of $86\text{--}456 \mu\text{Jy beam}^{-1}$ integrated over 50 km s^{-1} .

The ALMA data were calibrated and imaged using the Common Astronomy Software Applications (CASA) package (McMullin et al. 2007). We utilized flux, phase, and bandpass-calibrated measurement sets provided by the North American ALMA Regional Center at NRAO. The CASA task TCLEAN was used to produce clean imaged data cubes with a velocity resolution of 50 km s^{-1} ($\approx 1/3$ of the rest-optical line FWHM; Price et al. 2016) using natural weighting. We searched for detections by collapsing the channels within $\pm 200 \text{ km s}^{-1}$ of the systemic redshift determined from the rest-optical lines and searching for positive peaks in these moment-zero maps exceeding 3σ at the spatial location of each target galaxy. Figure 1 shows CO(3–2) contours superposed on HST false-color images for our sample (top panel of each subplot). We found CO(3–2) emission is robustly detected in six targets with peak $\text{S/N} > 5$ in the moment-zero maps, tentatively detected in two targets with peak $\text{S/N} = 3\text{--}4$, and not detected in the remaining six targets.

For all detected sources, we perform optimal extractions to produce one-dimensional science spectra (Horne 1986) after converting the data cube intensity units from Jy/beam to Jy/pixel using the beam size in each frequency channel. All but one source (ID 3324) have spatial profiles that are consistent with being unresolved. We extract these targets as point sources using a two-dimensional Gaussian profile set by the beam shape. Spectra of nondetections are extracted using a point source profile at the target centroid location from HST/WFC3 F160W imaging (rest-optical). Employing boxcar extractions yields consistent results with slightly larger uncertainties. The extracted 1D CO(3–2) spectra are displayed in the bottom panels of each subplot in Figure 1.

ID 3324 presents an unusual spatial profile with two peaks separated by ≈ 1 beamwidth ($1''.5$). Spectra extracted separately at each peak location yield 1D lines with roughly comparable fluxes and velocity centroids that are consistent with one another and the rest-optical redshift at less than the 1σ level. To evaluate whether the second peak may be spurious, we searched the data cube for negative peaks with significance equal to or greater than that of the second peak when integrating over the same velocity interval. We found two negative peaks at $\geq 5.3\sigma$, while the second peak of ID 3324 is the only positive feature in the data cube with this significance, indicating it is possible that the second peak is due to noise. However, the probability of such a noise fluctuation aligning with our target both spatially and spectrally, with a frequency matching the known spectroscopic redshift, must be very small. We thus cannot conclude whether the second peak of ID 3324 is spurious without deeper observations. We proceed by including the total line flux from both peaks by extracting ID 3324 using a spatial profile of two point sources aligned

¹¹ The stellar masses used to select the sample observed with ALMA were not corrected for the contribution of strong emission lines to the broadband photometry. The stellar masses used in this paper have been derived from emission line corrected photometry (Sanders et al. 2021). Accordingly, the final stellar mass range differs slightly from that originally used in target selection.

Table 1
Galaxy Properties, CO(3–2) Measurements, and Derived Molecular Gas Properties of the MOSDEF-ALMA Sample and Composite Spectra

ID	R.A. J2000	Decl J2000	t_{int} hr	$\frac{\text{rms}}{\text{Jy}}$ $\frac{\text{beam}}$	z_{spec}	$\log\left(\frac{M_*}{M_\odot}\right)$	$\log\left(\frac{\text{SFR}}{M_\odot \text{ yr}^{-1}}\right)$	12+log(O/H)	R_{eff} kpc	$S_{\text{CO(3–2)}}$ Jy km s $^{-1}$	$\log(L'_{\text{CO(3–2)}})$	$\log\left(\frac{M_{\text{mol}}}{M_\odot}\right)$	$\log(\mu_{\text{mol}})$
13296	10:00:27.623	+02:18:55.05	2.82	88	2.1672	10.40 ± 0.04	1.46 ± 0.16	8.81 ± 0.03	3.4	0.139 ± 0.026	9.54 ± 0.08	10.44 ± 0.08	0.04 ± 0.09
19753 ^a	10:00:18.182	+02:22:50.32	0.83	198	2.4694	10.33 ± 0.08	1.83 ± 0.04	...	4.1	0.250 ± 0.051	9.90 ± 0.09
13701 ^b	10:00:27.052	+02:19:09.98	2.82	86	2.1659	10.57 ± 0.04	2.19 ± 0.10	8.81 ± 0.02	4.1	0.147 ± 0.032	9.57 ± 0.10	10.46 ± 0.10	-0.11 ± 0.11
2672	10:00:31.073	+02:12:25.91	1.36	143	2.3074	10.50 ± 0.05	1.99 ± 0.16	8.61 ± 0.03	4.1	0.207 ± 0.047	9.77 ± 0.10	10.80 ± 0.10	0.30 ± 0.11
5094	10:00:33.688	+02:13:48.67	0.64	174	2.1715	10.34 ± 0.01	1.88 ± 0.27	8.71 ± 0.06	5.0	0.298 ± 0.076	9.88 ± 0.11	10.77 ± 0.11	0.43 ± 0.11
3324	10:00:35.618	+02:12:47.280	0.87	192	2.3072	10.55 ± 0.01	1.80 ± 0.15	8.84 ± 0.03	4.8	0.302 ± 0.079	9.93 ± 0.12	10.82 ± 0.12	0.27 ± 0.12
19985	10:00:14.484	+02:22:57.98	0.23	322	2.1882	10.20 ± 0.07	2.29 ± 0.04	8.36 ± 0.01	1.3	0.219 ± 0.079	9.75 ± 0.16	11.19 ± 0.16	0.99 ± 0.18
24763	10:00:13.608	+02:26:04.786	1.50	154	2.4649	10.46 ± 0.05	1.32 ± 0.13	8.66 ± 0.06	5.1	0.081 ± 0.035	9.41 ± 0.20	10.36 ± 0.20	-0.10 ± 0.21
20062	10:00:16.436	+02:23:00.79	0.45	254	2.1857	10.24 ± 0.04	2.36 ± 0.03	8.49 ± 0.01	1.5	<0.159	<9.61	<10.84	<0.60
3666	10:00:18.607	+02:12:57.72	0.39	265	2.0859	10.25 ± 0.04	1.94 ± 0.05	8.45 ± 0.01	3.6	<0.268	<9.80	<11.09	<0.84
4497	10:00:17.153	+02:13:25.94	0.72	193	2.4413	10.35 ± 0.00	1.98 ± 0.14	8.65 ± 0.03	3.1	<0.154	<9.68	<10.65	<0.30
4930	10:00:29.037	+02:13:43.66	1.18	154	2.2265	10.44 ± 0.05	1.74 ± 0.20	8.63 ± 0.06	5.7	<0.120	<9.50	<10.50	<0.06
5814	10:00:40.591	+02:14:18.22	0.16	456	2.1266	10.48 ± 0.04	2.14 ± 0.07	8.72 ± 0.02	4.7	<0.298	<9.86	<10.76	<0.28
9971	10:00:34.449	+02:16:54.47	0.57	218	2.4108	10.26 ± 0.05	2.01 ± 0.06	8.55 ± 0.01	1.7	<0.163	<9.70	<10.83	<0.57

Composite Spectra

name	bin	N_{gal}	z_{spec}	$\log\left(\frac{M_*}{M_\odot}\right)$	$\log\left(\frac{\text{SFR}}{M_\odot \text{ yr}^{-1}}\right)$	12+log(O/H)	R_{eff}	$S_{\text{CO(3–2)}}$	$\log(L'_{\text{CO(3–2)}})$	$\log\left(\frac{M_{\text{mol}}}{M_\odot}\right)$	$\log(\mu_{\text{mol}})$
stack-all	...	13	2.250	10.39 ± 0.03	1.93 ± 0.09	8.64 ± 0.04	3.7	0.158 ± 0.018	9.63 ± 0.05	10.61 ± 0.05	0.22 ± 0.06
stack-nondet	...	8	2.266	10.33 ± 0.03	1.97 ± 0.09	8.56 ± 0.04	3.3	0.144 ± 0.030	9.59 ± 0.09	10.70 ± 0.10	0.37 ± 0.10
stack-oh	low	6	2.234	10.31 ± 0.05	2.05 ± 0.10	8.51 ± 0.04	3.0	0.146 ± 0.030	9.59 ± 0.09	10.79 ± 0.09	0.48 ± 0.10
stack-oh	high	7	2.264	10.45 ± 0.04	1.83 ± 0.13	8.74 ± 0.03	4.3	0.173 ± 0.024	9.67 ± 0.06	10.56 ± 0.06	0.11 ± 0.07
stack-delsfms	low	6	2.274	10.45 ± 0.03	1.70 ± 0.13	8.71 ± 0.04	4.7	0.165 ± 0.022	9.66 ± 0.06	10.55 ± 0.06	0.10 ± 0.07
stack-delsfms	high	7	2.229	10.34 ± 0.05	2.13 ± 0.07	8.58 ± 0.06	2.9	0.154 ± 0.031	9.61 ± 0.09	10.69 ± 0.09	0.35 ± 0.11

Notes. ID numbers are from the 3D-HST v4.1 photometric catalog (Momcheva et al. 2016). The rms value gives the noise per beam over a bandwidth of 50 km s^{-1} at the frequency of the CO(3–2) line. All metallicities are based on O3O2Ne3 except for those of IDs 5094, 4930, and 24763 that use O3N2. $L'_{\text{CO(3–2)}}$ is in units of $M_\odot (\text{K km s}^{-1} \text{ pc}^2)^{-1}$. M_{mol} and μ_{mol} are calculated assuming the $\alpha_{\text{CO}}(\text{O/H})$ relation of Accurso et al. (2017; see Section 3.3 and Equation (13)). CO(3–2) fluxes, luminosities, and derived gas properties are given as 3σ upper limits for undetected sources. The z_{spec} , $\log(M_*)$, $\log(\text{SFR})$, 12+log(O/H), and R_{eff} assigned to each stack are the mean values of the individual galaxies.

^a The rest-optical lines and CO(3–2) emission likely originate from different components of ID 19753. As such, we do not report the metallicity or calculate M_{mol} or μ_{mol} for this object (see Section 2.2).

^b The CO(3–2) spectrum of ID 13701 was extracted from the data cube targeting ID 13296.

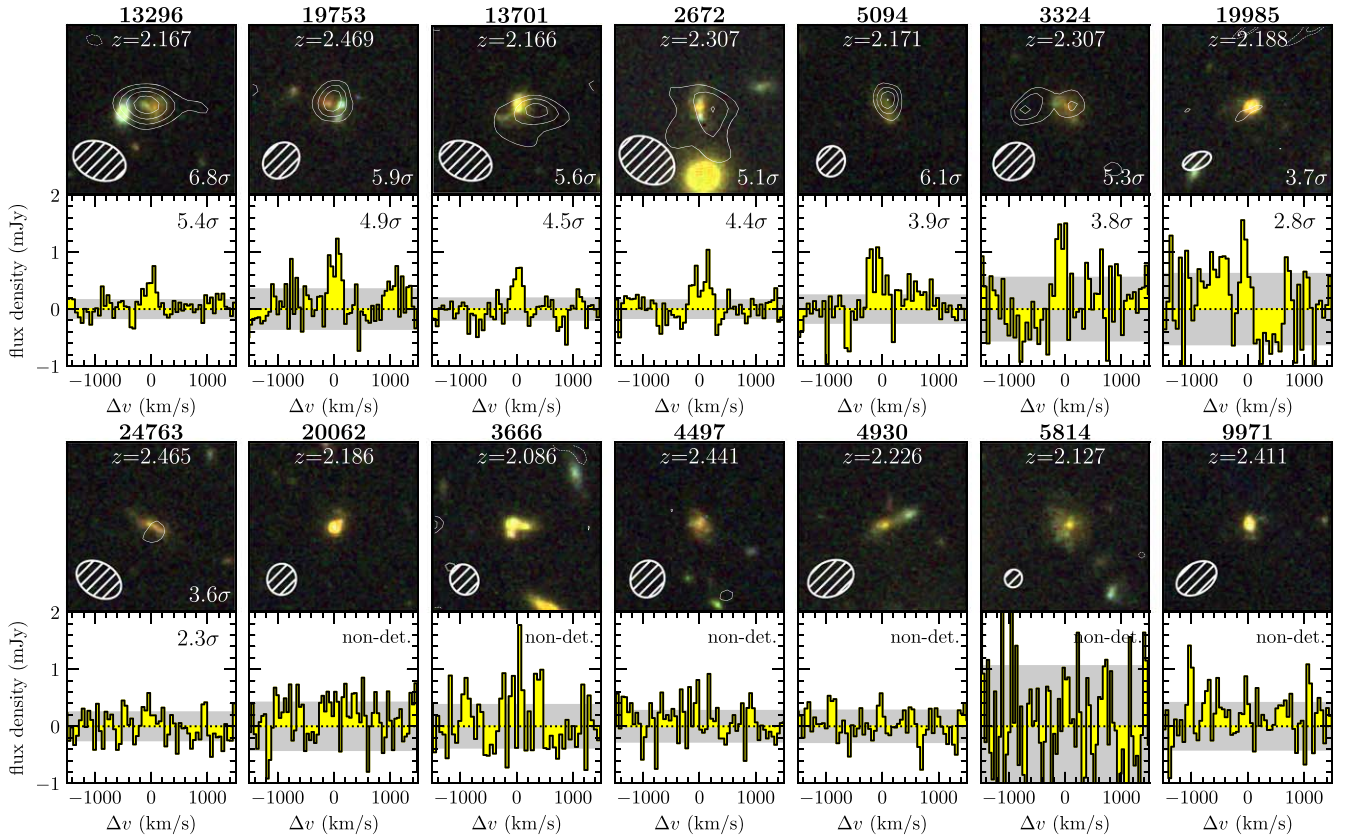


Figure 1. ALMA CO(3–2) observations for the 14 sources in our sample at $z = 2.08$ – 2.47 , sorted by decreasing integrated CO(3–2) S/N. The top panel of each subplot displays a HST false-color image (red = F160W; green = F125W; blue = F814W) overlaid with CO(3–2) S/N contours (white), with solid lines denoting positive values starting at $+3$ in steps of 1 and dashed lines showing negative values starting at -3 in steps of -1 . The beam shape at line center is shown in the lower left corner, and the peak CO(3–2) S/N is given in the lower right corner. The bottom panel presents the extracted 1D spectrum, with the rms noise displayed by the gray shaded region and the integrated CO(3–2) S/N given in the upper right corner for robust and tentative detections.

with the two peak locations, but note that our results in Section 3 do not significantly change if we exclude ID 3324 entirely or only include the CO(3–2) flux from the peak that is more spatially coincident with the HST imaging centroid.

Integrated CO(3–2) line fluxes are measured by fitting single Gaussian profiles to the extracted 1D spectra, with the uncertainty on the flux estimated from the covariance matrix. For nondetections, we fit a single Gaussian where the velocity width is fixed to be the same as that of the strong rest-optical lines ($\text{H}\alpha$ and $[\text{O III}]\lambda 5007$) and the centroid is allowed to vary $\pm 50 \text{ km s}^{-1}$ from the systemic redshift. The resulting uncertainties are used to infer 3σ upper limits on the CO(3–2) flux. Employing bandpass integrations or double Gaussian profiles for sources that may be spectrally double-peaked (IDs 19753 and 2672) yields line fluxes that are consistent within the uncertainties with the single Gaussian values. The six robust detections have integrated CO(3–2) S/N = 3.8 – 5.4 , while the two tentatively detected lines have significances of 2.8σ and 2.3σ .

One source, ID 19753, is robustly detected in CO(3–2) but is not included in the analysis, because of ambiguity in whether the rest-optical line emission is associated with the region dominating the CO(3–2) emission. ID 19753 displays a clumpy morphology with two dominant components displaying a large color difference, with a red clump to the east and a blue western clump that dominates the UV. It is probable that the rest-optical line emission originates from the UV-bright blue component, given that the $\text{H}\alpha/\text{H}\beta$ ratio implies relatively low

nebular reddening ($E(B-V)_{\text{gas}} = 0.16$). Dust continuum emission from ALMA Band 6 observations are offset from the blue component and are more spatially coincident with the red component (Shivaei et al. 2022). Due to the large beam size of the Band 3 observations, we cannot determine whether the CO(3–2) emission is co-spatial with the blue or red component, though it is likely that the CO emission aligns with the dust emission. Given the likelihood of the CO(3–2) and rest-optical lines of ID 19753 arising from distinct spatial components, we remove this source and proceed with a final sample of 13 galaxies.

2.3. Redshifts, Line Ratios, and SFRs

Rest-optical emission line fluxes are measured by fitting Gaussian line profiles to the slit-loss-corrected 1D science spectra from the MOSDEF survey (Kriek et al. 2015). $[\text{Ne III}]\lambda 3869$, $\text{H}\beta$, $[\text{O III}]\lambda 4959$, and $[\text{O III}]\lambda 5007$ are fit independently with single Gaussian profiles. The $[\text{O II}]\lambda\lambda 3726, 3729$ doublet is fit with a double Gaussian with the same line width for each component and a rest-frame offset between the two lines fixed to the expected value of 2.78 \AA . The $[\text{S II}]\lambda\lambda 6716, 6731$ doublet is fit simultaneously with a double Gaussian, but with independent line parameters for each component. $\text{H}\alpha$ and $[\text{N II}]\lambda\lambda 6548, 6584$ are fit simultaneously with a triple Gaussian where the widths of the three lines are tied but the $[\text{N II}]$ centroids can vary slightly from their expected position relative to $\text{H}\alpha$. In all cases, the continuum is set to the best-fit model from SED fitting such that stellar

Balmer absorption is accounted for in the best-fit $\text{H}\alpha$ and $\text{H}\beta$ fluxes. Systemic redshifts are inferred from the best-fit centroids of the highest-S/N line ($\text{H}\alpha$ or $[\text{O III}]\lambda 5007$).

Emission line fluxes are corrected for the effects of dust by using the $\text{H}\alpha/\text{H}\beta$ ratio to calculate $E(B-V)_{\text{gas}}$, assuming an intrinsic ratio of 2.86 (Osterbrock & Ferland 2006) and the Milky Way extinction curve of Cardelli et al. (1989). Reddy et al. (2020) derived a nebular attenuation curve directly from $z \sim 2$ MOSDEF measurements that is consistent with the Milky Way curve. All emission line ratios utilized for metallicity estimates are calculated using dust-corrected line fluxes. Star formation rates (SFRs) are derived from dust-corrected $\text{H}\alpha$ luminosities using the $\text{H}\alpha$ conversion factor of Hao et al. (2011) adjusted to a Chabrier (2003) IMF. The star formation rate surface density is calculated as $\Sigma_{\text{SFR}} = \text{SFR}/2\pi R_{\text{eff}}^2$, where R_{eff} is the rest-optical half-light elliptical semimajor axis derived from HST/WFC3 F160W imaging as cataloged by van der Wel et al. (2014). We define the offset from the star-forming main sequence at fixed M_* as a function of redshift as $\Delta \log(\text{SFR})_{\text{MS}} \equiv \log(\text{SFR}/\text{SFR}_{\text{MS}}(M_*, z))$, where we adopt the $\text{SFR}_{\text{MS}}(M_*, z)$ parameterization of Speagle et al. (2014), which matches the mean SFR– M_* relation of MOSDEF star-forming galaxies at $z \sim 2.3$ and $z \sim 3.3$ (Sanders et al. 2021).

2.4. Stellar Masses

Stellar masses are derived from spectral energy distribution (SED) fitting of the extensive broadband photometry in the COSMOS field from the 3D-HST survey catalogs (Skelton et al. 2014; Momcheva et al. 2016). Photometry was fit using the SED fitting code FAST (Kriek et al. 2009) in combination with the flexible stellar population synthesis models of Conroy et al. (2009), assuming constant star formation histories, solar stellar metallicity, a Chabrier (2003) IMF, and a Calzetti et al. (2000) attenuation curve. Because these models do not include a nebular emission component, photometric measurements were corrected for the contribution of strong rest-optical emission lines prior to fitting as described in Sanders et al. (2021), a necessary step due to the large emission line equivalent widths common at $z > 2$ (Reddy et al. 2018). Correcting the broadband photometry results in lower stellar masses by 0.12 dex on average in our sample. The two galaxies with the highest rest-optical equivalent widths have mass estimates reduced by 0.35 dex. The resulting best-fit stellar continuum model is used in the emission line fitting, as described above.

2.5. Gas-phase Metallicities

Gas-phase metallicities, given as $12 + \log(\text{O/H})$, are derived from reddening-corrected rest-frame optical line ratios. We employ metallicity calibrations derived from composite spectra of extreme local galaxies that are analogs of $z \sim 2$ galaxies from Bian et al. (2018). The functional form of the calibrations we use are given in Appendix A and Table A1. These calibrations reflect the significant evolution of H II region ionization conditions between $z \sim 0$ and $z > 1$ (e.g., Steidel et al. 2014; Shapley et al. 2015; Sanders et al. 2016; Steidel et al. 2016; Strom et al. 2017, 2018; Shapley et al. 2019; Sanders et al. 2020a; Topping et al. 2020a, 2020b; Runco et al. 2020) and provide a good match to the existing sample of $z > 1$ galaxies with direct-method metallicities (Sanders et al. 2020b). Because we are interested in measuring O/H, we consider

metallicities based on line ratios involving α elements (i.e., O, Ne) to be more robust than those involving N, since N/O has a large scatter at fixed O/H in H II regions and galaxies (~ 0.2 dex; e.g., Pilyugin & Thuan 2011; Strom et al. 2017), due to the differing nucleosynthetic production channels of N and α elements. Accordingly, we establish a hierarchy of preferred metallicity indicators based on the emission lines available for a given source.

The most-preferred metallicity estimate is derived by simultaneously fitting $[\text{O III}]\lambda 5007/\text{H}\beta$, $[\text{O III}]\lambda 5007/[\text{O II}]$, and (when available) $[\text{Ne III}]/[\text{O II}]$, following the approach of Sanders et al. (2021) and referred to here as O2O3Ne3. If $[\text{O II}]$ measurements are not available, $\text{O3N2} \equiv ([\text{O III}]\lambda 5007/\text{H}\beta)/([\text{N II}]\lambda 6584/\text{H}\alpha)$ is used to derive metallicities. If $[\text{O III}]$ and/or $\text{H}\beta$ are lacking, then $\text{N2} = [\text{N II}]\lambda 6584/\text{H}\alpha$ is used. O3N2 is preferred over N2 because metallicities estimated from O3N2 are less affected by N/O variations than those based on N2 alone. As described in Appendix A, the Bian et al. (2018) O3N2 and N2 calibrations have been renormalized such that they yield consistent metallicities on average with those derived from O2O3Ne3 for galaxies at $z \sim 2$.

In our sample, 10 galaxies have detections of $[\text{O II}]$, $[\text{O III}]$, and $\text{H}\beta$ (2 with $[\text{Ne III}]$ as well) for which O2O3Ne3 metallicities can be derived. All 13 targets have detections of $\text{H}\beta$, $[\text{O III}]$, $\text{H}\alpha$, and $[\text{N II}]$ such that O3N2 and N2 metallicities are available. In the following analysis, the oxygen abundance of each source is taken to be the best available estimate based on the preference of O2O3Ne3, then O3N2, then N2 unless otherwise specified. We obtain consistent results if we instead use O3N2 metallicities uniformly for the full sample, with the main quantitative difference being that the slopes of the anti-correlations presented in Section 3.4.3 are slightly different. We define the offset from the mass–metallicity relation at fixed M_* as a function of redshift as $\Delta \log(\text{O/H})_{\text{MZR}} \equiv 12 + \log(\text{O/H}) - \text{MZR}(M_*, z)$. Here, MZR (M_*, z) is the parameterization of the evolving mass–metallicity relation derived in Appendix B:

$$\text{MZR}(M_*, z) = 8.80 - 0.28 \times \log(1 + [M_*/M_0(z)]^{-1.08}) \quad (1)$$

$$\text{where } \log(M_0(z)/M_\odot) = 9.90 + 2.06 \times \log(1 + z).$$

2.6. Composite CO(3–2) Spectra

Given that CO(3–2) emission is not robustly detected for approximately half of our sample, we employ spectral stacking techniques to include information from all of the targets in our analysis. We create composite spectra by converting the extracted 1D spectra from flux density to luminosity density and shifting the frequency axis to velocity offset based on the systemic redshift measured from the rest-optical lines. We then combine the individual spectra by taking the unweighted mean luminosity density at intervals of 50 km s^{-1} velocity offset. We do not use any weighting because the on-source integration times and sensitivities varied widely from source to source, such that the few sources with long integration times dominate the stacks if inverse-variance weighting is used. The composite CO(3–2) spectrum is then converted back to flux density using the mean redshift of the included individual galaxies. The composite CO(3–2) line flux is measured by fitting a Gaussian profile to the composite 1D spectrum, and is presented in Table 1.

We create composite CO(3–2) spectra of all of the galaxies in our sample (13 sources, labeled “stack-all”) and the subset

that are not robustly detected (eight sources, labeled “stack-nondet”). We also stack in two bins of various galaxy properties divided such that there are roughly equal numbers of galaxies per bin. The galaxy properties according to which we bin include offset from the MS ($\Delta \log(\text{SFR})_{\text{MS}}$; “stack-delsfms”) and metallicity ($12 + \log(\text{O/H})$; “stack-oh”). Splitting the sample in Σ_{SFR} results in identical bins as stack-delsfms, while binning according to offset from the mass–metallicity relation ($\Delta \log(\text{O/H})_{\text{MZR}}$) yields the same results as stack-oh. The mass, SFR, effective radius, and metallicity associated with each composite CO(3–2) spectrum given in Table 1 are the mean $\log(M_*)$, $\log(\text{SFR})$, rest-optical R_{eff} , and $12 + \log(\text{O/H})$ of the individual galaxies included in each stack.

Example composite CO(3–2) 1D spectra are shown in the bottom row of Figure 2 for the stack-all and stack-nondet samples. The integrated CO(3–2) significance is $\geq 4.8\sigma$ for all stacked spectra used in this paper (stack-nondet has the lowest significance). The top row displays 2D stacks constructed by producing data cubes using TCLEAN with a uv taper of $3''$ and a spatial sampling of $0''.5$ pixel to homogenize the beam sizes, integrating the channels within $\pm 300 \text{ km s}^{-1}$ of the systemic redshift, and taking the mean flux value at each spatial position relative to the HST imaging centroid. While we utilize composite CO(3–2) fluxes from the stacked 1D spectra in the following analysis, line fluxes derived by spatially integrating the 2D composites agree with the 1D fluxes within 20%.

2.7. Literature CO Sample

We draw from the literature a supplementary sample of star-forming galaxies at $z = 2$ –3 with both CO and metallicity constraints available. We selected galaxies at $z = 2$ –3 with CO(3–2) measurements from the PHIBSS (Tacconi et al. 2013) and ASPECS (Boogaard et al. 2019) surveys. This literature CO sample was then cross-matched with rest-optical spectroscopic surveys to identify objects for which metallicity constraints could be derived. Objects with $[\text{N II}]/\text{H } \alpha > 0.5$ were excluded as probable AGN. One additional object at $z = 1.99$ with rest-optical spectroscopy from Shapley et al. (2020) was included with a CO(1–0) measurement from Riechers et al. (2020). This literature sample comprises 23 galaxies with CO measurements (19 CO detections and four upper limits), 16 (12 CO detections and four upper limits) of which have gas-phase metallicity constraints from rest-optical emission lines (one from O3O2Ne3, six from O3N2, and nine from N2). The properties of the literature sample are presented in Table C1. Stellar masses and SFRs are taken from the literature sources and converted to a Chabrier (2003) IMF when necessary. Line ratios are calculated using the rest-optical line fluxes from the given spectroscopic O/H references, which we then use to derive metallicities as described in Section 2.5. This sample of $z = 2$ –3 literature sources complements the MOSDEF-ALMA sample in our analysis.

3. Results

3.1. Sample Properties

The redshift, M_* , and SFR properties of the MOSDEF-ALMA and $z = 2$ –3 literature CO samples are shown in Figure 3. The two samples are well-matched in redshift (top panel), with mean redshifts of 2.25 and 2.30, respectively. The combined sample spans $z = 2.0$ –2.7, with a mean redshift of

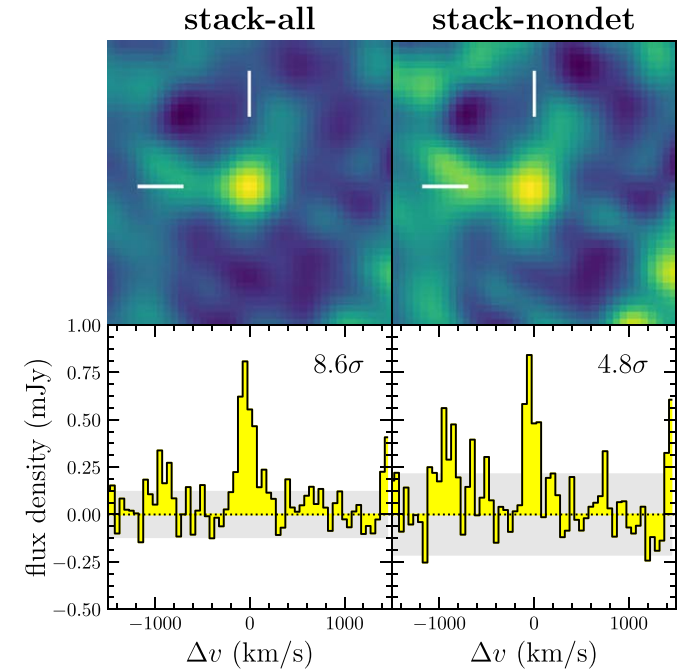


Figure 2. Example 2D (top) and 1D (bottom) composite CO(3–2) spectra for the stack-all (left; 13 galaxies) and stack-nondet (right; 8 galaxies) samples. The white crosshair is aligned with the expected spatial location of emission based on HST imaging centroids. The integrated CO(3–2) line S/N is given in the upper right corner of the bottom panels. The similarity of the noise patterns in the left and right columns arises because there are eight galaxies in common between the two stacks.

2.28 ± 0.17 , where the uncertainty represents the sample standard deviation.

The middle panel of Figure 3 shows SFR versus M_* . The MOSDEF-ALMA sample spans a range of stellar masses $\log(M_*/M_{\odot}) = 10.20$ – 10.57 with a mean mass of $10^{10.39} M_{\odot}$, and a range of SFRs $\log(\text{SFR}/M_{\odot} \text{ yr}^{-1}) = 1.32$ – 2.36 with a mean SFR of $85 M_{\odot} \text{ yr}^{-1}$. The MOSDEF-ALMA sample falls 0.25 dex above the MS on average (red square), while probing a large range of offsets below and above the MS. Our CO sample is complementary to existing ones at these redshifts, lying at lower stellar masses than samples from the large CO surveys PHIBSS and ASPECS (green points). The $z = 2$ –3 literature sample has a mean stellar mass of $10^{10.84} M_{\odot}$, a factor of 2.8 times larger than that of MOSDEF-ALMA, with a mean SFR that falls directly on the MS. In the combined sample, 29/36 sources fall within a factor of 3 of the Speagle et al. (2014) MS. Offsets from the MS are nearly identical if we instead adopt the MS parameterization of Whitaker et al. (2014), which matches that of Speagle et al. (2014) at < 0.1 dex in SFR at fixed M_* across the mass range of the combined sample.

The bottom panel of Figure 3 presents the mass–metallicity relation (MZR) at $z \sim 2.3$. On average, both the MOSDEF-ALMA and literature samples fall on the mean MZR at this redshift (black line, Equation (1)). The MOSDEF-ALMA sample in particular displays a wide range of metallicities spanning $12 + \log(\text{O/H}) = 8.36$ – 8.84 (0.5 – $1.4 Z_{\odot}$), with a mean metallicity of 8.64 ($0.9 Z_{\odot}$).

Collectively, the combined sample is representative in both SFR and metallicity of typical $z \sim 2.3$ star-forming galaxies in the mass range $\log(M_*/M_{\odot}) = 10.3$ – 11.0 , falling on the mean MS and MZR at this redshift. The addition of the MOSDEF-

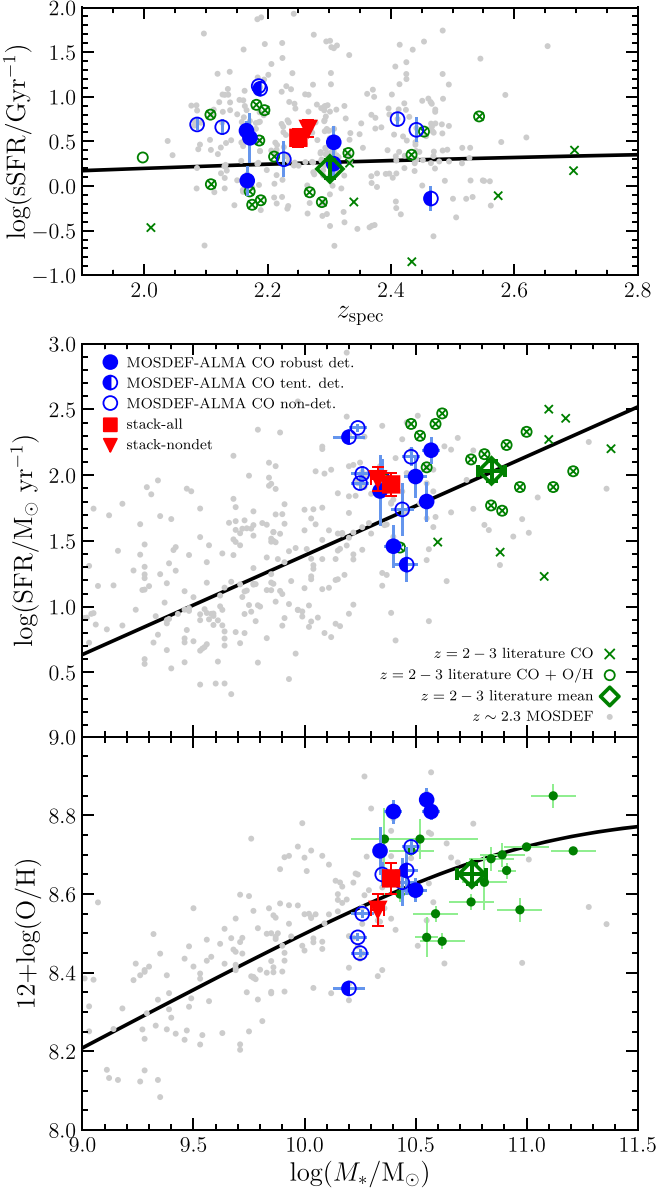


Figure 3. Properties of the $z \sim 2.3$ MOSDEF-ALMA sample (blue) and the $z = 2-3$ literature sample (green). Top: Specific SFR ($\text{sSFR} = \text{SFR}/M_*$) vs. redshift. Robust CO detections from MOSDEF-ALMA are displayed as filled blue circles, while tentative detections are half-filled and nondetections are unfilled. Red points show values for composite spectra. Green X symbols denote literature objects with CO measurements, where green circles indicate those with gas-phase metallicity constraints. The green diamond shows the mean values of the literature sample. The full sample of $z \sim 2.3$ star-forming galaxies from the MOSDEF survey are displayed as small gray points. The black solid line presents the star-forming main sequence of Speagle et al. (2014) evaluated at $10^{10.5} M_\odot$. Middle: SFR vs. M_* , with points as above. The black line shows the Speagle et al. (2014) parameterization evaluated at $z = 2.3$. Bottom: O/H vs. M_* . This panel only includes literature sources with metallicity constraints (green circles). The black line displays the parameterization of the mass–metallicity relation given in Equation (1) evaluated at $z = 2.3$.

ALMA observations expands the sample of $z \sim 2$ galaxies with CO measurements to lower masses and metallicities than were available to date. The wide range of offsets both above and below the mean MS and MZ relations makes MOSDEF-ALMA an ideal sample with which to search for correlated residuals around mass-scaling relations that are signposts of self-regulated baryon cycling.

3.2. $\text{CO}(3-2)$ Luminosity and Galaxy Properties

Before deriving molecular gas masses, we first explore empirical relations between observed $\text{CO}(3-2)$ luminosity and global galaxy properties with the goal of assessing whether the CO production efficiency, and thus the CO-to- H_2 conversion factor, varies systematically. Integrated $\text{CO}(3-2)$ line fluxes, S_{CO} , are converted to total line luminosities using the relation of Solomon et al. (1997):

$$L'_{\text{CO}} = 3.25 \times 10^7 S_{\text{CO}} \nu_{\text{obs}}^{-2} D_L^2 (1+z)^{-3}, \quad (2)$$

where ν_{obs} is the observed line frequency in GHz and D_L is the luminosity distance in Mpc. The MOSDEF-ALMA $\text{CO}(3-2)$ luminosities are given in Table 1.

The relation between $L'_{\text{CO}(3-2)}$ and stellar mass is shown in the top panel of Figure 4. The points are color-coded by offset from the star-forming main sequence, $\Delta \log(\text{SFR})_{\text{MS}}$. We find a significant positive correlation between $L'_{\text{CO}(3-2)}$ and M_* , with an evident secondary dependence on $\Delta \log(\text{SFR})_{\text{MS}}$ such that galaxies at fixed M_* with higher $L'_{\text{CO}(3-2)}$ have higher SFR.¹² Such a secondary dependence is expected if galaxies above (below) the MS have larger (smaller) molecular gas reservoirs than those on the MS, as has been observed in the local universe (e.g., Saintonge et al. 2016, 2017; Saintonge & Catinella 2022) and at high redshifts with dust- and CO-based measurements (e.g., Tacconi et al. 2013; Genzel et al. 2015; Scoville et al. 2017; Tacconi et al. 2018; Aravena et al. 2020; Tacconi et al. 2020). Using an orthogonal distance regression, we fit a function that is linear in $\log(M_*)$ and $\Delta \log(\text{SFR})_{\text{MS}}$ to the combined sample of individual galaxies (excluding limits), and find a best-fit relation of

$$\log \left(\frac{L'_{\text{CO}(3-2)}}{\text{K km s}^{-1} \text{pc}^2} \right) = 1.10(\pm 0.17) \times \log \left(\frac{M_*}{10^{10.7} M_\odot} \right) + 0.71(\pm 0.14) \times \log \left(\frac{\text{SFR}}{\text{SFR}_{\text{MS}}} \right) + 9.86(\pm 0.04). \quad (3)$$

Since this relation is a function of $\Delta \log(\text{SFR})_{\text{MS}}$, the fact that the MOSDEF-ALMA sample lies above the MS on average does not introduce bias. The stack of the MOSDEF-ALMA nondetections is 1σ consistent with this best-fit relation, suggesting that the exclusion of limits when fitting has not significantly biased this result. After accounting for measurement uncertainties, the remaining intrinsic scatter in $L'_{\text{CO}(3-2)}$ around the best-fit function is $\sigma_{\text{int}} = 0.17$ dex. This equation can thus be used to predict the $\text{CO}(3-2)$ luminosity of $z \sim 2$ galaxies to within a factor of ≈ 1.5 using M_* and SFR alone. If the SFR term is neglected such that $L'_{\text{CO}(3-2)}$ is a function of M_* alone (gray line, top panel of Figure 4), the intrinsic scatter is 0.31 dex.

The ratio of $L'_{\text{CO}(3-2)}$ to SFR is a proxy of the CO production per unit M_{mol} because SFR is tightly coupled to M_{mol} via the molecular KS law (e.g., Kennicutt 1998; Tacconi et al. 2013; de los Reyes & Kennicutt 2019; Kennicutt & De Los Reyes 2021). The bottom panel of Figure 4 displays $L'_{\text{CO}(3-2)}/\text{SFR}$ as a function of M_* . A positive correlation remains after normalizing $L'_{\text{CO}(3-2)}$ by SFR, made clear by the sample means, though with

¹² At fixed M_* , $\text{SFR} = \Delta \log(\text{SFR})_{\text{MS}} + C$, where C is a constant equal to the SFR of the mean star-forming main sequence at that mass. As such, trends in $\Delta \log(\text{SFR})_{\text{MS}}$ represent trends in absolute SFR when working at fixed M_* .

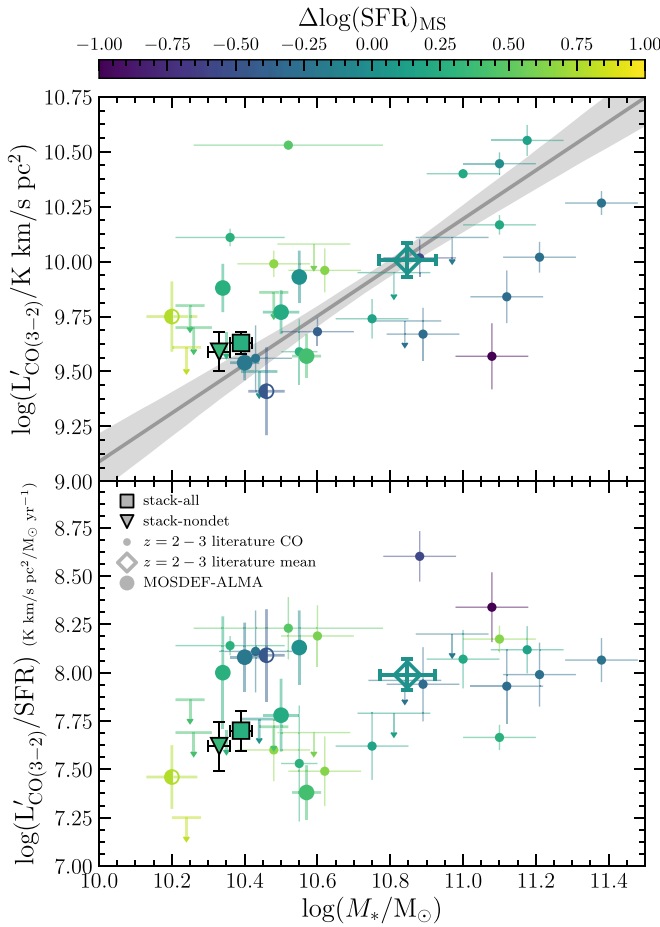


Figure 4. CO(3–2) luminosity ($L'_{\text{CO}(3-2)}$, top) and $L'_{\text{CO}(3-2)}/\text{SFR}$ (bottom) vs. stellar mass for the $z \sim 2$ CO sample, color-coded by offset from the star-forming main sequence. Arrows provide 3σ limits for CO-undetected sources. Gray lines indicate best-fit linear relations from a bivariate weighted orthogonal distance regression. The light gray shaded region displays the 1σ uncertainty bounds on the best-fit line. In the top panel, the gray line corresponds to Equation (3) evaluated at $\Delta\log(\text{SFR})_{\text{MS}} = 0$.

very large scatter at fixed M_* . No secondary trend with $\Delta\log(\text{SFR})_{\text{MS}}$ is evident. The correlation in the bottom panel of Figure 4 implies that CO(3–2) emission is more efficiently produced per unit of molecular gas mass in high-mass galaxies.

Figure 5 presents $L'_{\text{CO}(3-2)}/\text{SFR}$ as a function of metallicity. There is a positive correlation between these two quantities, with significantly smaller scatter in $L'_{\text{CO}(3-2)}/\text{SFR}$ at fixed O/H compared to that at fixed M_* , suggesting that the relation between $L'_{\text{CO}(3-2)}/\text{SFR}$ and O/H is more fundamental such that the correlation with M_* emerges because of the mass–metallicity relation. Applying a Spearman correlation test to the individually detected sources yields $\rho_S = 0.45$ and a p –value = 0.05, indicating a 2σ correlation. If the one significant outlier is excluded (discussed below), the correlation is stronger with $\rho_S = 0.65$ and p –value = 0.003, indicating 3σ significance. Fitting a linear function to the individual galaxies, excluding limits, yields

$$\log\left(\frac{L'_{\text{CO}(3-2)}}{\text{SFR}}\right) = 1.29(\pm 0.44) \times x + 7.91(\pm 0.07), \quad (4)$$

where $x = 12 + \log(\text{O/H}) - 8.7$, $L'_{\text{CO}(3-2)}$ is in units of $\text{K km s}^{-1} \text{pc}^2$, and SFR is in units of $M_\odot \text{ yr}^{-1}$. There is no significant secondary dependence on $\Delta\log(\text{SFR})_{\text{MS}}$, suggesting

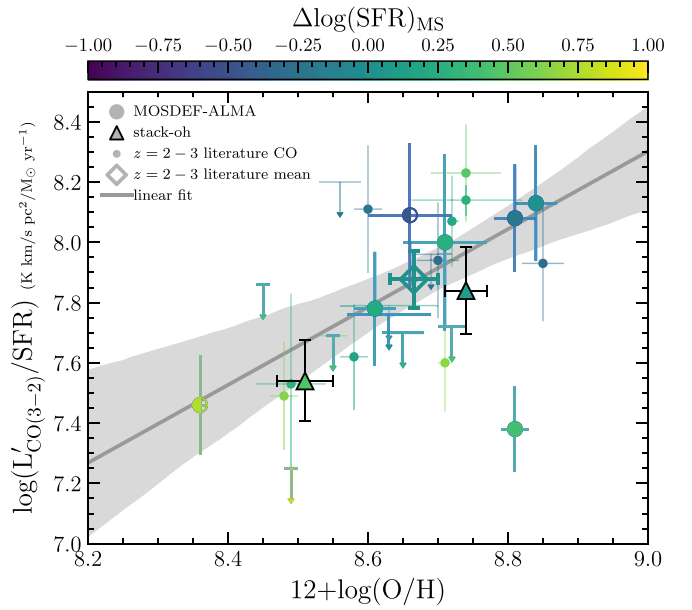


Figure 5. $L'_{\text{CO}(3-2)}/\text{SFR}$ vs. gas-phase oxygen abundance, with points and lines as in Figure 4. Colored triangles denote measurements from composite spectra in two bins of O/H. The best-fit linear relation is given in Equation (4).

that the best-fit relation is robust even though the MOSDEF-ALMA sample is offset above the MS on average. The composite spectra agree with the best-fit relation at the 1σ level, implying that our exclusion of limits when fitting has not significantly biased the result. The intrinsic scatter about this best-fit line is 0.12 dex after accounting for measurement uncertainties.

The single significant outlier in Figure 5, lying $\sim 4\sigma$ below the best-fit line, is ID 13701 in the MOSDEF-ALMA sample, a potential merger with tidal tail-like features and two distinct brightness peaks in HST imaging (Figure 1). It is possible that the low $L'_{\text{CO}(3-2)}/\text{SFR}$ of ID 13701 is a result of an enhanced star formation efficiency ($\text{SFR}/M_{\text{mol}}$) during a major merger (Di Matteo et al. 2007; Sargent et al. 2014; Kennicutt & De Los Reyes 2021) because $L'_{\text{CO}(3-2)}$ traces M_{mol} , though it is unclear how significant such enhancement is expected to be in high-redshift mergers (Fensch et al. 2017).

The positive correlation between $L'_{\text{CO}(3-2)}/\text{SFR}$ and O/H demonstrates that the production efficiency of CO(3–2) is a function of metallicity, with low-metallicity galaxies outputting less CO(3–2) per unit SFR than metal-rich galaxies. If the star formation efficiency (or equivalently, depletion timescale) is similar across our sample, then the correlation in Figure 5 implies a decreasing CO luminosity per unit M_{mol} with decreasing metallicity in $z \sim 2$ star-forming galaxies. This same trend has been observed in local galaxy samples, manifesting as a metallicity-dependent CO-to-H₂ conversion factor (α_{CO}) with α_{CO} increasing with decreasing metallicity (Wilson 1995; Arimoto et al. 1996; Wolfire et al. 2010; Schruba et al. 2012; Bolatto et al. 2013; Accurso et al. 2017). Higher α_{CO} at lower O/H, corresponding to lower CO luminosity per unit gas mass, arises because CO is dissociated at greater depths into H₂ clouds in low-metallicity environments. CO molecules are photodissociated by far-UV photons and require dust shielding to prevent dissociation (e.g., Wolfire et al. 2010; Glover & Mac Low 2011). Metal-poor galaxies have lower dust-to-gas ratios (e.g., Sandstrom et al. 2013; De Vis et al. 2019), and

low-metallicity massive stars produce harder and more intense UV radiation fields, such that there is an increasing fraction of CO-dark H₂ gas with decreasing metallicity. The trend in Figure 5 thus suggests that a metallicity-dependent α_{CO} is required to accurately translate observed CO luminosities of $z \sim 2$ galaxies into molecular gas masses.

3.3. The CO-to-H₂ Conversion Factor at $z \sim 2$

Given the evidence for a metallicity-dependent α_{CO} at $z \sim 2$ presented above, we utilize a combined sample of MOSDEF-ALMA and literature targets at $z > 1$ with CO and rest-optical spectra to constrain the form of the $\alpha_{\text{CO}}-\text{O/H}$ relation at high redshifts. Genzel et al. (2012) presented evidence for a $\alpha_{\text{CO}}-\text{O/H}$ relation at high redshift using a sample of ~ 40 $z > 1$ main-sequence galaxies, but the majority of their sample lacked spectroscopic metallicity constraints and instead had metallicities inferred from the MZR, with only a subset of nine CO-detected galaxies having metallicities based on [N II]/H α ratios. The analysis below represents a significant improvement on the foundational results of Genzel et al. (2012) by using a sample composed entirely of galaxies with spectroscopic metallicities.

To maximize the sample size for the α_{CO} analysis, we supplement the combined $z = 2-3$ MOSDEF-ALMA and literature CO+O/H sample with 14 additional galaxies at $z > 1$ with the necessary observations that were not included in our primary sample because they either fall outside of the target redshift range (i.e., at $z = 1-2$ or $z > 3$), are extreme starbursts with $\Delta \log(\text{SFR})_{\text{MS}} \geq 10$, or are strongly gravitationally lensed. Sources in this supplementary $z > 1$ sample are given in Table C1. Thus, this expanded sample is only used for the α_{CO} analysis, while the remainder of the paper employs only the more homogeneous $z = 2-3$ MOSDEF-ALMA and literature samples described in Section 2.7. The α_{CO} sample includes 43 galaxies spanning $z = 1.08-3.22$ with a mean redshift of 2.12. Of these 43 sources, all have metallicity constraints from rest-optical line ratios, 33 have CO detections, and 10 have CO upper limits.

The CO-to-H₂ conversion factor α_{CO} is defined as

$$\alpha_{\text{CO}} = \frac{M_{\text{mol}}}{L'_{\text{CO}(1-0)}} = \frac{r_{J1} M_{\text{mol}}}{L'_{\text{CO}(J-J-1)}}, \quad (5)$$

where M_{mol} is the total molecular gas mass including a 36% contribution from helium, and r_{J1} is the excitation correction factor to convert higher- J CO luminosities to that of the ground transition. We adopt $r_{31} = 0.55$ (Tacconi et al. 2018) and $r_{21} = 0.76$ (Daddi et al. 2015). Our α_{CO} sample contains 33 galaxies with CO(3–2) measurements, seven with CO(2–1) and three with CO(1–0). Our results are thus most sensitive to the assumed r_{31} value, whereas the adopted r_{21} will have only a minor effect.

Constraining α_{CO} requires an estimate of M_{mol} that is independent of CO emission. We employ two methods of estimating M_{mol} : from dynamical masses, and via the molecular KS law. Both techniques require the galaxy size in the calculations, so we required a half-light radius measurement in our selection criteria. We operate under the assumption that the effective radii of rest-optical continuum emission, H α emission, and molecular gas are similar for $z \sim 2$ galaxies, as has been found at $z \sim 1-2$ by comparing resolved H α and CO sizes to HST imaging (Tacconi et al. 2013;

Förster Schreiber et al. 2019). We describe the calculations of M_{mol} using each method below.

3.3.1. Dynamical Mass Method

The dynamical mass M_{dyn} provides a measure of the total mass in a galaxy, including stars, gas, and dark matter. We assume that $z \sim 2$ galaxies are dominated by baryons within the effective radius such that dark matter is negligible (Genzel et al. 2017, 2020; Price et al. 2021), and that the total gas mass in $z > 1$ galaxy disks is dominated by the molecular component (Tacconi et al. 2018). Under these assumptions, M_{mol} can be inferred from M_{dyn} using

$$M_{\text{mol}} \approx M_{\text{dyn}} - M_{*}. \quad (6)$$

In the α_{CO} sample, 13 objects have M_{dyn} constraints based on measured rotation, either from H α velocity mapping (seven galaxies; Förster Schreiber et al. 2006, 2018), CO velocity mapping (one galaxy; Swinbank et al. 2011), or forward-modeling of tilted emission lines in slit spectra (five galaxies; Price et al. 2016, 2020).

For targets without measured rotation, M_{dyn} can be estimated via the virial mass equation

$$M_{\text{dyn}} = \frac{k R_{\text{eff}} \sigma_v^2}{G}, \quad (7)$$

where G is the gravitational constant, σ_v is the velocity dispersion measured from emission line widths (corrected for instrumental resolution), k is the virial coefficient, and R_{eff} is the half-light elliptical semimajor axis. The value of the virial coefficient depends on the mass and velocity distribution of stars and gas in the source. Rather than assuming a value for k from the literature, we calibrate k such that dispersion-based M_{dyn} estimated using Equation (7) matches rotation-based M_{dyn} on average for the 13 targets with measured rotation. This process yields a best-fit value of $k = 8.6$, very close to the virial coefficient for an exponential profile (Sérsic index $n = 1$) from Cappellari et al. (2006). Our best-fit virial coefficient is somewhat higher than has been used for disks and spheroids in past work ($k \approx 3-6$; e.g., Pettini et al. 2001; Erb et al. 2006b; Cappellari et al. 2006; Price et al. 2016), though this difference is at least partially explained by the fact that we do not perform inclination corrections such that our best-fit k encompasses both the virial coefficient and an average inclination correction factor. Excluding the 13 objects with measured rotation, we find that 26 of the remaining galaxies have published line widths, for which we calculate M_{dyn} using Equation (7). We thus have M_{dyn} constraints for a sample of 39 galaxies (13 from rotation, 26 from line widths), for which we estimate M_{mol} with Equation (6) and $\alpha_{\text{CO}}^{\text{dyn}}$ using Equation (5). Seven objects have $M_{*} > M_{\text{dyn}}$ such that the inferred M_{mol} and $\alpha_{\text{CO}}^{\text{dyn}}$ are unphysically negative, which we attribute to the large systematic scatter in deriving M_{dyn} from spatially unresolved measurements. For these sources, we instead calculate 3σ upper limits on M_{mol} and $\alpha_{\text{CO}}^{\text{dyn}}$.

The molecular gas mass can also be estimated by applying the molecular KS relation between the surface densities of SFR (Σ_{SFR}) and molecular gas mass (Σ_{mol}) (e.g., Kennicutt 1998; Tacconi et al. 2013; de los Reyes & Kennicutt 2019; Kennicutt

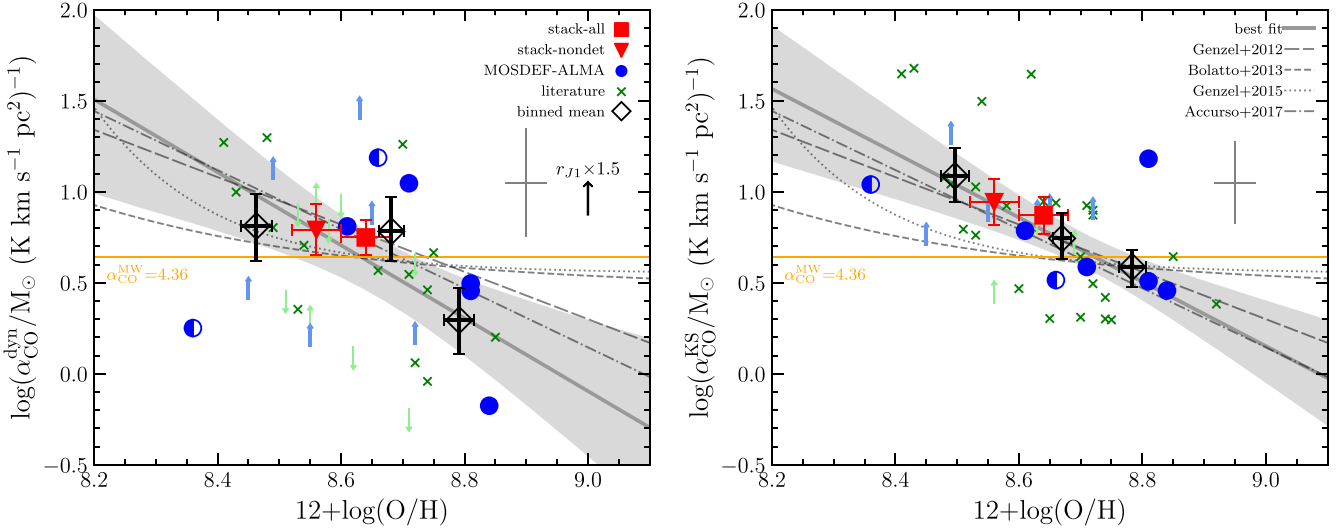


Figure 6. The CO-to-H₂ conversion factor, α_{CO} , vs. gas-phase oxygen abundance. In the calculation of α_{CO} , M_{mol} has been inferred from the difference between dynamical and stellar masses (left), or the molecular KS relation of Tacconi et al. (2013; right). Black open diamonds present mean α_{CO} values in three bins of O/H, with an equal number of sources in each bin. The gray error bars on the right side of each plot display the mean statistical uncertainty of the individual galaxies. The black arrow in the left panel demonstrates how the inferred α_{CO} values would change if the excitation correction factor r_{J1} was larger by 50%. Thin gray lines display α_{CO} –O/H relations from Genzel et al. (2012, long dashed), Bolatto et al. (2013, short dashed), Genzel et al. (2014, dotted), and Accurso et al. (2017, dashed-dotted). The orange line indicates the Milky Way α_{CO} value. The gray solid line shows the best-fit relation (Equations (11) and (12)), with the 1σ uncertainty bound shown in gray shading.

& De Los Reyes 2021). We calculated Σ_{SFR} according to

$$\Sigma_{\text{SFR}} = \frac{\text{SFR}}{2\pi r_{\text{eff}}^2}, \quad (8)$$

converted Σ_{SFR} to Σ_{mol} based on the adopted KS law

$$\Sigma_{\text{SFR}} = c \Sigma_{\text{mol}}^n \quad (9)$$

with Σ_{SFR} in units of $M_{\odot} \text{ yr}^{-1} \text{ kpc}^{-2}$ and Σ_{mol} in units of $M_{\odot} \text{ pc}^{-2}$, and finally derived M_{mol} using

$$M_{\text{mol}} = 2\pi r_{\text{eff}}^2 \Sigma_{\text{mol}}, \quad (10)$$

where the same value of r_{eff} is used in the first and last steps. We adopt the molecular KS law of Tacconi et al. (2013) adjusted for the different r_{31} assumed in that work, with $\log(c) = -2.96$ and $n = 1.05$. This M_{mol} estimate is then applied in Equation (5) to infer $\alpha_{\text{CO}}^{\text{KS}}$.

3.3.2. The α_{CO} –O/H Relation at $z \sim 2$

Figure 6 shows α_{CO} as a function of metallicity using the dynamical mass method (left panel) and the KS law method (right panel). The black diamonds show mean values of the individual objects (excluding limits) in three bins of O/H. With both methods, we find a trend of decreasing α_{CO} with increasing O/H. In each panel, only one source at $12+\log(\text{O/H}) > 8.7$ has inferred $\alpha_{\text{CO}} > 10$, while several galaxies exceed this value at lower metallicities. Likewise, α_{CO} lower than the Milky Way value of 4.36 is common at $12+\log(\text{O/H}) > 8.6$, while at lower metallicities there are only two galaxies that have $\alpha_{\text{CO}}^{\text{dyn}} < 4.36$ and none with $\alpha_{\text{CO}}^{\text{KS}}$ below the Galactic value. A Spearman correlation test indicates $\rho_S = -0.55$ and $p - \text{value} = 0.0098$ for $\alpha_{\text{CO}}^{\text{dyn}}$, and $\rho_S = -0.62$ and $p - \text{value} = 1.1 \times 10^{-4}$ for $\alpha_{\text{CO}}^{\text{KS}}$, rejecting the null hypothesis of no correlation at 2.6σ and 3.3σ , respectively.

We fit power-law relations to the individual galaxies, excluding sources with α_{CO} limits. The best-fit relations (thick

gray lines in Figure 6) are

$$\log(\alpha_{\text{CO}}^{\text{dyn}}) = -2.00(\pm 0.97) \times x + 0.51(\pm 0.16) \quad (11)$$

$$\log(\alpha_{\text{CO}}^{\text{KS}}) = -1.76(\pm 0.70) \times x + 0.68(\pm 0.09), \quad (12)$$

where $x = 12 + \log(\text{O/H}) - 8.7$ and α_{CO} is in units of $M_{\odot} (\text{K km s}^{-1} \text{ pc}^2)^{-1}$. The MOSDEF-ALMA stacks are consistent with the best-fit relations, suggesting that the exclusion of limits has not introduced a significant bias. These best-fit relations are fully consistent with one another despite the different methods employed to estimate α_{CO} . They are also generally consistent with existing α_{CO} –O/H calibrations (Genzel et al. 2012; Bolatto et al. 2013; Genzel et al. 2015; Accurso et al. 2017), though the $z \sim 2$ data favor a steeper slope than that of Bolatto et al. (2013) and are in particularly good agreement with the Accurso et al. (2017) relation, which has a slope of -1.623 and a normalization at $12+\log(\text{O/H}) = 8.7$ of 0.63 ± 0.165 . Our fits also broadly agree with $\alpha_{\text{CO}}(\text{O/H})$ at $z = 2$ derived from the SIMBA cosmological simulations (Davé et al. 2020).

A number of systematic uncertainties may affect the position of the $z \sim 2$ sample in the α_{CO} –O/H plane. First, the metallicity calibration can shift galaxies horizontally. We have employed the high-redshift analog calibrations of Bian et al. (2018, see Appendix A, Table A1). If we instead use the $z \sim 0$ calibrations of Pettini & Pagel (2004) or Curti et al. (2017, 2020), the metallicities decrease by ≈ 0.15 dex on average. Given that the majority of the sample has CO(3–2) measurements, the value of the r_{31} excitation correction factor, which is not well-constrained at high redshift, can shift galaxies vertically. If we instead assume r_{31} that is 1.5 times larger (i.e., $r_{31} = 0.84$ as found by Riechers et al. 2020 for five $\sim 10^{11} M_{\odot}$ galaxies at $z \approx 2.6$), the inferred α_{CO} would decrease by 0.18 dex. Finally, the assumed molecular KS law and virial coefficient affect $\alpha_{\text{CO}}^{\text{KS}}$ and $\alpha_{\text{CO}}^{\text{dyn}}$, respectively.

While these systematic uncertainties are a significant concern for the absolute normalization of the $\alpha_{\text{CO}} - \text{O/H}$ relation, they each shift the majority of galaxies in our sample in the same direction unless there is a strong systematic dependence of r_{31} or the virial coefficient on metallicity. It is plausible that r_{31} increases with decreasing metallicity, because the combination of reduced dust shielding and harder and more intense UV radiation fields at low metallicity is expected to more highly excite CO. In this scenario, the true $\alpha_{\text{CO}}(\text{O/H})$ slope would be steeper than our derivation that assumes a constant r_{31} , though more high-redshift galaxies with detections of both CO(3–2) and CO(1–0) are needed to robustly assess the impact of excitation (Boogaard et al. 2020; Riechers et al. 2020). With the currently available constraints, we conclude that α_{CO} depends on O/H at $z \sim 2$ with similar dependence to that observed at $z \sim 0$. It is crucial to take this metallicity dependence into account to derive accurate gas masses for subsolar-metallicity galaxies that are common in the high-redshift universe.

3.4. The Molecular Gas Content of $z \sim 2$ Star-forming Galaxies

In this section, we derive molecular gas masses for the MOSDEF-ALMA and $z = 2$ –3 literature samples, and explore relationships between molecular gas content, stellar mass, SFR, and metallicity. Based on the good agreement with the $z \sim 2$ galaxies in Figure 6, we adopt the Accurso et al. (2017) relation between α_{CO} and metallicity¹³ with a floor at the Milky Way value of $\alpha_{\text{CO}}^{\text{MW}} = 4.36 M_{\odot} (\text{K km s}^{-1} \text{ pc}^2)^{-1}$ such that supersolar metallicity galaxies do not have significantly smaller values of α_{CO} :

$$\log(\alpha_{\text{CO}}) = \begin{cases} 14.752 - 1.623x, & \text{if } x \leq 8.7 \\ \log(4.36), & \text{if } x > 8.7 \end{cases} \quad (13)$$

where $x = 12 + \log(\text{O/H})$. Molecular gas masses are calculated assuming this $\alpha_{\text{CO}}(\text{O/H})$ relation and $r_{31} = 0.55$, where the latter is adopted for consistency with Tacconi et al. (2018). For the seven literature sources without spectroscopic metallicity constraints, O/H from the MZR(M_* , z) of Equation (1) is used for M_{mol} calculations, and these sources are excluded from any plots and analyses that directly include metallicity. The derived molecular gas properties of the MOSDEF-ALMA sample and stacks are presented in Table 1, while those of the $z = 2$ –3 literature sample are given in Table C1.

3.4.1. Molecular Gas Content and Stellar Mass

The molecular gas masses, M_{mol} , and molecular gas fractions, $\mu_{\text{mol}} = M_{\text{mol}}/M_*$, are shown as a function of M_* in the top and middle panels of Figure 7, with points color-coded by offset from the star-forming main sequence. On average, the MOSDEF-ALMA sample has lower M_{mol} and higher μ_{mol} than the more-massive literature sample, indicating a positive correlation between M_{mol} and M_* and an anticorrelation between μ_{mol} and M_* . M_{mol} is typically larger than M_* below $10^{10.8} M_{\odot}$, with an average $\mu_{\text{mol}} \approx 2$ at $10^{10.4} M_{\odot}$.

¹³ The Accurso et al. (2017) α_{CO} parameterization is a function of offset in SFR from the MS in addition to metallicity. However, the SFR dependence is very weak, such that even a large offset of 1 dex from the MS changes α_{CO} by only 0.06 dex(15%). We ignore the SFR term and evaluate the Accurso et al. (2017) relation on the MS such that α_{CO} is only a function of O/H.

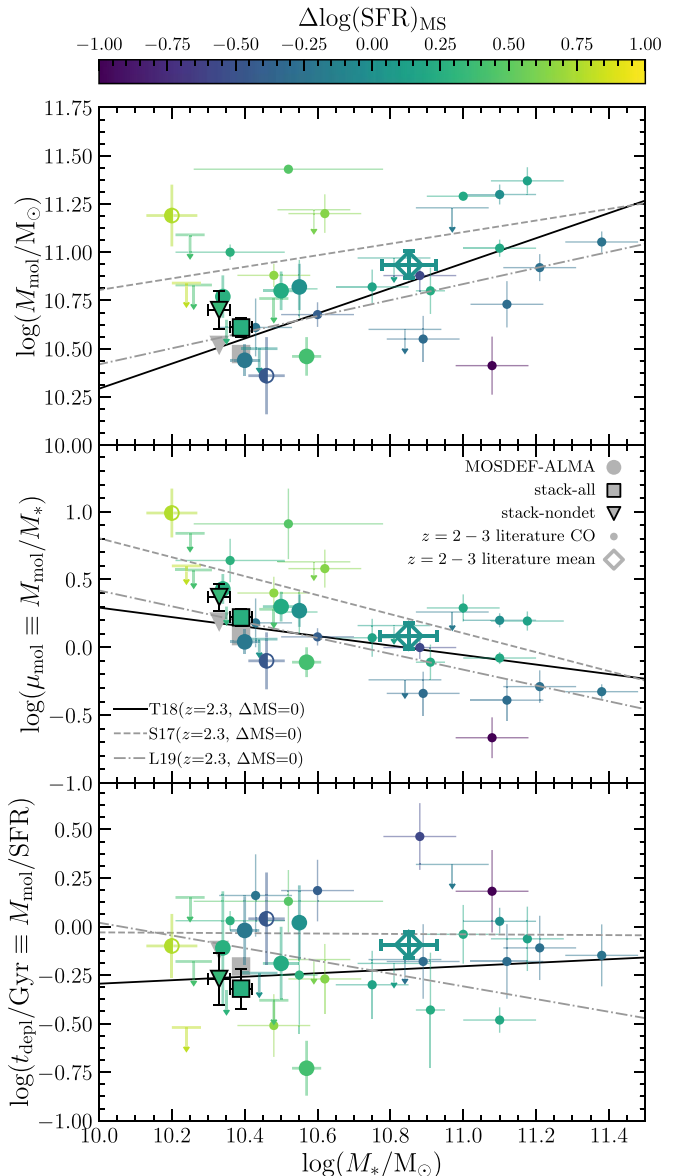


Figure 7. Molecular gas mass (top), gas fraction (middle), and depletion time (bottom) as a function of stellar mass. Points are color-coded according to offset from the star-forming main sequence of Speagle et al. (2014). Arrows denote 3σ upper limits for sources with CO nondetections. The black solid line in each panel shows the scaling relations of Tacconi et al. (2018) evaluated at $z = 2.3$ and on the main sequence. Gray points show the position of the composite spectra (stack-all and stack-nondet) after correcting for their offset from the MS according to the $\Delta \text{SFR}_{\text{MS}}$ dependence of the Tacconi et al. (2018) relations. The gray dashed and dotted-dashed lines display the scaling relations of Scoville et al. (2017) and Liu et al. (2019), respectively, evaluated at $z = 2.3$ for targets on the main sequence.

Consequently, gas mass is expected to dominate the baryonic mass of $z \sim 2$ galaxies at $\lesssim 10^{10.4} M_{\odot}$.

There is a significant additional dependence on SFR such that galaxies with higher SFR at fixed M_* have larger M_{mol} , as has been observed in previous works (e.g., Tacconi et al. 2013; Scoville et al. 2017; Tacconi et al. 2018; Liu et al. 2019; Tacconi et al. 2020). The black line shows the Tacconi et al. (2018) scaling relation¹⁴ evaluated at $z = 2.3$ and $\Delta \log(\text{SFR})_{\text{MS}} = 0$. While the sample average of the literature

¹⁴ While the scaling relation reported in Tacconi et al. (2018) is for μ_{mol} , this function can be converted to M_{mol} by multiplying by M_* .

sources falls on this relation, the MOSDEF-ALMA stacks fall slightly above it because the sample lies 0.25 dex above the MS on average. If we correct M_{mol} of the MOSDEF-ALMA stacks assuming the SFR dependence from Tacconi et al. (2018) ($M_{\text{mol}} \propto \Delta \text{SFR}_{\text{MS}}^{0.53}$; see also Figure 9, left), then the composites fall on the Tacconi et al. (2018) main-sequence relation. We thus find that the Tacconi et al. (2018) scaling relation reliably reproduces the average M_{mol} and μ_{mol} of $z \sim 2$ star-forming galaxies down to at least $\sim 10^{10.2} M_{\odot}$.

The bottom panel of Figure 7 presents the molecular gas depletion timescale, $t_{\text{depl}} = M_{\text{mol}}/\text{SFR}$. We do not find evidence for any significant dependence of t_{depl} on M_{*} across $\log(M_{*}/M_{\odot}) = 10.2\text{--}11.2$. In the sample averages, we find slightly lower t_{depl} at lower M_{*} , though the MOSDEF-ALMA and literature mean values are consistent with one another at the $\approx 1.5\sigma$ level. A dependence on offset from the MS is apparent, with higher-SFR galaxies at fixed M_{*} having shorter t_{depl} . The gray points once again show the MOSDEF-ALMA stacks corrected for their offset from the MS according to the dependence of the Tacconi et al. (2018) scaling relation ($t_{\text{depl}} \propto \Delta \text{SFR}_{\text{MS}}^{-0.44}$). The SFR-corrected stack of all MOSDEF-ALMA targets has $\log(t_{\text{depl}}/\text{Gyr}) = -0.20 \pm 0.10$ at $10^{10.4} M_{\odot}$, while the $z = 2\text{--}3$ literature mean is $\log(t_{\text{depl}}/\text{Gyr}) = -0.09 \pm 0.07$ at $10^{10.85} M_{\odot}$. We thus find that the molecular gas depletion timescale of $z \sim 2$ main-sequence star-forming galaxies at $\log(M_{*}/M_{\odot}) \sim 10\text{--}11.5$ is $t_{\text{depl}} = 600\text{--}800$ Myr with no significant M_{*} dependence, shorter by a factor of ~ 2 than that of main-sequence $z \sim 0$ galaxies at similar M_{*} with $t_{\text{depl}} \approx 1.4$ Gyr (Saintonge et al. 2016, 2017).

3.4.2. The $z \sim 2$ Molecular KS Law

Figure 8 shows Σ_{SFR} versus Σ_{mol} for $z = 2\text{--}3$ galaxies.¹⁵ We find a tight correlation between these quantities that is fit well by a linear relation with constant $t_{\text{depl}} = 700$ Myr (orange dashed line), in agreement with the findings of Tacconi et al. (2013) based on the PHIBSS $z = 1.0\text{--}1.5$ and $z = 2.0\text{--}2.5$ samples, the latter of which is included in our literature sample. The best-fit relation from fitting the individual galaxies (excluding limits) is

$$\log\left(\frac{\Sigma_{\text{SFR}}}{M_{\odot} \text{yr}^{-1} \text{kpc}^{-2}}\right) = 1.09(\pm 0.09) \left[\log\left(\frac{\Sigma_{\text{mol}}}{M_{\odot} \text{pc}^{-2}}\right) - 3 \right] + 0.10(\pm 0.05). \quad (14)$$

Our best-fit relation is fully consistent with the $z = 1\text{--}2.5$ relation from PHIBSS (Tacconi et al. 2013). The best-fit slope at $z = 2\text{--}3$ is consistent with the molecular KS law in the local universe that is generally found to be near-linear with either integrated or spatially resolved observations (e.g., Kennicutt 1998; Bigiel et al. 2008; Leroy et al. 2008; de los Reyes & Kennicutt 2019; Kennicutt & De Los Reyes 2021), although the normalization is offset from what is appropriate for typical integrated $z \sim 0$ main-sequence galaxies with $t_{\text{depl}} \approx 1\text{--}1.5$ Gyr (gray dotted line).

¹⁵ Our adopted $\alpha_{\text{CO}}(\text{O/H})$ relation from Accurso et al. (2017) was not derived using the KS relation. These authors employed radiative transfer modeling of [C II] and CO(1–0) to infer α_{CO} . As such, this $\alpha_{\text{CO}}(\text{O/H})$ relation does not imprint a certain KS relation by construction.

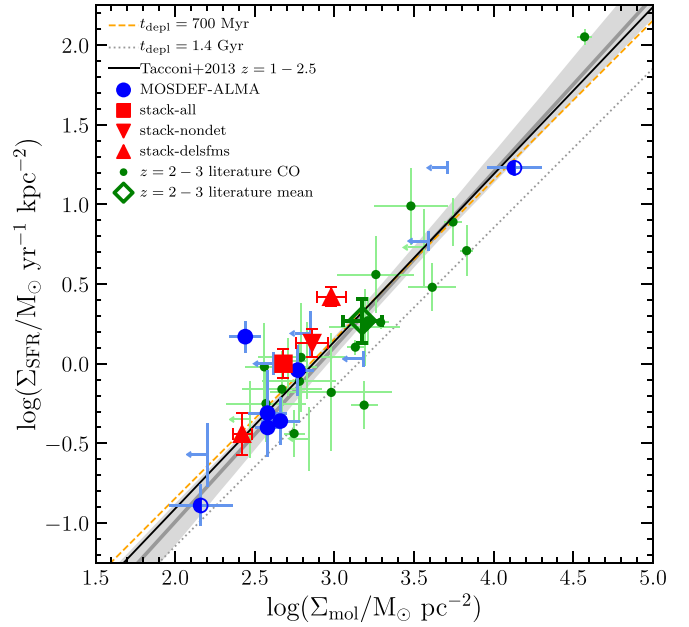


Figure 8. The molecular Kennicutt–Schmidt law relating Σ_{SFR} and Σ_{mol} . Upward red triangles denote composite spectra in two bins of Σ_{SFR} . The best linear fit (gray line) is very similar to the $z > 1$ KS law from Tacconi et al. (2013) and to a line of constant depletion time $t_{\text{depl}} = 700$ Myr (orange dashed line), but is offset from the Tacconi et al. (2013) fit to $z = 0$ data (dotted line).

We find that the $z \sim 2$ molecular KS law is very tight over nearly three orders of magnitude in Σ_{mol} and Σ_{SFR} , with an intrinsic scatter of 0.07 dex (18%) in Σ_{SFR} around the best-fit line after accounting for measurement uncertainties. The MOSDEF-ALMA results demonstrate that $z \sim 2$ galaxies down to $10^{10.2} M_{\odot}$ fall on a well-defined KS relation, implying that Equation (14) can be used to accurately infer M_{mol} (and M_{dyn} , assuming negligible dark matter) for existing large samples of $z \sim 2$ galaxies with SFR and size measurements in deep extragalactic legacy fields. This implication is especially beneficial for existing large rest-optical spectroscopic surveys, which have mean sample stellar masses of $\approx 10^{10} M_{\odot}$, e.g., MOSDEF (Kriek et al. 2015) and KBSS-MOSFIRE (Steidel et al. 2014).

3.4.3. Correlated Residuals around Mean Scaling Relations

We now search for correlations among the residuals around three mean scaling relations: the SFR– M_{*} relation (i.e., star-forming main sequence; MS), the mass–metallicity relation (MZR), and the $M_{\text{mol}}\text{--}M_{*}$ relation. Models of galaxy growth governed by a self-regulating baryon cycle predict that the scatter around these scaling relations will be (anti-)correlated (e.g., Lilly et al. 2013; Davé et al. 2017; De Rossi et al. 2017; Torrey et al. 2019). We adopt parameterizations of each of these mean relations as a function of M_{*} and redshift: SFR– M_{*} from Speagle et al. (2014), MZR from Equation (1), and $M_{\text{mol}}\text{--}M_{*}$ using the relation of Tacconi et al. (2018) evaluated on the MS ($\Delta \text{SFR}_{\text{MS}} = 0$). The residuals around each of these relations are derived by subtracting the logarithmic scaling relation value (at matched M_{*} and z) from the measured value for each object. We adopt the following terms for these residuals: $\Delta \log(\text{SFR})_{\text{MS}}$, $\Delta \log(\text{O/H})_{\text{MZR}}$, and $\Delta \log(M_{\text{mol}})_{\text{T18,MS}}$. Comparing these residual quantities to one another is a sensitive technique to search for secondary parameter dependences about M_{*} -scaling relations. Since the primary dependence on M_{*} has been subtracted off, this approach allows

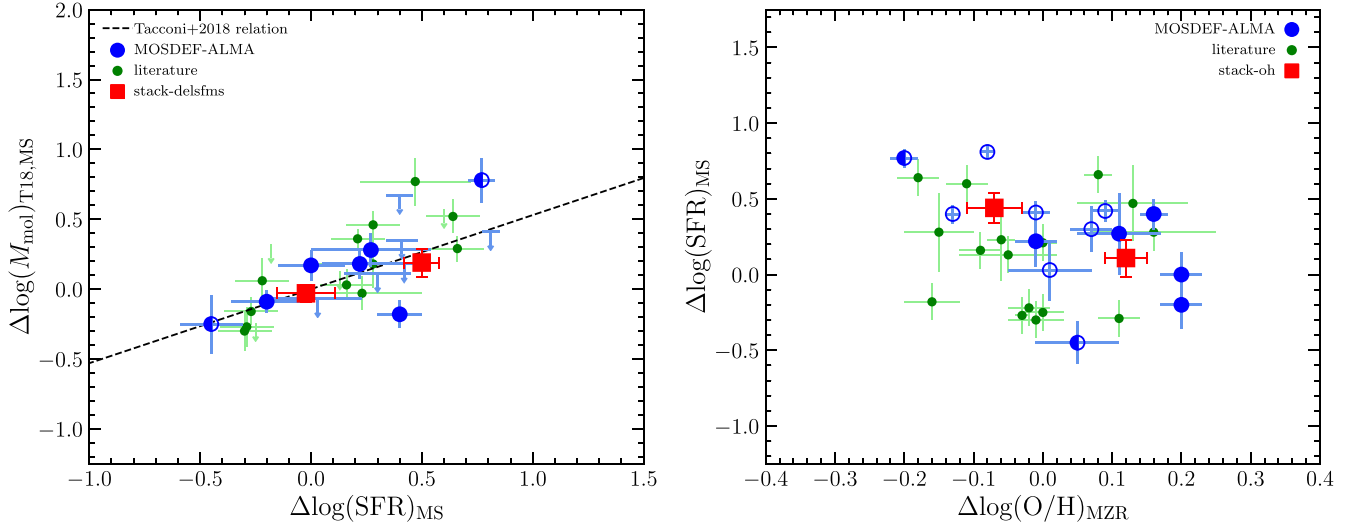


Figure 9. Residual plots comparing offsets from mean scaling relations at fixed M_* . Left: Offset from the Tacconi et al. (2018) M_{mol} scaling relation evaluated at $\Delta \text{SFR}_{\text{MS}} = 0$ vs. offset from the star-forming main sequence. The dashed black line shows the best-fit form of this correlation from Tacconi et al. (2018): $\Delta M_{\text{mol}} \propto \Delta \text{SFR}^{0.53}$. Right: Offset from the star-forming main sequence vs. offset from the mass–metallicity relation. In each panel, red squares denote MOSDEF-ALMA composites in two bins of the x -axis variable.

the signal to be combined across the full range of M_* in the sample, maximizing the ability to recover weak trends.

The left panel of Figure 9 presents $\Delta \log(M_{\text{mol}})_{\text{T18,MS}}$ versus $\Delta \log(\text{SFR})_{\text{MS}}$ for the MOSDEF-ALMA and $z = 2\text{--}3$ literature samples. This comparison is a different way of viewing the $\Delta \log(\text{SFR})_{\text{MS}}$ dependence of M_{mol} at fixed M_* shown in the top panel of Figure 7. We find a positive correlation between these quantities, indicating that galaxies with higher SFR have larger M_{gas} at fixed M_* . The correlation is highly significant: a Spearman correlation test yields $\rho_S = 0.79$ with a p -value = 5.6×10^{-5} . The trends of stacked MOSDEF-ALMA data in two bins of $\Delta \log(\text{SFR})_{\text{MS}}$ (red squares) and the individual objects are consistent with the SFR dependence of the Tacconi et al. (2018) scaling relation ($M_{\text{mol}} \propto \text{SFR}^{0.53}$ at fixed M_*) and the existence of a tight KS relation at $z \sim 2$.

The relation between $\Delta \log(\text{SFR})_{\text{MS}}$ and $\Delta \log(\text{O/H})_{\text{MZR}}$ is shown in the right panel of Figure 9. Focusing on the MOSDEF-ALMA sample, we find evidence of an anticorrelation between these quantities for the individual galaxies, where galaxies above the MS fall below the MZR. This trend is more clearly evident in the MOSDEF-ALMA composites in two bins of $\Delta \log(\text{O/H})_{\text{MZR}}$ (red squares). The observed anticorrelation is a manifestation of the SFR–FMR in which galaxies at fixed M_* with higher SFR have lower O/H. The inverse correlation of $\Delta \log(\text{O/H})_{\text{MZR}}$ on $\Delta \log(\text{SFR})_{\text{MS}}$ has been observed with much higher significance using both individual galaxies and stacked spectra of a considerably larger ($N \sim 250$) MOSDEF $z \sim 2.3$ star-forming sample (Sanders et al. 2018, 2021). Here, we confirm the existence of an SFR–FMR among the 13 MOSDEF-ALMA targets.

There is not a significant correlation present for the literature CO sample in the right panel of Figure 9. This apparent lack of an SFR–FMR may be due to the small sample size or the impact of systematic uncertainties on O/H, or it could be the true physical scenario for this sample. The small sample size of only 16 galaxies can make it difficult to recover the secondary dependence of O/H on SFR in addition to the primary dependence on M_* , considering that there is both intrinsic scatter in the SFR–FMR and several literature sources have fairly large statistical uncertainties on O/H. The metallicities of

the literature sample are derived from a heterogeneous set of strong-line ratios: nine based on N2, six from O3N2, and one from O3O2Ne3. While we have made efforts to control systematics between O/H derived from each of these indicators (see Appendix A), metallicities based on N2 (and O3N2 to a lesser extent) are strongly affected by object-to-object variations in N/O that are commonly a factor of 2 at fixed O/H (Pilyugin & Thuan 2011; Strom et al. 2017, Figure A1). In contrast, the MOSDEF-ALMA sample is more uniform in metallicity indicator, with 11 based on O3O2Ne3 (unaffected by N/O) and two derived using O3N2 (less strongly affected by N/O than N2).

It is also possible that there truly is no dependence of O/H on SFR at fixed M_* in the literature sample. In the local universe, the SFR dependence in the SFR–FMR significantly weakens and may disappear entirely or even invert at high masses ($> 10^{10.5} M_{\odot}$; e.g., Mannucci et al. 2010; Yates et al. 2012). That the massive literature sample (mean $M_* = 10^{10.85} M_{\odot}$) displays no SFR dependence while the less-massive MOSDEF-ALMA sample (mean $M_* = 10^{10.4} M_{\odot}$) does could thus indicate a behavior similar to that of the $z \sim 0$ SFR–FMR at high masses. Uniform full coverage of the rest-optical lines for a larger sample of such massive $z \sim 2$ star-forming galaxies is required in order to discern whether the lack of a correlation is the result of systematic effects or is real.

The top panel of Figure 10 displays $\Delta \log(M_{\text{mol}})_{\text{T18,MS}}$ versus $\Delta \log(\text{O/H})_{\text{MZR}}$. While the trend among individual MOSDEF-ALMA galaxies is unclear due to the large number of limits, there is a clear anticorrelation present for the two stacks in bins of $\Delta \log(\text{O/H})_{\text{MZR}}$ (red squares). This anticorrelation indicates the existence of an $M_*\text{--}M_{\text{mol}}\text{--O/H}$ relation in which galaxies at fixed M_* with higher M_{mol} have lower O/H. This relation has a clear connection to the SFR–FMR (i.e., $M_*\text{--SFR--O/H}$ relation) because the SFR depends on the amount of molecular gas present via the molecular KS relation (Figure 8), such that the SFR–FMR likely emerges because this more fundamental Gas–FMR exists among M_* , M_{mol} , and O/H. We thus expect that, if an SFR–FMR is present, a Gas–FMR will be present as well, as found in the MOSDEF-ALMA sample. We do not find evidence for a Gas–FMR among the

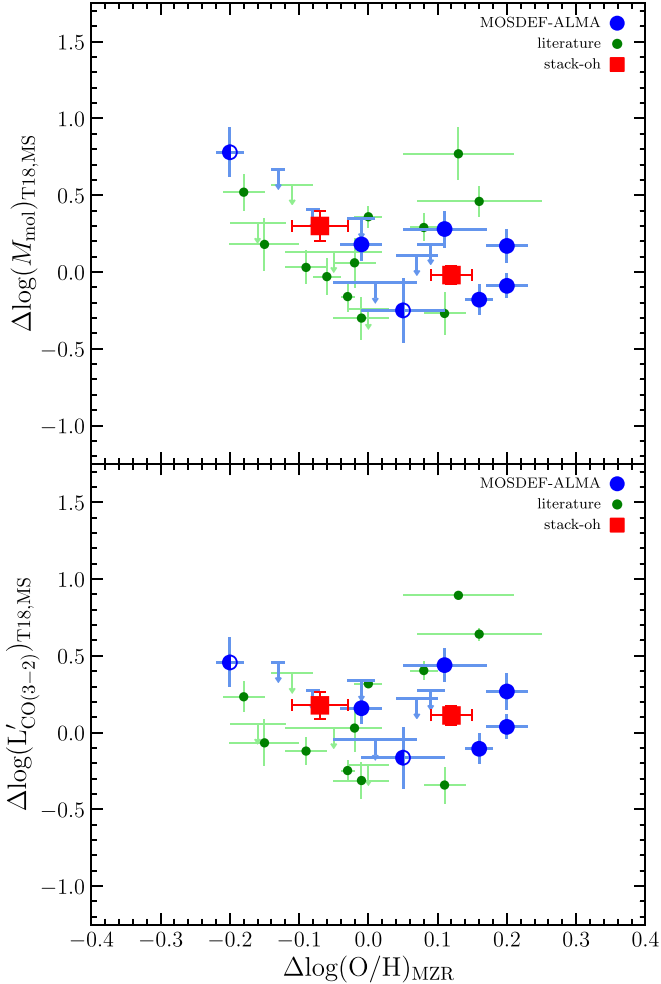


Figure 10. Top: Offset from the Tacconi et al. (2018) M_{mol} scaling relation evaluated at $\Delta SFR_{\text{MS}} = 0$ vs. offset from the mass–metallicity relation. Bottom: Offset from the mean $L'_{\text{CO}(3-2)} - M_*$ relation vs. offset from the mass–metallicity relation. The mean $L'_{\text{CO}(3-2)}$ as a function of M_* and redshift is inferred as follows. Beginning with the Tacconi et al. (2018) M_{mol} relation evaluated at $\Delta SFR_{\text{MS}} = 0$, $L'_{\text{CO}(1-0)}(M_*, z)$ is derived by dividing $M_{\text{mol}}(M_*, z)$ by $\alpha_{\text{CO}}(\text{O/H})$, where O/H is taken from the MZR(M_* , z) parameterization of Equation (1). The resulting function is then multiplied by r_{31} to arrive at $L'_{\text{CO}(3-2)}(M_*, z)$.

more-massive $z = 2\text{--}3$ literature sample, consistent with the lack of an SFR–FMR in the right panel of Figure 9.

Interpreting the top panel of Figure 10 is complicated by the fact that the derived M_{mol} depends on O/H through $\alpha_{\text{CO}}(\text{O/H})$, such that decreasing O/H increases the inferred M_{mol} . To understand the effect $\alpha_{\text{CO}}(\text{O/H})$ has on the $\Delta \log(M_{\text{mol}})_{\text{T18,MS}} - \Delta \log(\text{O/H})_{\text{MZR}}$ anticorrelation, we replace $\Delta \log(M_{\text{mol}})_{\text{T18,MS}}$ with $\Delta \log(L'_{\text{CO}(3-2)})$, the difference in observed $L'_{\text{CO}(3-2)}$ and the mean $L'_{\text{CO}(3-2)}$ at fixed M_* . The mean $L'_{\text{CO}(3-2)}$ as a function of M_* and z is inferred by dividing the Tacconi et al. (2018) $M_{\text{mol}}(M_*, z, \Delta SFR_{\text{MS}} = 0)$ relation by $\alpha_{\text{CO}}(\text{O/H})$, where O/H is inferred from the MZR(M_* , z) given in Equation (1), and finally multiplying by r_{31} . When evaluated at $z = 2.3$, the resulting $L'_{\text{CO}(3-2)}(M_*, z)$ relation is similar to the best-fit $L'_{\text{CO}(3-2)}$ versus M_* relation in the top panel of Figure 4, such that we obtain consistent results if that relation is instead assumed.

The bottom panel of Figure 10 displays $\Delta \log(L'_{\text{CO}(3-2)})_{\text{T18,MS}}$ versus $\Delta \log(\text{O/H})_{\text{MZR}}$. The distribution of MOSDEF-ALMA targets and stacks is flat, such that $L'_{\text{CO}(3-2)}$ has no dependence on O/H at fixed M_* . Consequently, the anticorrelation between

$\Delta \log(M_{\text{mol}})_{\text{T18,MS}}$ and $\Delta \log(\text{O/H})_{\text{MZR}}$ is significantly affected by how α_{CO} depends on metallicity. If α_{CO} has no dependence on O/H, then no Gas–FMR is found in the $z \sim 2$ MOSDEF-ALMA sample. However, we have presented strong evidence for an O/H-dependent α_{CO} in Figure 6. Furthermore, the inverse relation between α_{CO} and O/H is well-established in the local universe (e.g., Bolatto et al. 2013; Accurso et al. 2017) and is thought to be driven by physics that appear to behave similarly at higher redshifts, namely a correlation between metallicity and dust content (Reddy et al. 2010; Shapley et al. 2020, 2022; Popping et al. 2022; Shvarei et al. 2022), and an anticorrelation between metallicity and UV radiation field intensity. We thus conclude that the evidence for an anticorrelation between M_{mol} and O/H at fixed M_* in the MOSDEF-ALMA sample is robust, though the exact slope of this inverse relation will depend on the $\alpha_{\text{CO}}(\text{O/H})$ relation assumed.

4. Discussion

4.1. Signatures of Baryon Cycling at $z \sim 2$

Our analysis of the relations among M_* , SFR, metallicity, and gas content provides strong evidence for the existence of baryon cycling processes that govern the growth of $z \sim 2$ massive galaxies ($\log(M_*/M_{\odot}) \sim 10.0\text{--}11.5$). The typical depletion times of 700 Myr are only $\approx 25\%$ of the age of the universe at $z = 2.3$. Because a star-forming main sequence exists at this redshift, accretion of gas from the IGM and/or CGM is required to sustain star formation in these galaxies, as has been pointed out by previous studies (e.g., Tacconi et al. 2013). However, the gas fractions are not large enough to explain the ISM metallicities at $z \sim 2$. For the typical $\mu_{\text{mol}} \approx 1.5$ and assuming neutral atomic gas is negligible, a simple accreting box model with an accretion rate equal to the SFR predicts $12 + \log(\text{O/H}) = 9.1$, assuming the stellar O yield of core-collapse SNe from a Chabrier (2003) IMF. This value is considerably higher than the average observed $12 + \log(\text{O/H}) = 8.6\text{--}8.7$. Considering the large amount of evidence for ubiquitous high-velocity outflowing gas around high-redshift star-forming galaxies (e.g., Steidel et al. 2010; Förster Schreiber et al. 2019; Weldon et al. 2022), strong gas outflows present a probable candidate mechanism to further decrease the effective yield and drive model ISM metallicities lower toward observed values.

4.1.1. Implications for Outflow Mass Loading

The mass outflow rate (\dot{M}_{out}) is often parameterized in the outflow mass loading factor ($\eta_{\text{out}} = \dot{M}_{\text{out}}/\text{SFR}$) that encapsulates the efficiency with which feedback-driven galactic winds remove mass (and metals) from galaxies. We place quantitative constraints on η_{out} by employing the ideal gas-regulator model of Lilly et al. (2013). In this formalism, the ISM metallicity Z_{ISM} is a function of η_{out} and the gas fraction $\mu_{\text{gas}} = M_{\text{gas}}/M_*$:

$$Z_{\text{ISM}} = Z_0 + \frac{y}{1 + \eta_{\text{out}}(1 - R)^{-1} + \mu_{\text{gas}}}, \quad (15)$$

where y is the stellar metal yield, R is the fraction of stellar mass returned to the ISM through stellar evolutionary processes, and Z_0 is the metallicity of accreting gas. We assume $Z_0 \ll Z_{\text{ISM}}$ such that accreting metals are negligible. We adopt a stellar oxygen yield of $y_O = 0.033$ as a mass fraction

(equivalent to $12+\log(\text{O/H})_y = 9.45$ by number density) and $R = 0.45$, both values appropriate for core-collapse SNe enrichment with a Chabrier (2003) IMF (Vincenzo et al. 2016). Finally, we assume that the total gas mass is dominated by the molecular component in high-redshift star-forming galaxies such that $M_{\text{gas}} \approx M_{\text{mol}}$ (Tacconi et al. 2018), as found in studies of the atomic-to-molecular hydrogen fraction using semi-analytic models (Lagos et al. 2011; Popping et al. 2014, 2015).

The top panel of Figure 11 displays metallicity as a function of μ_{mol} . The black lines show gas-regulator models of Equation (15) with η_{out} varying between 0.5 and 8. We find that the $z \sim 2$ CO sample is generally described by models with η_{out} ranging from 0.5 to 4, with an average value of $\eta_{\text{out}} \approx 2$. Only five galaxies lie in the unphysical region of parameter space that would mathematically require $\eta_{\text{out}} < 0$, though four of these are $\approx 1\sigma$ consistent with the physical region. The data are incompatible with significantly lower stellar yields (i.e., $y_O = 0.015$ for a Salpeter 1955 IMF), which would place a large fraction of the $z \sim 2$ sample in the unphysical regime. Such low yields could only be accommodated if Z_0 is comparable to Z_{ISM} .

Suzuki et al. (2021) found that $z \sim 3.3$ galaxies at $\sim 10^{10.5} M_{\odot}$ have metallicities significantly lower than $z \sim 0$ and $z \sim 1.6$ galaxies at fixed μ_{gas} (where μ_{gas} includes both molecular and atomic components for local galaxies). These authors concluded that there is a sharp increase in η_{out} at fixed μ_{gas} between $z \sim 1.6$ and $z \sim 3$. We find that our $z \sim 2$ sample, with a mean value of $12+\log(\text{O/H}) = 8.6-8.7$ at $\mu_{\text{gas}} = 1.6$, falls near the distribution of the local and $z \sim 1.6$ galaxies at fixed μ_{gas} , implying no strong evolution in η_{out} at fixed μ_{gas} over $z = 0-2.5$. The apparent evolution in η_{out} at fixed μ_{gas} at $z > 3$ found by Suzuki et al. (2021) may be due to systematics associated with converting dust mass to M_{mol} and the metallicity calibrations these authors adopted. Obtaining joint CO and metallicity constraints for $z > 3$ main-sequence galaxies would aid in understanding whether η_{out} is different at $z > 3$.

Using our measured values of O/H and μ_{mol} , we solve Equation (15) for η_{out} and present the resulting values as a function of M_* in the bottom panel of Figure 11. The majority of the combined $z \sim 2$ sample has $\eta_{\text{out}} = 1-4$, with an average value of ≈ 2 and no apparent dependence on M_* over $\log(M_*/M_{\odot}) \sim 10.2-11.2$. The blue line displays an inference of the average η_{out} as a function of M_* for lower-mass main-sequence galaxies, obtained by inputting the best-fit $z \sim 2.3$ MZR of Sanders et al. (2021) and the Tacconi et al. (2018) μ_{mol} scaling relation into Equation (15), assuming the same y_O and R as above. As found by Sanders et al. (2021), η_{out} decreases with increasing M_* up to $10^{10.5} M_{\odot}$ as $\eta_{\text{out}} \propto M_*^{-1/3}$, at which point the blue line aligns with the average value of the higher-mass CO sample. The CO-based results suggest that η_{out} does not continue falling with increasing M_* above $10^{10.5} M_{\odot}$, but instead flattens out. A similar behavior is inferred on average for $z \sim 0$ galaxies (dashed black line). Given that $\eta_{\text{out}} > 1$ even at the highest masses, the flattening of η_{out} with respect to M_* is responsible for the flattening of the MZR at high masses (Figure 3). As Sanders et al. (2021) noted, the lower-mass inferences based on the MZR suggest that, at fixed M_* , η_{out} is larger at $z \sim 2$ than at $z \sim 0$. This does not appear to be the case at $> 10^{10.5} M_{\odot}$, where both low- and high-redshift galaxies are inferred to have similar η_{out} on average.

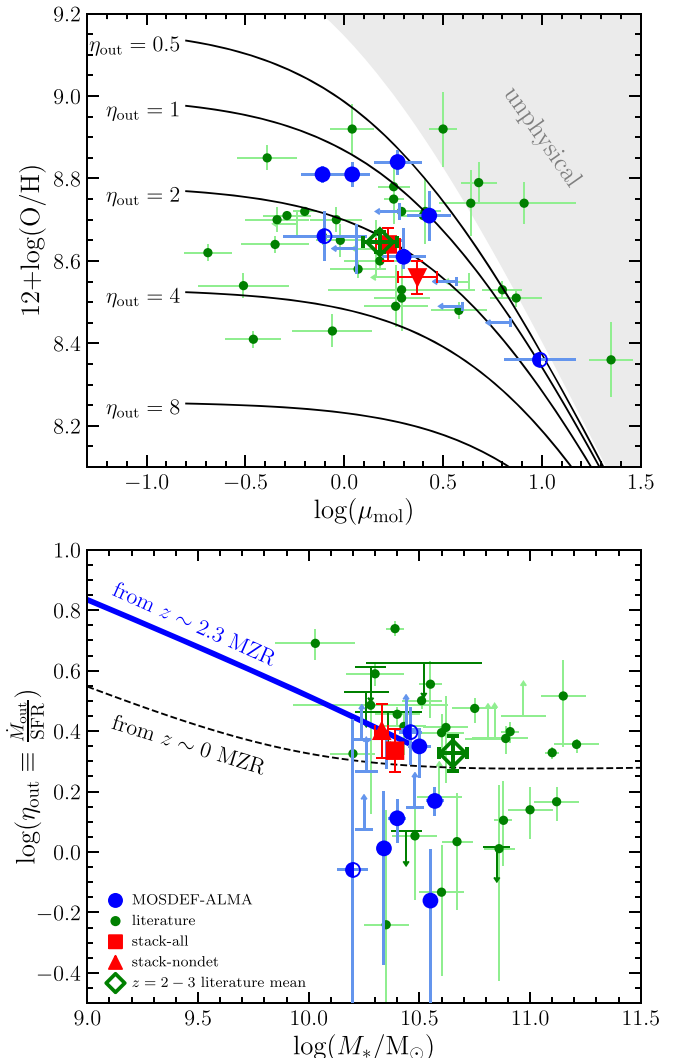


Figure 11. Top: Gas-phase metallicity vs. molecular gas fraction. Black lines show the gas-regulator model of Lilly et al. (2013) evaluated at outflow mass-loading factors of $\eta_{\text{out}} = 0.5$ to 8. The gray shaded region requires $\eta_{\text{out}} < 0$ and is thus unphysical. Bottom: η_{out} vs. M_* , where η_{out} is inferred from the Lilly et al. (2013) gas-regulator model. The thick blue line shows an inference of $\eta_{\text{out}}(M_*)$ at $z \sim 2.3$ obtained by combining the best-fit $z \sim 2.3$ MZR from Sanders et al. (2021) and the Tacconi et al. (2018) μ_{mol} scaling relation evaluated at $z = 2.3$ and $\Delta \text{SFR}_{\text{MS}} = 0$. The dashed black line shows $\eta_{\text{out}}(M_*)$ at $z \sim 0$ inferred from the combination of the local MZR of Curti et al. (2020) and the $z \sim 0$ μ_{gas} scaling relation of Saintonge et al. (2016) evaluated on the MS.

In the EAGLE simulations, Mitchell et al. (2020) found that η_{out} falls roughly as a power law with M_* even out to very high masses when AGN feedback is not included, while including AGN feedback causes η_{out} to flatten out above halo masses of $\sim 10^{12} M_{\odot}$ ($M_* \sim 10^{10} M_{\odot}$). Nelson et al. (2019) see a flattening of η_{out} toward high masses and eventual steep increase of η_{out} with M_* at very high masses that are attributed to AGN feedback in IllustrisTNG. Other analyses of cosmological simulations have found that the flattening of the MZR at high masses requires the inclusion of AGN feedback (e.g., De Rossi et al. 2015; Ma et al. 2016; De Rossi et al. 2017).

While we have excluded AGN from our sample, the tracers used to identify AGN (X-ray luminosity, near-IR colors tracing hot dust, and rest-optical line ratios) can only identify galaxies with contemporaneous high rates of black hole accretion. Galaxies with AGN activity in the recent past but low levels of

black hole accretion in the present would correctly be identified as star-forming, though AGN feedback may have a lasting effect on ISM gas via material removal or gas heating that makes it easier for SNe feedback to drive outflows. This scenario is consistent with the idea that supermassive black hole accretion rates trace SFRs (in turn tracing gas inflow rates) on average (Madau & Dickinson 2014), while maintaining significant variability such that galaxies alternate between an “on” AGN phase and “off” star formation dominated phase (Heckman & Best 2014; Hickox et al. 2014). We speculate that the transition from a power-law $\eta_{\text{out}}(M_*)$ to a flat η_{out} occurs at the mass above which the AGN duty cycle becomes high enough that the imprint of AGN feedback on ISM gas does not have time to be erased between consecutive AGN “on” phases, providing a physical driver for observed MZR flattening at high masses. The occurrence rate of strong AGN rises steeply above the mass at which the MZR begins to flatten at $z \sim 0$ (e.g., Kauffmann et al. 2004; Aird et al. 2019). Using the KMOS^{3D} sample at $z = 0.6\text{--}2.7$, Förster Schreiber et al. (2019) found that the occurrence rates of both AGN and AGN-driven outflows grow steeply with increasing M_* and exceed 10% at $M_* > 10^{10.5} M_\odot$, similar to the mass where we find the onset of MZR and η_{out} flattening at $z \sim 2$. While these results are generally consistent with intermittent AGN feedback as a driver of high-mass MZR flattening at $z \sim 2$, robustly evaluating this scenario will require better quantitative constraints on the turnover mass of the $z \sim 2$ MZR to directly compare to measures of AGN frequency as a function of M_* .

4.1.2. The Role of Accretion Rate in Scaling Relations at $z \sim 2$

The (anti-)correlated residuals around the MS, MZR, and $M_{\text{mol}}-M_*$ relation displayed in Figures 9 and 10 demonstrate the existence of a multidimensional relation among M_* , SFR, M_{mol} , and metallicity in the $z \sim 2$ MOSDEF-ALMA sample. This relation is such that, at fixed M_* , galaxies with higher gas masses have higher SFR and lower metallicity. Such trends are found in a range of cosmological simulations (e.g., Ma et al. 2016; Davé et al. 2017; De Rossi et al. 2017; Torrey et al. 2018; Davé et al. 2019; Torrey et al. 2019), and are a staple of models of galaxy evolution based on a self-regulating baryon cycle (Davé et al. 2012; Lilly et al. 2013; Peng & Maiolino 2014). These trends have also been observed in $z \sim 0$ star-forming galaxy populations as the SFR-FMR and Gas-FMR (Lara-López et al. 2010; Mannucci et al. 2010; Bothwell et al. 2013; Hughes et al. 2013; Lara-López et al. 2013; Bothwell et al. 2016a, 2016b; Brown et al. 2018). Evidence for an SFR-FMR at $z > 1$ has been found previously (Zahid et al. 2014; Sanders et al. 2018; Henry et al. 2021; Sanders et al. 2021), while hints of a Gas-FMR have been found at $z \sim 1.4$ (Seko et al. 2016). Here, we confirm the interdependent nature of these four properties and the simultaneous existence of the SFR-FMR and Gas-FMR at high redshift for the first time.

The correlated residuals in M_{mol} , SFR, and metallicity can be explained if deviations of M_{mol} from the mean reflect variations in the gas inflow rate, \dot{M}_{in} . The observed trends then indicate that higher \dot{M}_{in} drives larger SFR due to the availability of more cold gas while simultaneously diluting metals in the ISM as metal-poor gas is mixed in, lowering O/H. This scenario implies that the scatter of the MS, MZR, and $M_{\text{mol}}-M_*$ relations are all primarily driven by variations in accretion rates, a conclusion reached by previous works

modeling the SFR-FMR and Gas-FMR (Dayal et al. 2013; Ford et al. 2014; Brown et al. 2018; Torrey et al. 2019). The simultaneous existence of a correlation between $\Delta \log(M_{\text{mol}})_{\text{T18,MS}}$ and $\Delta \log(\text{SFR})_{\text{MS}}$ and an anticorrelation between $\Delta \log(M_{\text{mol}})_{\text{T18,MS}}$ and $\Delta \log(\text{O/H})_{\text{MZR}}$ requires that SFR and metallicity respond to the accretion of fresh gas quickly, faster than the timescale of significant variations in the inflow rate, as is seen in cosmological simulations (Muratov et al. 2015; Torrey et al. 2018, 2019). Indeed, the dynamical timescales of $z \sim 2$ galaxy disks (on which galaxy-averaged SFR and metallicity can vary) are a few tens of Myr (e.g., Förster Schreiber et al. 2006; Reddy et al. 2012), while halo dynamical times (on which \dot{M}_{in} from smooth gas accretion is expected to vary) are roughly an order of magnitude larger (e.g., Torrey et al. 2018). The overall tightness of these three scaling relations (1σ scatter = 0.1–0.3 dex at fixed M_*) then suggests that large variations in \dot{M}_{in} averaged over the SFR and O/H response timescale (i.e., disk dynamical time, $\sim 30\text{--}50$ Myr) are rare.

Comparing the observed quantitative slopes of these correlated residual relations to those produced in numerical simulations and semi-analytic models of galaxy formation presents an avenue to make high-order tests of accretion and feedback models (e.g., Davé et al. 2017; Torrey et al. 2019; Pandya et al. 2020). The slopes are not well-constrained with the current $z \sim 2$ MOSDEF-ALMA sample, due to the small sample size and data quality. This work motivates a larger and deeper survey of CO in $z \sim 2$ galaxies with accompanying metallicity measurements to quantitatively constrain the secondary dependence on gas mass.

4.2. ISM Metal Mass and Retention

The total metal mass in the ISM can be estimated from the combination of metallicity and gas mass. We convert from the number density $12+\log(\text{O/H})$ to a mass fraction $Z_O = M_O/M_{\text{gas}}$, assuming He makes up 36% of the gas mass, and then we use the ratio of the oxygen and total metal stellar yields $y_O/y_Z = 0.6$ ¹⁶ to infer the total gas-phase ISM metal mass fraction $Z_{\text{ISM}} = M_Z/M_{\text{gas}}$. We then multiply Z_{ISM} by M_{mol} , assuming $M_{\text{mol}} \approx M_{\text{gas}}$ for the $z \sim 2$ sources, to obtain the mass of metals in the ISM, $M_{Z,\text{ISM}}$. The top panel of Figure 12 shows that $M_{Z,\text{ISM}}$ increases with increasing M_* on average (i.e., for the composites), as expected because both metallicity and M_{mol} increase with increasing M_* . The typical ISM metal mass of $z \sim 2$ star-forming galaxies is $M_{Z,\text{ISM}} \approx 10^{8.7} M_\odot$ at $M_* = 10^{10.5} M_\odot$.

The ratio of gas-phase ISM metal mass to galaxy stellar mass has been used as a measure of a galaxy’s ability to retain metals because M_* is approximately proportional to the total metals produced over a galaxy lifetime (Ma et al. 2016; Torrey et al. 2019). Torrey et al. (2019) defined this quantity as the ISM metal retention efficiency, $\gamma_{Z,\text{ISM}} = M_{Z,\text{ISM}}/M_*$, and argued that evolving gas fractions, not outflow efficiencies, control the evolution of the MZR because higher-redshift galaxies in IllustrisTNG have higher $\gamma_{Z,\text{ISM}}$ at fixed M_* and are thus

¹⁶ We used the IMF-integrated core-collapse SNe yields of Vincenzo et al. (2016) for a Chabrier (2003) IMF and the Nomoto et al. (2013) yield tables. The O-to-total metals mass fraction is lower for systems significantly enriched by Type Ia SNe (e.g., 0.43 for a solar abundance pattern). There is evidence that the enrichment of $z \sim 2$ star-forming galaxies is dominated by core-collapse SNe with little contribution from Type Ia (Steidel et al. 2016; Strom et al. 2018; Topping et al. 2020a; Sanders et al. 2020b; Topping et al. 2020b).

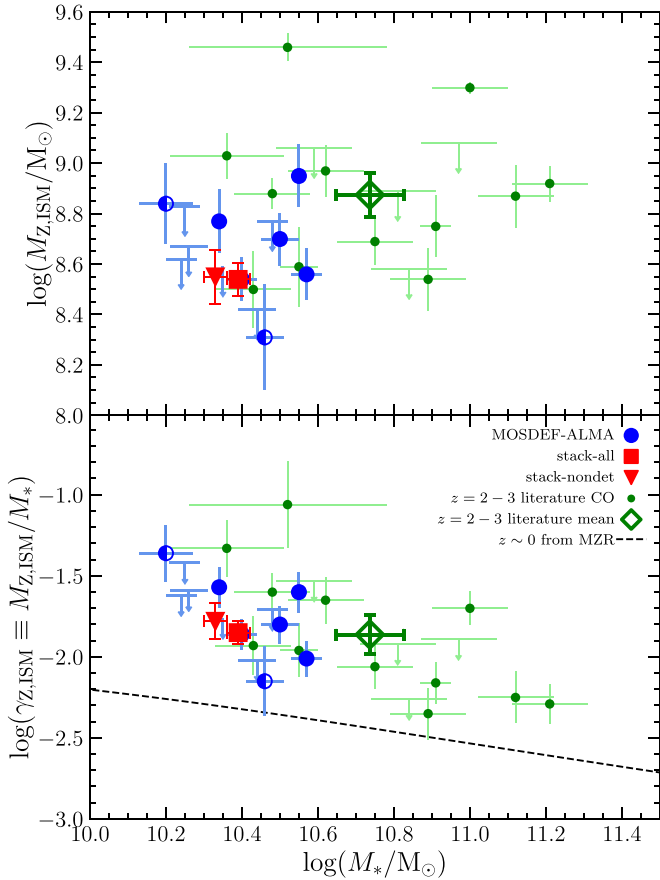


Figure 12. Top: Total metal mass in the gas-phase ISM vs. stellar mass. Bottom: The retained metal yield of the ISM vs. stellar mass. The black dashed line represents the mean relation at $z \sim 0$ derived by combining the MZR of Curti et al. (2020) with M_{gas} ($M_{\text{HI}} + M_{\text{mol}}$) inferred from the scaling relation of Saintonge et al. (2016) evaluated on the main sequence.

inferred to be more efficient at retaining gas-phase metals than their low-redshift counterparts. We plot $\gamma_{Z,\text{ISM}}$ versus M_* in the bottom panel of Figure 12 and find that the combined $z \sim 2$ sample indeed displays ISM metal retention efficiencies at fixed M_* that are higher by a factor of ~ 3 than the mean value at $z \sim 0$ (black dashed line).

This result implies that $z \sim 2$ galaxies at $\log(M_*/M_\odot) \sim 10.5\text{--}11$ are less efficient at ejecting metals, seemingly in conflict with the result based on gas-regulator models that η_{out} is the same on average at $z \sim 2$ and $z \sim 0$ over this mass range (Figure 11, bottom panel). In their analysis of the MZR in the IllustrisTNG simulations, Torrey et al. (2019) pointed out the tension between $\gamma_{Z,\text{ISM}}$, which implies that gas fraction primarily governs the MZR shape and its evolution (see also Ma et al. 2016), and analyses based on gas-regulator or equilibrium models in which outflow efficiency is inferred to play the larger role (e.g., Peeples & Shankar 2011; Davé et al. 2012; Lilly et al. 2013; Sanders et al. 2021). Torrey et al. (2019) argued that the importance of outflows is overestimated when using current gas-regulator models because they are not properly treating potentially important physical processes known to occur in numerical simulations, notably the recycling of enriched, previously outflowing material (Finlator & Davé 2008; Muratov et al. 2015; Anglés-Alcázar et al. 2017; Muratov et al. 2017; Pandya et al. 2020). Theoretical work has shown close connections between η_{out} and μ_{gas} or Σ_{gas} (Hayward & Hopkins 2017; Kim et al. 2020), such that

the action of outflows versus gas fraction in setting the ISM metallicity may not be cleanly separable. We will revisit the apparent tension between Figures 11 and 12 at the end of Section 4.3.

4.3. A Budget of Metals in Massive $z \sim 2$ Star-forming Galaxies

We now combine the ISM metal mass calculated above in Section 4.2 with estimates of the metal mass in stars and dust, to perform a simple metal budget analysis. We carry out this analysis on the sample averages of the MOSDEF-ALMA and $z = 2\text{--}3$ literature samples. We estimate the mass of metals locked in stars, $M_{Z,\text{stars}}$, by multiplying the stellar metallicity by M_* , assuming the stellar metallicity is equal to the current gas-phase metallicity. This approach likely overestimates the true $M_{Z,\text{stars}}$ because ISM metallicity increases with time, on average, such that only recently formed stars will have metallicity equal to that of the current ISM, while previous generations of stars should have lower metallicity. The mass of metals in dust, $M_{Z,\text{dust}}$, is taken to be the total dust mass because dust grains are essentially entirely composed of metals. To estimate $M_{Z,\text{dust}}$, we combine the gas mass with the dust-to-gas ratio as a function of O/H from De Vis et al. (2019),¹⁷ which is consistent with current dust-to-gas constraints at $z \sim 2$ (Shapley et al. 2020; Popping et al. 2022). As before, we assume that $M_{\text{gas}} \approx M_{\text{mol}}$ in high-redshift star-forming galaxies (Lagos et al. 2011; Popping et al. 2014, 2015; Tacconi et al. 2018). The lifetime metal production is calculated by first dividing M_* by (1-R), to infer the lifetime total stellar mass produced, and then multiplying the resulting value by the stellar metal yield. We adopt $y_Z = 0.051$ and $R = 0.45$ for a Chabrier (2003) IMF (Vincenzo et al. 2016).

The left panel of Figure 13 displays the mass of metals in the ISM, stars, dust, and the sum total of metals accounted for inside galaxies compared to the lifetime metal mass produced for the $z \sim 2$ samples. We find that the majority of metals inside $z \sim 2$ galaxies reside in the gas-phase ISM, even at very high M_* . This is unlike what is found at $z \sim 0$, where only low-mass galaxies at $M_* < 10^{10} M_\odot$ have most of their metals in the ISM, while the majority of metals in more massive local galaxies resides in stars (Peeples et al. 2014; Oppenheimer et al. 2016; Muratov et al. 2017). This difference can be attributed to the steep increase of μ_{gas} with redshift: $z \sim 2$ galaxies have roughly an order of magnitude larger M_{gas} than $z \sim 0$ galaxies at fixed M_* . Dust appears to be a subdominant destination for metals at $z \sim 2$, similarly to $z \sim 0$. Our dust mass estimates, based on a dust-to-gas ratio, are ~ 0.2 dex lower than those derived from ALMA dust continuum measurements of $z \sim 2.3$ galaxies at similar M_* by Shvarei et al. (2022). Even if $M_{Z,\text{dust}}$ was larger by that amount, it would remain smaller than $M_{Z,\text{ISM}}$ and $M_{Z,\text{stars}}$.

The fraction of metals accounted for relative to the lifetime metal mass produced is presented in the right panel of Figure 13. The metal mass accounted for in the ISM, stars, and dust makes up only $30\% \pm 4\%$ of the total metals produced, implying that the majority of produced metals have been ejected from the galaxies in our samples and reside in either the CGM or IGM. This value is very similar to the 25% average metal retention fraction derived for $z \sim 0$ galaxies by

¹⁷ We use their parameterization based on the Pettini & Pagel (2004) O3N2 metallicity calibration.

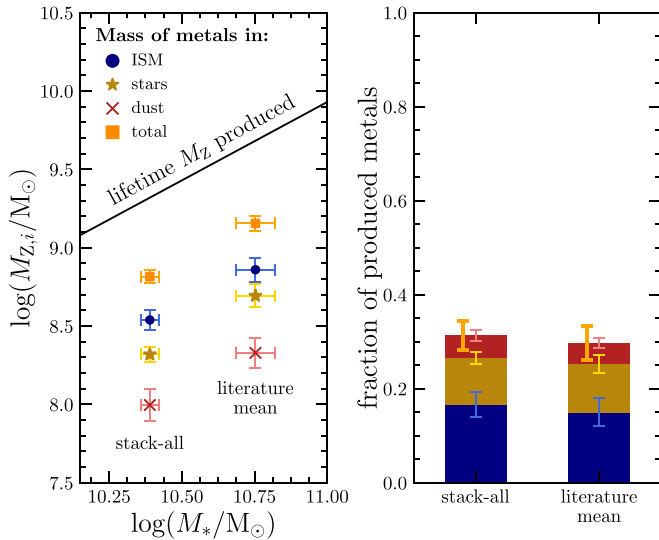


Figure 13. A budget of metals in star-forming galaxies at $z = 2$ –3. Data are shown for the composite spectrum of all MOSDEF-ALMA targets (stack-all) at lower mass and the mean of the $z = 2$ –3 literature CO+O/H sample at higher mass. Left: The mass of metals in different phases vs. M_* . Metal mass has been estimated for the gas-phase ISM (blue circle), stars (yellow star), interstellar dust (red “x”), and the sum of these three components representing the total metal mass accounted for within the galaxy (orange square). The black line shows the estimated total metal mass produced. Right: Fraction of total produced metals accounted for in the ISM, stars, and dust, obtained by dividing the metal mass in each phase by the lifetime metal mass produced. The orange error bar shows the cumulative uncertainty on the sum. The $\approx 70\%$ of produced metals that are unaccounted for are inferred to be lost to the CGM and IGM.

Peeples et al. (2014) using similar metal budgeting techniques, and is also close to that of $\sim 10^{10} M_\odot$ galaxies at $z = 2$ in the FIRE simulations (Muratov et al. 2017). The metal loss fraction of 70% does not show variation across the mass range spanned by the $z \sim 2$ samples, again similar to the behavior at $z \sim 0$ (Peeples et al. 2014; Oppenheimer et al. 2016) despite large differences in global properties such as μ_{gas} , SFR, and Σ_{SFR} that are thought to be related to outflow strength. This analysis predicts a large mass of metals in the CGM of $z \sim 2$ star-forming galaxies, with $M_{Z,\text{CGM}} \sim 10^9 M_\odot$ at $M_* = 10^{10.5} M_\odot$. Significant metal absorption from low- and high-ionization species has been observed in the CGM of $z \sim 2$ galaxies (e.g., Adelberger et al. 2005; Steidel et al. 2010; Rudie et al. 2019). Recently, Rudie et al. (2019) found that the mass of metals in the CGM of $M_* \sim 10^{10} M_\odot$ $z \sim 2$ galaxies is $> 25\%$ of $M_{Z,\text{ISM}}$, alongside evidence that metal ejection from the halo into the IGM may be common. Improved observational constraints on the CGM metal mass of high-redshift galaxies are needed to see if the missing metals in Figure 13 can be accounted for.

The fact that the total metal retention fraction is found to be $\approx 30\%$ for galaxies at $\log(M_*/M_\odot) \sim 10.5$ at both $z \sim 0$ and $z \sim 2$ implies that they have a similar efficiency of metal ejection, consistent with our inferences of η_{out} at both redshifts in the bottom panel of Figure 11. We can now understand the apparent tension in the evolution of the ISM metal retention efficiency, $\gamma_{Z,\text{ISM}}$, at fixed M_* in Figure 12 toward higher metal retention with increasing redshift. As a consequence of their large gas fractions (i.e., $M_{\text{gas}} > M_*$), $z \sim 2$ galaxies store the largest fraction of their metals in the gas-phase ISM, with smaller contributions from stars and dust. In contrast, gas fractions are low at $z \sim 0$ ($M_{\text{gas}} \approx 0.2 M_*$ at $\sim 10^{10.5} M_\odot$), such that the vast majority of metals are stored in stars and only a small part is in the ISM for local galaxies in this mass range

(Peeples et al. 2014). Thus, the evolution of $\gamma_{Z,\text{ISM}}$ at fixed M_* in Figure 12 reflects an increasing fraction of total metals stored in the gas-phase ISM with increasing redshift as a consequence of higher μ_{gas} , rather than a higher overall metal retention (and lower metal ejection efficiency) at higher redshift.

We therefore do not find any tension between analyses based on gas-regulator models and metal retention fractions, but stress that galaxy metal retention (and its evolution with redshift) cannot be properly evaluated using metals in the gas-phase ISM alone because the relative contribution of this phase to the total metal mass changes as a function of both M_* and redshift. This finding suggests that the missing physics (e.g., outflow recycling) in current gas-regulator models may not be required to obtain a reasonably accurate understanding of the origin and evolution of the MZR, though this problem ultimately requires the development of analytic models including these high-order processes to evaluate the impact of their inclusion or exclusion. In Figure 11, inferences at lower masses from the MZR suggest that η_{out} increases with increasing redshift below $10^{10} M_\odot$. Accordingly, we expect the total metal retention fraction to be lower at $z \sim 2$ than at $z \sim 0$ at fixed M_* for low-mass systems. This motivates an analysis of the metal budget at $z \sim 2$ across a wider mass range, which we will address in future work.

4.4. Cold Gas Content Scaling Relations at $z \sim 2$

Recent studies have calibrated scaling relations of M_{mol} , μ_{mol} , and t_{depl} as a function of redshift, M_* , and SFR (or equivalently, offset from the MS) by combining samples with Rayleigh–Jeans dust continuum and/or CO line emission observations spanning $z = 0$ –4 (Genzel et al. 2015; Scoville et al. 2017; Tacconi et al. 2018; Liu et al. 2019; Tacconi et al. 2020; Wang et al. 2022). These scaling relations potentially offer great utility by providing estimates of the cold gas content of galaxies based on galaxy properties that are easier to directly constrain. However, at $z \geq 2$, the samples used to calibrate such scaling relations are composed of massive galaxies ($M_* \gtrsim 10^{10.5} M_\odot$) such that using these relations to estimate gas masses of lower-mass high-redshift galaxies requires extrapolation. Furthermore, the vast majority (and in some works entirely) of galaxies in the $z > 1$ calibration samples have gas mass measurements based on dust continuum emission, while only a small fraction have CO-based M_{mol} . Using the combination of the lower-mass MOSDEF-ALMA and more-massive literature CO samples in this work, we can evaluate which cold gas scaling relations are reliable at $z \sim 2$.

The scaling relations of Scoville et al. (2017), Tacconi et al. (2018), and Liu et al. (2019) are displayed in each panel of Figure 7, all evaluated at $z = 2.3$ for galaxies on the MS. We find that the scaling relation of Tacconi et al. (2018) reliably reproduces CO-based M_{mol} and μ_{mol} of main-sequence galaxies on average (gray square and colored diamond) down to $10^{10.4} M_\odot$, in particular having a slope that matches the observed trend with M_* . In contrast, the Scoville et al. (2017) and Liu et al. (2019) relations have slopes as a function of M_* that are too shallow for M_{mol} and too steep for μ_{mol} , suggesting that these relations will overestimate gas mass when extrapolating to $M_* \lesssim 10^{10} M_\odot$. The normalization of the Scoville et al. (2017) relation is too high across the full range of masses probed by the $z \sim 2$ CO sample, while the Liu et al. (2019) relation underestimates M_{mol} and μ_{mol} at $\sim 10^{11} M_\odot$. The good match between the relation of Tacconi et al. (2018) and the

CO-based mean values suggests that the Tacconi et al. (2018) parameterization is more reliable when extrapolating to lower masses.

The form of the $z \sim 2$ $M_{\text{mol}}-M_*$ relation has recently been investigated at low stellar masses ($\log(M_*/M_\odot) \sim 9.5-10.5$) by Solimano et al. (2021) using CO observations of strongly lensed galaxies. These authors found that lensed $z \sim 2$ galaxies in this mass range fall 0.5–1 dex below the extrapolation of the Tacconi et al. (2018) relation. There is thus tension between results based on strongly lensed galaxies and field galaxies (this work) as to whether the Tacconi et al. (2018) is reliable toward low M_* . At the low metallicities of such low- M_* lensed sources, the correction due to the α_{CO} factor is very large and systematic uncertainty on the $\alpha_{\text{CO}}(\text{O/H})$ relation may contribute to this offset. Differential lensing of the CO and nebular line emitting gas may also introduce systematic effects for galaxies as highly magnified ($>30\times$) as those in the sample of Solimano et al. (2021). Deep CO observations of unlensed galaxies in a mass range overlapping the lensed sample are ultimately needed to understand whether low- M_* $z \sim 2$ galaxies follow the Tacconi et al. (2018) relation at $\lesssim 10^{10} M_\odot$.

We found little dependence of t_{depl} on M_* in Figure 7, with lower-mass galaxies having marginally smaller t_{depl} . Both the Scoville et al. (2017) relation that has no mass dependence and the relation of Tacconi et al. (2018) with $t_{\text{depl}} \propto M_*^{0.09 \pm 0.05}$ are consistent with the observed M_* scaling within the uncertainties. The Liu et al. (2019) dependence ($t_{\text{depl}} \propto M_*^{-0.52}$) is clearly too steep to match the CO-based t_{depl} and would severely overestimate t_{depl} at lower M_* . The Scoville et al. (2017) and Tacconi et al. (2018) relations bracket the observations in normalization, with the former slightly higher and the latter slightly lower.

The SFR dependence of M_{mol} and μ_{mol} at fixed M_* is nearly identical for Tacconi et al. (2018) and Liu et al. (2019) ($\mu_{\text{mol}} \propto (\text{SFR/SFR}_{\text{MS}})^{0.53}$), matching the observed trend in Figure 9, left panel. Scoville et al. (2017) find $\mu_{\text{mol}} \propto (\text{SFR/SFR}_{\text{MS}})^{0.32}$, significantly shallower than the CO-based constraints at $z \sim 2$. In summary, we find that the Tacconi et al. (2018) scaling relations provide the best overall match to the CO-based observations for estimates of M_{mol} , μ_{mol} , and t_{depl} as a function of M_* and SFR at $z \sim 2$, and provide a particularly good match in mass dependence, suggesting extrapolation to lower masses is reliable.¹⁸

4.5. Prospects for Detecting CO of Low-mass High-redshift Galaxies with ALMA

With the MOSDEF-ALMA sample, we have pushed the stellar mass of $z \sim 2$ main-sequence galaxies with CO-based M_{mol} down by a factor of 2, from $10^{10.7} M_\odot$ to $10^{10.4} M_\odot$. It is of interest to investigate the prospects of detecting CO emission in even lower-mass $z \sim 2$ galaxies to expand the dynamic range of parameter space probed by CO in the M_* -SFR plane. We estimated the integrated CO(3–2) line flux, $S_{\text{CO}(3-2)}$, for $z = 2.3$ galaxies on the MS by combining Equations (4) and (1) to estimate $L'_{\text{CO}(3-2)}/\text{SFR}$ as a function of M_* , using the

¹⁸ While the majority of our $z = 2-3$ literature CO sample was included in the Tacconi et al. (2018) calibration sample, $<25\%$ of their $z > 1$ sample have CO measurements, with the vast majority based on dust continuum. The good match of the Tacconi et al. (2018) scaling relations to the CO-based measurements is thus not by construction, because this small subset of their total sample would not dominate during the fitting process.

$z = 2.3$ MS of Speagle et al. (2014) to convert to $L'_{\text{CO}(3-2)}$, and finally obtaining $S_{\text{CO}(3-2)}$ with Equation (2). We then inferred $S_{\text{CO}(3-2)}$ for offsets above and below the MS using the best-fit SFR dependence of $L'_{\text{CO}(3-2)}$ at fixed M_* : $L'_{\text{CO}(3-2)} \propto (\text{SFR/SFR}_{\text{MS}})^{0.71}$ (Equation (3)).

The predicted $S_{\text{CO}(3-2)}$ at $z = 2.3$ across the M_* -SFR plane is displayed in Figure 14. We converted $S_{\text{CO}(3-2)}$ to the peak line flux density assuming a velocity FWHM of 150 km s^{-1} , the average value for $z \sim 2.3$ galaxies in the MOSDEF survey spanning $\log(M_*/M_\odot) = 9.0-10.5$ (Price et al. 2016). We then used this peak flux density to estimate the required integration time with ALMA to detect CO(3–2) across the M_* -SFR plane. We employed the ALMA Sensitivity Calculator¹⁹ to calculate the rms sensitivity for different on-source integration times. We assumed an observed frequency of 104.8 GHz (CO(3–2) at $z = 2.3$) that falls in ALMA Receiver Band 3, an equatorial target (e.g., the COSMOS field), and a bandwidth of 50 km s^{-1} equal to $1/3$ of the line FWHM for the rms calculations. Using Monte Carlo simulations, we found that integrated line $S/\text{N} = 4$ is obtained if the rms value integrated over $1/3$ of the line FWHM is 3.5 times smaller than the line peak. For a given integration time, we identified the contour in the M_* -SFR plane for which the line peak is 3.5 times the rms value, above which galaxies will have integrated CO(3–2) $S/\text{N} > 4$.

The blue, green, orange, and red lines show contours where the integrated line flux has $S/\text{N} = 4$ in on-source integration times of 1, 2.5, 5, and 10 hr, respectively. Integrations of ~ 1 hr on-source reach the current mass limit of $10^{10.4} M_\odot$ on the MS. At $z \sim 2.3$, a survey with 5 h on-source will reach $10^{10} M_\odot$ on the MS, $10^{9.7} M_\odot$ for moderate starbursts ($3 \times \text{MS}$), and $10^{9.4} M_\odot$ for extreme starbursts ($10 \times \text{MS}$). Such a survey could nearly double the parameter space containing galaxies with CO detections at $z \sim 2$ relative to the current sample, probing a regime that significantly overlaps with samples from large spectroscopic surveys for which detailed metallicity, SFR, dust reddening, and ionization constraints are available. Detecting CO(3–2) in main-sequence galaxies at masses significantly below $10^{10} M_\odot$ would require prohibitively long integrations with ALMA and is thus not a feasible route to constrain the gas masses of these targets. More promising strategies to reach lower masses include measuring CO in gravitationally lensed galaxies (e.g., Saintonge et al. 2013; Dessauges-Zavadsky et al. 2015, 2017; González-López et al. 2017; Dessauges-Zavadsky et al. 2019; Solimano et al. 2021), where even modest magnification factors of 3–5 would lead to significant gains in efficiency, or deriving M_{mol} from the Rayleigh–Jeans dust continuum, which has proven to be detectable with ALMA in shorter integration times than are required for CO (e.g., Kaasinen et al. 2019; Aravena et al. 2020; Suzuki et al. 2021; Shvaei et al. 2022).

5. Summary and Conclusions

We have analyzed ALMA observations of CO(3–2) for a sample of 13 moderate-mass main-sequence galaxies at $z \sim 2.3$ that uniquely have near-infrared spectra from the MOSDEF survey covering the full set of strong rest-optical emission lines, from which we have derived gas-phase metallicities. We supplemented the MOSDEF-ALMA sample with a sample of more massive $z = 2-3$ main-sequence galaxies from the literature with existing CO and metallicity constraints. The

¹⁹ <https://almascience.eso.org/proposing/sensitivity-calculator>

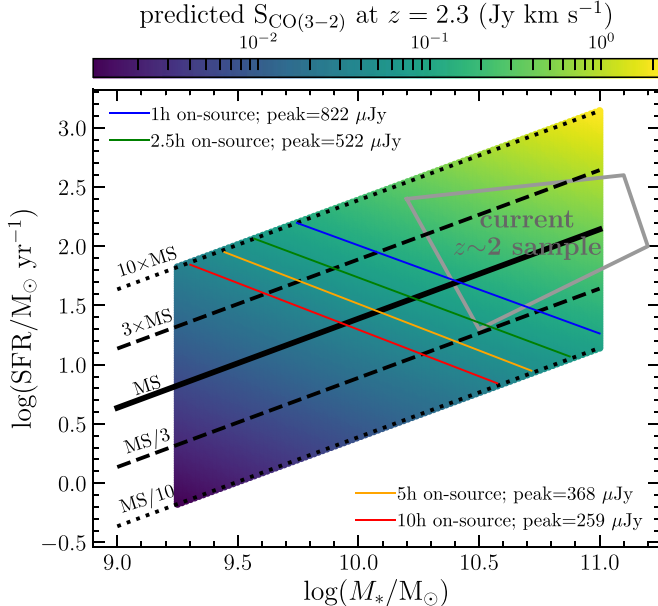


Figure 14. Predicted integrated CO(3–2) line flux, $S_{\text{CO}(3-2)}$, as a function of M_* and SFR for galaxies at $z = 2.3$. $S_{\text{CO}(3-2)}$ is estimated as described in the text. Colored lines show contours with integrated CO(3–2) S/N = 4 in a given on-source integration time with ALMA, with the integration time and flux density of the line peak given in the legend. The rms sensitivity over a 50 km s $^{-1}$ bandwidth is equal to the peak flux density divided by 3.5. The range of M_* and SFR for the current $z \sim 2$ CO sample employed in this work is outlined by the thick gray line. The solid black line traces the star-forming main sequence at $z = 2.3$ (Speagle et al. 2014), while the dashed and dotted lines show locations 3 and 10 times above/below the MS.

combination of cold gas content and metallicity information provides a powerful tool to constrain baryon cycling in the high-redshift universe. Our main conclusions are as follows:

(i) We characterized the dependence of $L'_{\text{CO}(3-2)}$ on M_* , SFR, and O/H at $z \sim 2$, finding that $L'_{\text{CO}(3-2)}/\text{SFR}$ increases with O/H in a tight relation (Figure 5). This result implies that CO luminosity per unit gas mass is lower in low-metallicity galaxies, carrying important implications for the conversion factor between CO luminosity and molecular gas mass.

(ii) We estimated the CO-to-H₂ conversion factor α_{CO} for a sample of $z = 1.1$ –3.2 galaxies with spectroscopic metallicity constraints using two techniques based on dynamical masses and the molecular KS law. With both methods, we found a significant dependence of α_{CO} on O/H such that α_{CO} increases with decreasing O/H (Figure 6), a trend that is physically driven by less dust shielding and more intense UV radiation fields in low-metallicity systems. The $z \sim 2$ relation is consistent with $z \sim 0$ $\alpha_{\text{CO}}(\text{O/H})$ relations within the uncertainties.

(iii) We found that M_{mol} increases and μ_{mol} decreases with increasing M_* , while both properties display a strong secondary positive correlation with SFR at fixed M_* (Figure 7). The scaling relation of Tacconi et al. (2018, 2020) reproduces the observed M_* dependence better than other published μ_{mol} scaling relations (Scoville et al. 2017; Liu et al. 2019), suggesting it provides a more reliable extrapolation if applied to lower-mass $z \sim 2$ samples. The molecular depletion timescales are 700 Myr on average and do not display any dependence on M_* across $\log(M_*/M_\odot) = 10.2$ –11.4.

(iv) A tight near-linear molecular KS law exists at $z \sim 2$ (Figure 8, Equation (14)), providing a reliable means of

estimating M_{mol} indirectly from SFR and size measurements for large high-redshift star-forming samples.

(v) In the $z \sim 2$ MOSDEF-ALMA sample, we found that residuals around the SFR– M_* (star-forming main sequence), O/H– M_* (mass–metallicity relation), and $M_{\text{mol}}-M_*$ relations are correlated (Figures 9 and 10). These correlations are such that, at fixed M_* , galaxies with larger M_{mol} have higher SFR and lower O/H. This result confirms the simultaneous existence of an SFR–FMR and Gas–FMR at $z \sim 2$, both of which have been observed at $z \sim 0$. These results suggest that the scatter of both the star-forming main sequence and mass–metallicity relation are driven by stochastic variations in gas inflow rates that are traced by variations in gas fraction at fixed M_* . Better gas mass constraints spanning a wider range of M_* and SFR are required to obtain the quantitative form of the high-redshift Gas–FMR and its evolution across cosmic history, which could provide high-order tests of gas accretion and feedback models in numerical simulations.

(vi) We used gas-regulator models to infer the outflow mass-loading factors of the $z \sim 2$ sample, finding $\eta_{\text{out}} = 1$ –4 with a typical value of 2.5 with no significant dependence on M_* above $10^{10.2} M_\odot$ (Figure 11). A similar flattening of η_{out} at high M_* is observed at $z \sim 0$. We conclude that the high-mass flattening of the MZR is driven by a flattening in η_{out} , which in turn may be caused by the onset of cyclical AGN feedback in high-mass galaxies.

(vii) We performed a metal budgeting analysis, estimating the mass of metals found inside massive $z \sim 2$ main-sequence galaxies in the gas-phase ISM, dust, and stars (Figure 13). Comparing the sum of these phases to the total metal mass produced over a galaxy lifetime showed that massive $z \sim 2$ star-forming galaxies retain only 30% of produced metals, implying that two-thirds of produced metals are ejected into the CGM and/or IGM and demonstrating the important role of feedback-driven outflows in removing metals from galaxies. Future constraints on CGM metal masses at $z \sim 2$ will be able to determine whether the missing metals can be accounted for.

(viii) We find that the M_{mol} , μ_{gas} , and t_{depl} scaling relations of Tacconi et al. (2018) provide the best overall match to the $z \sim 2$ CO samples in terms of M_* and SFR dependence, suggesting that these relations can be extrapolated to lower masses without incurring large systematic biases. The μ_{gas} scaling relations of Scoville et al. (2016) and Liu et al. (2019) are too steep with M_* such that they likely overestimate the molecular gas content of low-mass systems at $z \sim 2$.

(ix) We explored the possibility of detecting CO(3–2) in low-mass $z \sim 2$ galaxies with ALMA (Figure 14). Main-sequence galaxies at $M_* = 10^{10} M_\odot$ can be detected in 5 hr on source, while starbursts a factor of 5 times above the main-sequence can be reached with the same depth down to $10^{9.5} M_\odot$. Detecting CO at lower masses is inefficient with ALMA, due to the combined effect of decreasing M_{mol} with decreasing M_* and large α_{CO} at low metallicity. Targeting lensed galaxies for CO and deriving M_{mol} from dust continuum observations present promising possibilities to reach low masses at high redshift.

These results demonstrate the power of combining measurements of metallicity and gas mass to constrain baryon cycling for high-redshift galaxies. Existing samples at $z > 2$ with these measurements are small and largely have low-S/N gas measurements (CO or dust continuum) that often require stacking to produce significant detections. Combining samples

from the literature potentially introduces systematic effects due to the variety of selection criteria and rest-optical line ratios available for metallicity determinations. The quest for a detailed understanding of baryon cycling at high redshifts would greatly benefit from a deeper survey of CO emission in a large and systematically selected sample of galaxies with accompanying rest-optical spectroscopy. ALMA currently has the capability to obtain the required measurements for a large sample at $z \sim 2$.

This paper makes use of the following ALMA data: ADS/JAO.ALMA#2018.1.01128.S. ALMA is a partnership of ESO (representing its member states), NSF (USA), and NINS (Japan), together with NRC (Canada), MOST and ASIAA (Taiwan), and KASI (Republic of Korea), in cooperation with the Republic of Chile. The Joint ALMA Observatory is operated by ESO, AUI/NRAO and NAOJ. The National Radio Astronomy Observatory is a facility of the National Science Foundation operated under cooperative agreement by Associated Universities, Inc. Support for this work was provided by NASA through the NASA Hubble Fellowship grant #HST-HF2-51469.001-A awarded by the Space Telescope Science Institute, which is operated by the Association of Universities for Research in Astronomy, Incorporated, under NASA contract NAS5-26555. We acknowledge support from NSF AAG grants AST-1312780, 1312547, 1312764, and 1313171, archival grant AR-13907 provided by NASA through the Space Telescope Science Institute, and grant NNX16AF54G from the NASA ADAP program. We also acknowledge a NASA contract supporting the “WFIRST Extragalactic Potential Observations (EXPO) Science Investigation Team” (15-WFIRST15-0004), administered by GSFC. We additionally acknowledge the 3D-HST collaboration for providing spectroscopic and photometric catalogs used in the MOSDEF survey. The authors wish to recognize and acknowledge the very significant cultural role and reverence that the summit of Maunakea has always had within the indigenous Hawaiian community. We are most fortunate to have the opportunity to conduct observations from this mountain.

Appendix A

Metallicity Calibrations

The set of calibrations used to convert strong-line ratios to metallicities deserves careful consideration in analyses where metallicity plays a key role, especially when a uniform set of emission lines is not available for the entire sample. We adopt calibrations derived from the local sample of $z \sim 2$ analogs from Bian et al. (2018) that Sanders et al. (2020b) found to be a good match to actual $z \sim 2$ galaxies with direct-method abundances for line ratios of [O III], [O II], [Ne III], and H β . Here, we describe some important differences in our use of the Bian et al. (2018) calibration set relative to what is reported in that work. Table A1 provides the metallicity calibrations adopted in this work as polynomial coefficients for use in the following equation:

$$\log(R) = \sum_{n=0}^N c_n x^n, \quad (\text{A1})$$

where R is the line ratio under consideration, $x = 12 + \log(\text{O}/\text{H})$, and c_n are the coefficients. Differences from the values in Bian et al. (2018) are described below.

As noted in Sanders et al. (2021), the [O III] $\lambda 5007/\text{H}\beta$ calibration coefficients given in Equation (17) of Bian et al. (2018) are actually the coefficients fit to [O III] $\lambda\lambda 4959, 5007/\text{H}\beta$, i.e., the ratio including both of the [O III] components. This issue has been confirmed by the authors (F. Bian, private communication). The normalization of the [O III] $\lambda 5007/\text{H}\beta$ calibration in Table A1 is 0.126 dex lower than the value reported in Bian et al. (2018) to correct for this issue, under the assumption that [O III] $\lambda 5007/\lambda 4959 = 2.98$ (Storey & Zeippen 2000).

While strong-line ratios involving the [N II] $\lambda 6584$ line are commonly used to derive the oxygen abundance (e.g., N2 and O3N2; Pettini & Pagel 2004; Marino et al. 2013), N-based calibrations are sensitive to N/H such that differences in N/O at fixed O/H between the calibrating and target samples will systematically bias the O/H estimates. Unfortunately, Sanders et al. (2020b) were unable to test the N2 and O3N2 analog calibrations from Bian et al. (2018), due to the small number of galaxies at $z > 1$ with both direct-method metallicities and [N II] detections.

Figure A1 presents O/H derived from the original Bian et al. (2018) analog calibrations for the $z \sim 2.3$ MOSDEF star-forming galaxy sample of Sanders et al. (2021), comparing metallicities based on O3N2 and N2 to those derived from the combination of [O III], [O II], H β , and [Ne III] (O3O2Ne3). Gray squares show results for composite spectra in bins of M_* . Both the N2 and O3N2 metallicities (tied to the Bian et al. 2018 scale) are lower on average than those based on O3O2Ne3 by 0.12 and 0.06 dex, respectively. These offsets are nearly constant across the full range of O/H. To place metallicities derived from N2 and O3N2 on the same scale as those based on O3O2Ne3 (our preferred method; see Section 2.5), we shift the normalization of the Bian et al. (2018) analog N2 and O3N2 calibrations based on the average offsets reported above, obtaining:

$$12 + \log(\text{O}/\text{H}) = 8.94 + 0.49 \times \text{N2} \quad (\text{A2})$$

$$12 + \log(\text{O}/\text{H}) = 9.03 - 0.39 \times \text{O3N2}. \quad (\text{A3})$$

For reference, the leading constant factors of the original Bian et al. (2018) calibrations are 8.82 and 8.97, respectively. The coefficients in Table A1 match these renormalized relations and yield consistent metallicities on average from N2, O3N2, or O3O2Ne3 for $z \sim 2.3$ galaxies.

The individual galaxies are color-coded by the difference in [N II] $\lambda 6584/[\text{O II}]$ relative to the average value at fixed M_* ($\Delta \log([\text{N II}]/[\text{O II}])$), where the average relation is $\log([\text{N II}]/[\text{O II}]) = 0.37 \times \log(M_*/10^{10} \text{ M}_\odot) - 0.99$ as fit to the composite spectra of Sanders et al. (2021). For both N2 and O3N2, there is a clear trend that the offset relative to the O3O2Ne3 metallicities is correlated with deviations in [N II]/[O II]. Furthermore, only galaxies with [N II]/[O II] ~ 0.3 dex higher than average at fixed M_* lie on the one-to-one line, i.e., have consistent metallicities from O3O2Ne3 and N2 or O3N2 using the original Bian et al. (2018) analog calibrations.

Metallicities based on N2 and O3N2 are clearly sensitive to variations in N/O (as traced by [N II]/[O II]) at fixed O/H, with N2 more strongly affected than O3N2. The average offsets observed in Figure A1 can be explained if the Bian et al. (2018) analog calibrating sample has higher N/O at fixed O/H than the $z \sim 2.3$ sample. Figure A2 presents [N II]/[O II] versus [O III]/H β for the $z \sim 2.3$ MOSDEF and Bian et al. (2018) analog samples. The Bian et al. (2018) stacks have ~ 0.3 dex

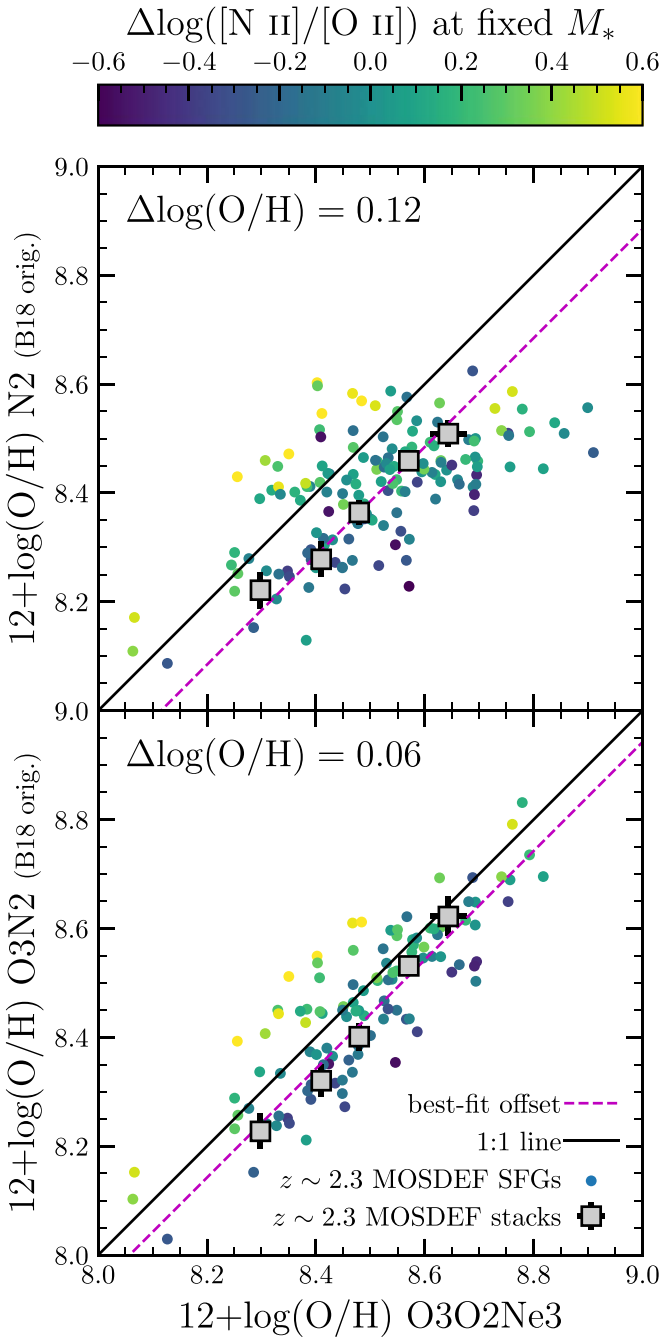


Figure A1. Gas-phase oxygen abundance derived from N2 (top) and O3N2 (bottom) using the original Bian et al. (2018) calibrations vs. O/H based on the combination of [O III], [O II], [Ne III], and H β (O3O2Ne3). Gray squares show composite spectra of $z \sim 2.3$ star-forming galaxies from Sanders et al. (2021). Small circles display individual $z \sim 2.3$ galaxies, color-coded by the difference in [N II]/[O II] relative to the average value at fixed M_* . The solid black line denotes a one-to-one relation. The dashed pink line presents the best-fit offset between each pair of metallicities, as fit to the composite spectra. The N2 and O3N2 calibrations given in Table A1 have been renormalized such that N2, O3N2, and O3O2Ne3 yield consistent metallicities on average for the $z \sim 2.3$ sample.

larger [N II]/[O II] than the $z \sim 2.3$ sample at fixed [O III]/H β . Based on the calibration of Strom et al. (2017), a difference of 0.3 dex in [N II]/[O II] corresponds to a difference of 0.2 dex in N/O. This exercise suggests that the Bian et al. (2018) analog sample has larger N/O at fixed O/H than actual $z \sim 2.3$ star-forming galaxies and highlights the care that is needed when

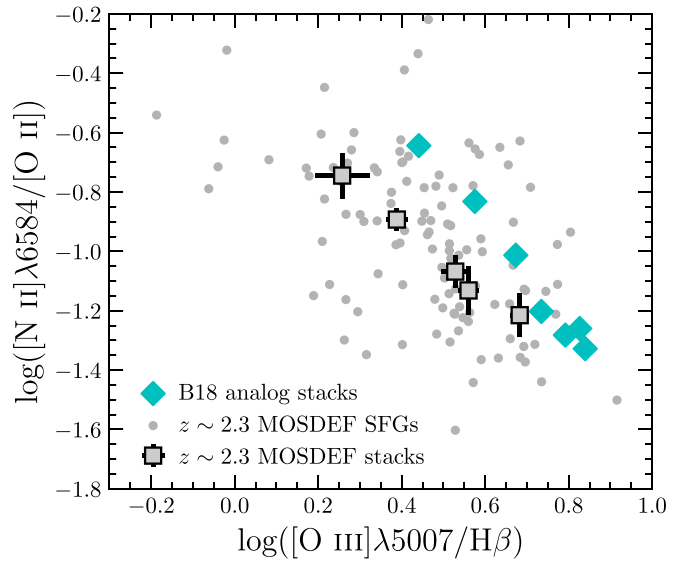


Figure A2. Line ratio diagram of [N II]/[O II] vs. [O III]/H β for $z \sim 2.3$ star-forming galaxies (gray circles), composite spectra of $z \sim 2.3$ galaxies in bins of M_* (gray squares; Sanders et al. 2021), and composite spectra of local analogs of high-redshift galaxies (cyan diamonds; Bian et al. 2018).

Table A1
Adopted Metallicity Calibrations for High-redshift Samples, with Coefficients Given for Equation (A1)

Line Ratio (R)	c_0	c_1	c_2	c_3
[O III]λ5007/H β	43.8576	-21.6211	3.4277	-0.1747
[O III]λ5007/[O II]	14.35	-1.70
[Ne III]λ3869/[O II]	12.38	-1.59
R_{23}^a	138.0430	-54.8284	7.2954	-0.32293
[N II]λ6584/H α	-18.24	2.04
O3N2 ^b	23.12	-2.56

Notes.

^a $R_{23} = ([O\ III]\lambda\lambda 4959, 5007 + [O\ II]\lambda\lambda 3726, 3729)/H\beta$.

^b $O3N2 = ([O\ III]\lambda 5007/H\beta)/([N\ II]\lambda 6584/H\alpha)$.

using local analogs in place of actual high-redshift samples. These analogs were selected to lie in the same region of the [N II] BPT diagram as $z \sim 2$ samples. This criterion has clearly failed to select galaxies with identical ISM conditions to those at $z \sim 2$, consistent with recent work that found local and high-redshift galaxies occupying the same region of the BPT diagram maintain some distinct differences in their ISM conditions (Runco et al. 2020). Improving metallicity calibrations for use at high redshifts will require more careful selection of local analogs, and ultimately, an expanded sample of high-redshift sources with direct-method metallicities that will soon be enabled by the James Webb Space Telescope.

Appendix B

Parameterization of the Evolving Mass–Metallicity Relation

We utilize recent observational determinations of the mass–metallicity relation at different redshifts to obtain a functional form for the evolving mass–metallicity relation parameterized by M_* and z . We use the high-redshift measurements of Sanders et al. (2021) based on composite spectra of $z \sim 2.3$ and $z \sim 3.3$ star-forming galaxies from the MOSDEF survey. Metallicities of the high-redshift samples are based on

O3O2Ne3 and derived using the Bian et al. (2018) $z \sim 2$ analog calibrations. We add the binned data of Curti et al. (2020) for a sample of $\sim 150,000$ star-forming galaxies at $z_{\text{med}} = 0.08$ from the Sloan Digital Sky Survey (SDSS) to set the local baseline. Metallicities of the local sample were determined using calibrations based on stacked spectra of normal $z \sim 0$ galaxies derived in Curti et al. (2020). Both calibration sets are on a T_e -based metallicity scale.

We fit the $z \sim 0$, $z \sim 2.3$, and $z \sim 3.3$ data with a function of the form

$$\text{MZR}(M_*, z) = Z_0 - \gamma/\beta \times \log(1 + [M_*/M_0(z)]^{-\beta}), \quad (\text{B1})$$

where Z_0 is the high-mass asymptotic metallicity, γ is the low-mass power-law slope, and β controls the sharpness of the turnover that occurs at the mass $\log(M_0(z)/M_\odot) = m_0 + m_1^* \log(1 + z)$. This is the same functional form used to fit the $z \sim 0$ SFR-FMR by Curti et al. (2020), but with the secondary parameter being $(1 + z)$ instead of SFR. We find the following best-fit parameters: $Z_0 = 8.80$, $\gamma = 0.30$, $\beta = 1.08$, $m_0 = 9.90$, and $m_1 = 2.06$. This fitting function yields a nearly identical relation to the Curti et al. (2020) best-fit $z \sim 0$ MZR when evaluated at $z = 0.08$.

Figure B1 shows the best-fit $\text{MZR}(M_*, z)$ alongside the $z \sim 2.3$ and $z \sim 3.3$ data (green and blue, respectively; $z \sim 0$ data are not displayed, for clarity), displaying a good fit across the entire mass range. To test the applicability of this fitting function across a wider range of redshifts, we compare to samples at $z \sim 0.8$ (Zahid et al. 2011, DEEP2) and $z \sim 1.5$ (Topping et al. 2021, MOSDEF). The metallicities of the $z \sim 0.8$ sample have been re-evaluated using the R_{23} and O_{32} $z \sim 0$ calibrations of Curti et al. (2020), while those of the $z \sim 1.5$ sample have been rederived with the renormalized high-redshift N2 calibration given in Table A1. Our best-fit $\text{MZR}(M_*, z)$ function provides a good match at intermediate redshifts as well, demonstrating that it is widely applicable over $z = 0\text{--}3.3$ for galaxies above $10^9 M_\odot$.

The gray dashed lines show the $\text{MZR}(M_*, z)$ derived by Genzel et al. (2015) and adopted by Tacconi et al. (2018, 2020), evaluated at $z = [0.8, 1.5, 2.3, 3.3]$. Our new relation yields higher metallicity at fixed M_* and redshift across the full mass range (0.15 dex in O/H at $10^{10.5} M_\odot$ and $z = 2.3$).

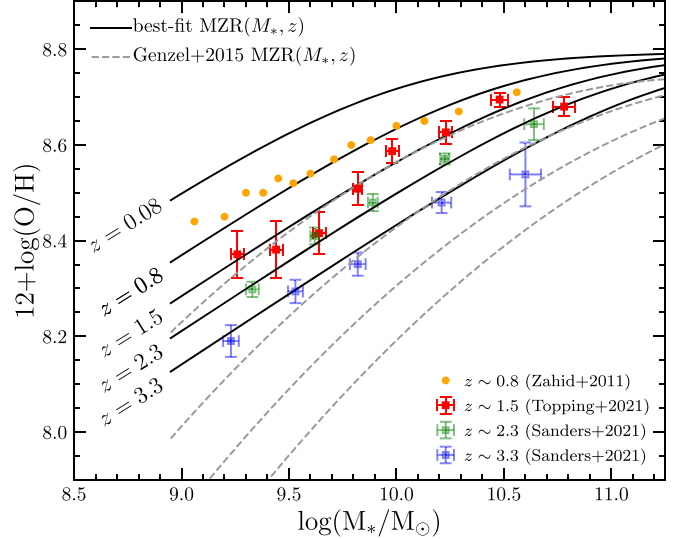


Figure B1. The mass–metallicity relation for samples of star-forming galaxies at a range of redshifts: $z \sim 0.8$ (Zahid et al. 2011), $z \sim 1.5$ (Topping et al. 2021), and $z \sim 2.3$ and 3.3 (Sanders et al. 2021). Solid black lines show the best-fit $\text{MZR}(M_*, z)$ to data at $z = 0.08$ (Curti et al. 2020), $z \sim 2.3$, and $z \sim 3.3$, assuming the functional form given in Equation (B1). Additional black lines display the best-fit $\text{MZR}(M_*, z)$ evaluated at $z = 0.8$ and $z = 1.5$ in comparison to observational MZR data at these redshifts that were not used in the fitting process, demonstrating that the best-fit function is robust across the intermediate redshift range as well. Dashed gray lines display the $\text{MZR}(M_*, z)$ function of Genzel et al. (2015), evaluated at $z = [0.8, 1.5, 2.3, 3.3]$.

The difference primarily stems from the use of larger and more representative high-redshift data sets in this work (see Sanders et al. 2021 for a discussion) and different choices of metallicity calibrations, in particular the use of different calibrations at low and high redshifts in this work to reflect evolving ISM ionization conditions.

Appendix C Literature CO References

Table C1 presents the properties and literature references for the $z = 2\text{--}3$ literature CO sample and the supplementary $z > 1$ α_{CO} sample.

Table C1
Literature CO samples

Literature $z = 2$ –3 CO sample									
ID	z_{spec}	$\log\left(\frac{M_*}{M_\odot}\right)$	$\log\left(\frac{\text{SFR}}{M_\odot \text{ yr}^{-1}}\right)$	12+log(O/H)	Type ^a	$\log\left(\frac{M_{\text{mol}}}{M_\odot}\right)$	$\log(\mu_{\text{mol}})$	CO Reference ^b	O/H Ref. ^b
zC406690	2.1950	10.62 ± 0.10	2.47 ± 0.15	8.48 ± 0.02	N2	11.20 ± 0.10	0.58 ± 0.14	1	2
HDF-BX1439	2.1867	10.55 ± 0.05	2.06 ± 0.26	8.49 ± 0.05	O2O3Ne3	10.81 ± 0.15	0.26 ± 0.16	1	3
Q1623-MD66	2.1075	10.59 ± 0.10	2.39 ± 0.15	8.55 ± 0.02	N2	<11.22	<0.63	1	4
Q1623-BX453	2.1820	10.48 ± 0.10	2.39 ± 0.15	8.71 ± 0.01	O3N2	10.88 ± 0.06	0.40 ± 0.12	1	5
Q1623-BX528	2.2684	10.84 ± 0.10	1.77 ± 0.15	8.69 ± 0.03	N2	<10.60	<-0.24	1	6
Q1623-BX599	2.3312	10.75 ± 0.10	2.12 ± 0.15	8.58 ± 0.02	N2	10.82 ± 0.09	0.07 ± 0.14	1	2
Q1623-BX663	2.4335	10.81 ± 0.10	2.16 ± 0.15	8.63 ± 0.07	N2	<10.97	<0.16	1	6
Q1700-MD69	2.2881	11.21 ± 0.10	2.03 ± 0.15	8.71 ± 0.01	O3N2	10.92 ± 0.07	-0.29 ± 0.12	1	5
Q1700-BX691	2.1891	10.89 ± 0.10	1.73 ± 0.15	8.70 ± 0.03	O3N2	10.55 ± 0.12	-0.34 ± 0.16	1	5
Q2343-BX610	2.2107	11.00 ± 0.10	2.33 ± 0.15	8.72 ± 0.01	N2	11.29 ± 0.02	0.29 ± 0.10	1	2
Q2343-BX513	2.1082	10.43 ± 0.10	1.45 ± 0.15	8.60 ± 0.02	N2	10.61 ± 0.15	0.18 ± 0.18	1	2
Q2343-BX442	2.1752	11.12 ± 0.10	1.91 ± 0.15	8.85 ± 0.03	O3N2	10.73 ± 0.12	-0.39 ± 0.15	1	5
Q2343-BX389	2.1711	10.97 ± 0.10	1.91 ± 0.15	8.56 ± 0.03	O3N2	<11.23	<0.26	1	5
UDF3/3mm.01	2.5430	10.52 ± 0.26	2.30 ± 0.16	8.74 ± 0.05	O3N2	11.43 ± 0.02	0.91 ± 0.26	7	8
UDF4/3mm.03	2.4537	10.36 ± 0.15	1.97 ± 0.03	8.74 ± 0.08	N2	11.00 ± 0.04	0.64 ± 0.16	7	8
UDF11/9mm.5	1.9978	10.91 ± 0.04	2.23 ± 0.27	8.66 ± 0.02	N2	10.80 ± 0.12	-0.11 ± 0.13	9	8
Q1700-MD94	2.3330	11.18 ± 0.10	2.43 ± 0.15	...	MZR	11.37 ± 0.07	0.19 ± 0.07	1	...
Q1700-MD174	2.3400	11.38 ± 0.10	2.20 ± 0.15	...	MZR	11.05 ± 0.05	-0.33 ± 0.05	1	...
Q1700-BX561	2.4340	11.08 ± 0.10	1.23 ± 0.15	...	MZR	10.41 ± 0.15	-0.67 ± 0.15	1	...
Q2343-MD59	2.0110	10.88 ± 0.10	1.41 ± 0.15	...	MZR	10.88 ± 0.08	-0.00 ± 0.08	1	...
3mm.07	2.6961	11.10 ± 0.10	2.27 ± 0.05	...	MZR	11.30 ± 0.05	0.20 ± 0.05	7	...
3mm.09	2.6977	11.10 ± 0.10	2.50 ± 0.05	...	MZR	11.02 ± 0.04	-0.08 ± 0.04	7	...
3mm.12	2.5739	10.60 ± 0.10	1.49 ± 0.15	...	MZR	10.68 ± 0.06	0.08 ± 0.06	7	...
Supplementary $z > 1$ α_{CO} sample									
ID	z_{spec}	12+log(O/H)		Type ^a			CO Ref. ^b	O/H Ref. ^b	
BzK-16000	1.5249	8.72 ± 0.01		N2			10	3	
cB58	2.7293	8.43 ± 0.04		O3N2			11	12	
CosmicEye	3.0740	8.62 ± 0.02		N2			13	14	
Eyelash	2.3230	8.53 ± 0.02		O2O3Ne3			15	16	
8oclock	2.7360	8.53 ± 0.01		O2O3Ne3			17	14	
Horseshoe	2.3813	8.54 ± 0.03		N2			17	18	
Clone	2.0026	8.41 ± 0.02		N2			17	18	
HDF-M23	3.2159	8.51 ± 0.08		O2O3Ne3			19	3	
UDF6/3mm.04	1.4152	8.75 ± 0.06		O3N2			7	8	
3mm.06	1.0955	8.92 ± 0.06		N2			7	7	
3mm.11	1.0964	8.70 ± 0.03		N2			7	7	
3mm.14	1.0981	8.65 ± 0.04		O2O3Ne3			7	7	
MP.3mm.02	1.0872	8.64 ± 0.02		O2O3Ne3			7	7	
S15-830	1.4610	8.72 ± 0.08		O2O3Ne3			20	21	

Notes.

^a Line ratio used for metallicity derivation, described in Section 2.5. Metallicities of sources with “MZR” are inferred from Equation (1) for use in M_{mol} calculations.

^b References for CO and rest-optical spectroscopic observations.

References. (1) Tacconi et al. 2013; (2) Förster Schreiber et al. 2018; (3) Kriek et al. 2015; (4) Shapley et al. 2004; (5) Steidel et al. 2014; (6) Förster Schreiber et al. 2006; (7) Boogaard et al. 2019; (8) Shapley et al. 2020; (9) Riechers et al. 2020; (10) Daddi et al. 2010; (11) Baker et al. 2004; (12) Teplitz et al. 2000; (13) Riechers et al. 2010; (14) Richard et al. 2011; (15) Danielson et al. 2011; (16) Olivares et al. 2016; (17) Saintonge et al. 2013; (18) Hainline et al. 2009; (19) Magdis et al. 2012; (20) Silverman et al. 2015; (21) Kashino et al. 2019.

ORCID iDs

Ryan L. Sanders  <https://orcid.org/0000-0003-4792-9119>
Alice E. Shapley  <https://orcid.org/0000-0003-3509-4855>
Tucker Jones  <https://orcid.org/0000-0001-5860-3419>
Irene Shivaei  <https://orcid.org/0000-0003-4702-7561>
Gergö Popping  <https://orcid.org/0000-0003-1151-4659>
Naveen A. Reddy  <https://orcid.org/0000-0001-9687-4973>
Romeel Davé  <https://orcid.org/0000-0003-2842-9434>
Sedona H. Price  <https://orcid.org/0000-0002-0108-4176>

Mariska Kriek  <https://orcid.org/0000-0002-7613-9872>
Alison L. Coil  <https://orcid.org/0000-0002-2583-5894>
Brian Siana  <https://orcid.org/0000-0002-4935-9511>

References

Accurso, G., Saintonge, A., Catinella, B., et al. 2017, *MNRAS*, 470, 4750
Adelberger, K. L., Shapley, A. E., Steidel, C. C., et al. 2005, *ApJ*, 629, 636
Aird, J., Coil, A. L., & Georgakakis, A. 2019, *MNRAS*, 484, 4360
Andrews, B. H., & Martini, P. 2013, *ApJ*, 765, 140

Anglés-Alcázar, D., Faucher-Giguère, C.-A., Kereš, D., et al. 2017, *MNRAS*, **470**, 4698

Aravena, M., Boogaard, L., Gómez-López, J., et al. 2020, *ApJ*, **901**, 79

Arimoto, N., Sofue, Y., & Tsujimoto, T. 1996, *PASJ*, **48**, 275

Asplund, M., Amarsi, A. M., & Grevesse, N. 2021, *A&A*, **653**, A141

Azadi, M., Coil, A., Aird, J., et al. 2018, *ApJ*, **866**, 63

Azadi, M., Coil, A. L., Aird, J., et al. 2017, *ApJ*, **835**, 27

Baker, A. J., Tacconi, L. J., Genzel, R., Lehnert, M. D., & Lutz, D. 2004, *ApJ*, **604**, 125

Bian, F., Kewley, L. J., & Dopita, M. A. 2018, *ApJ*, **859**, 175

Bigiel, F., Leroy, A., Walter, F., et al. 2008, *AJ*, **136**, 2846

Bolatto, A. D., Wolfire, M., & Leroy, A. K. 2013, *ARA&A*, **51**, 207

Boogaard, L. A., Decarli, R., González-López, J., et al. 2019, *ApJ*, **882**, 140

Boogaard, L. A., van der Werf, P., Weiss, A., et al. 2020, *ApJ*, **902**, 109

Bothwell, M. S., Maiolino, R., Cicone, C., Peng, Y., & Wagg, J. 2016a, *A&A*, **595**, A48

Bothwell, M. S., Maiolino, R., Kennicutt, R., et al. 2013, *MNRAS*, **433**, 1425

Bothwell, M. S., Maiolino, R., Peng, Y., et al. 2016b, *MNRAS*, **455**, 1156

Bothwell, M. S., Wagg, J., Cicone, C., et al. 2014, *MNRAS*, **445**, 2599

Brammer, G. B., van Dokkum, P. G., Franx, M., et al. 2012, *ApJS*, **200**, 13

Brinchmann, J., Charlot, S., White, S. D. M., et al. 2004, *MNRAS*, **351**, 1151

Brown, T., Cortese, L., Catinella, B., & Kilborn, V. 2018, *MNRAS*, **473**, 1868

Calzetti, D., Armus, L., Bohlin, R. C., et al. 2000, *ApJ*, **533**, 682

Cappellari, M., Bacon, R., Bureau, M., et al. 2006, *MNRAS*, **366**, 1126

Cardelli, J. A., Clayton, G. C., & Mathis, J. S. 1989, *ApJ*, **345**, 245

Chabrier, G. 2003, *PASP*, **115**, 763

Coil, A. L., Aird, J., Reddy, N., et al. 2015, *ApJ*, **801**, 35

Conroy, C., Gunn, J. E., & White, M. 2009, *ApJ*, **699**, 486

Coppin, K. E. K., Swinbank, A. M., Neri, R., et al. 2007, *ApJ*, **665**, 936

Cresci, G., Mannucci, F., & Curti, M. 2019, *A&A*, **627**, A42

Cullen, F., Cirasuolo, M., McLure, R. J., Dunlop, J. S., & Bowler, R. A. A. 2014, *MNRAS*, **440**, 2300

Cullen, F., Shapley, A. E., McLure, R. J., et al. 2021, *MNRAS*, **505**, 903

Curti, M., Cresci, G., Mannucci, F., et al. 2017, *MNRAS*, **465**, 1384

Curti, M., Mannucci, F., Cresci, G., & Maiolino, R. 2020, *MNRAS*, **491**, 944

Daddi, E., Bournaud, F., Walter, F., et al. 2010, *ApJ*, **713**, 686

Daddi, E., Dannerbauer, H., Liu, D., et al. 2015, *A&A*, **577**, A46

Danielson, A. L. R., Swinbank, A. M., Smail, I., et al. 2011, *MNRAS*, **410**, 1687

Davé, R., Anglés-Alcázar, D., Narayanan, D., et al. 2019, *MNRAS*, **486**, 2827

Davé, R., Crain, R. A., Stevens, A. R. H., et al. 2020, *MNRAS*, **497**, 146

Davé, R., Finlator, K., & Oppenheimer, B. D. 2012, *MNRAS*, **421**, 98

Davé, R., Raftieferantsoa, M. H., Thompson, R. J., & Hopkins, P. F. 2017, *MNRAS*, **467**, 115

Dayal, P., Ferrara, A., & Dunlop, J. S. 2013, *MNRAS*, **430**, 2891

de los Reyes, M. A. C., & Kennicutt, R. C. J. 2019, *ApJ*, **872**, 16

De Rossi, M. E., Bower, R. G., Font, A. S., Schaye, J., & Theuns, T. 2017, *MNRAS*, **472**, 3354

De Rossi, M. E., Theuns, T., Font, A. S., & McCarthy, I. G. 2015, *MNRAS*, **452**, 486

De Vis, P., Jones, A., Viaene, S., et al. 2019, *A&A*, **623**, A5

Decarli, R., Walter, F., Gómez-López, J., et al. 2019, *ApJ*, **882**, 138

Dessauges-Zavadsky, M., Richard, J., Combes, F., et al. 2019, *NatAs*, **3**, 1115

Dessauges-Zavadsky, M., Zamojski, M., Rujopakarn, W., et al. 2017, *A&A*, **605**, A81

Dessauges-Zavadsky, M., Zamojski, M., Schaefer, D., et al. 2015, *A&A*, **577**, A50

Di Matteo, P., Combes, F., Melchior, A. L., & Semelin, B. 2007, *A&A*, **468**, 61

Erb, D. K., Shapley, A. E., Pettini, M., et al. 2006a, *ApJ*, **644**, 813

Erb, D. K., Steidel, C. C., Shapley, A. E., et al. 2006b, *ApJ*, **646**, 107

Fensch, J., Renaud, F., Bournaud, F., et al. 2017, *MNRAS*, **465**, 1934

Finlator, K., & Davé, R. 2008, *MNRAS*, **385**, 2181

Ford, A. B., Davé, R., Oppenheimer, B. D., et al. 2014, *MNRAS*, **444**, 1260

Förster Schreiber, N. M., Genzel, R., Lehnert, M. D., et al. 2006, *ApJ*, **645**, 1062

Förster Schreiber, N. M., Renzini, A., Mancini, C., et al. 2018, *ApJS*, **238**, 21

Förster Schreiber, N. M., Übler, H., Davies, R. L., et al. 2019, *ApJ*, **875**, 21

Genzel, R., Förster Schreiber, N. M., Übler, H., et al. 2017, *Natur*, **543**, 397

Genzel, R., Price, S. H., Übler, H., et al. 2020, *ApJ*, **902**, 98

Genzel, R., Tacconi, L. J., Combes, F., et al. 2012, *ApJ*, **746**, 69

Genzel, R., Tacconi, L. J., Lutz, D., et al. 2015, *ApJ*, **800**, 20

Glover, S. C. O., & Mac Low, M. M. 2011, *MNRAS*, **412**, 337

González-López, J., Bauer, F. E., Aravena, M., et al. 2017, *A&A*, **608**, A138

González-López, J., Decarli, R., Pavesi, R., et al. 2019, *ApJ*, **882**, 139

Greve, T. R., Bertoldi, F., Smail, I., et al. 2005, *MNRAS*, **359**, 1165

Grogan, N. A., Kocevski, D. D., Faber, S. M., et al. 2011, *ApJS*, **197**, 35

Hainline, K. N., Shapley, A. E., Kornei, K. A., et al. 2009, *ApJ*, **701**, 52

Hao, C.-N., Kennicutt, R. C., Johnson, B. D., et al. 2011, *ApJ*, **741**, 124

Hayward, C. C., & Hopkins, P. F. 2017, *MNRAS*, **465**, 1682

Heckman, T. M., & Best, P. N. 2014, *ARA&A*, **52**, 589

Henry, A., Rafelski, M., Sunquist, B., et al. 2021, *ApJ*, **919**, 143

Hickox, R. C., Mullaney, J. R., Alexander, D. M., et al. 2014, *ApJ*, **782**, 9

Horne, K. 1986, *PASP*, **98**, 609

Hughes, T. M., Cortese, L., Boselli, A., Gavazzi, G., & Davies, J. I. 2013, *A&A*, **550**, A115

Kaasinen, M., Scoville, N., Walter, F., et al. 2019, *ApJ*, **880**, 15

Kashino, D., Silverman, J. D., Sanders, D., et al. 2019, *ApJS*, **241**, 10

Kauffmann, G., White, S. D. M., Heckman, T. M., et al. 2004, *MNRAS*, **353**, 713

Kennicutt, R. C. J., & De Los Reyes, M. A. C. 2021, *ApJ*, **908**, 61

Kennicutt, R. C., Jr. 1998, *ARA&A*, **36**, 189

Kim, C.-G., Ostriker, E. C., Somerville, R. S., et al. 2020, *ApJ*, **900**, 61

Koekemoer, A. M., Faber, S. M., Ferguson, H. C., et al. 2011, *ApJS*, **197**, 36

Kriek, M., Shapley, A. E., Reddy, N. A., et al. 2015, *ApJS*, **218**, 15

Kriek, M., van Dokkum, P. G., Labb  , I., et al. 2009, *ApJ*, **700**, 221

Lagos, C. D. P., Baugh, C. M., Lacey, C. G., et al. 2011, *MNRAS*, **418**, 1649

Lara-L  pez, M. A., Cepa, J., Bongiovanni, A., et al. 2010, *A&A*, **521**, L53

Lara-L  pez, M. A., Hopkins, A. M., L  pez-Sanchez, A. R., et al. 2013, *MNRAS*, **433**, L35

Leroy, A. K., Walter, F., Brinks, E., et al. 2008, *AJ*, **136**, 2782

Leung, G. C. K., Coil, A. L., Aird, J., et al. 2019, *ApJ*, **886**, 11

Lilly, S. J., Carollo, C. M., Pipino, A., Renzini, A., & Peng, Y. 2013, *ApJ*, **772**, 119

Liu, D., Schinnerer, E., Groves, B., et al. 2019, *ApJ*, **887**, 235

Ma, X., Hopkins, P. F., Faucher-Gigu  re, C.-A., et al. 2016, *MNRAS*, **456**, 2140

Madau, P., & Dickinson, M. 2014, *ARA&A*, **52**, 415

Magdis, G. E., Daddi, E., B  thermin, M., et al. 2012, *ApJ*, **760**, 6

Magnelli, B., Saintonge, A., Lutz, D., et al. 2012, *A&A*, **548**, A22

Maiolino, R., Nagao, T., Grazian, A., et al. 2008, *A&A*, **488**, 463

Mannucci, F., Cresci, G., Maiolino, R., Marconi, A., & Gnerucci, A. 2010, *MNRAS*, **408**, 2115

Marino, R. A., Rosales-Ortega, F. F., S  nchez, S. F., et al. 2013, *A&A*, **559**, A114

McLean, I. S., Steidel, C. C., Epps, H. W., et al. 2012, *Proc. SPIE*, **8446**, 84460J

McMullin, J. P., Waters, B., Schiebel, D., Young, W., & Golap, K. 2007, in *ASP Conf. Ser.* 376, *Astronomical Data Analysis Software and Systems XVI*, ed. R. A. Shaw, F. Hill, & D. J. Bell (San Francisco, CA: ASP), **127**

Mitchell, P. D., Schaye, J., Bower, R. G., & Crain, R. A. 2020, *MNRAS*, **494**, 3971

Momcheva, I. G., Brammer, G. B., van Dokkum, P. G., et al. 2016, *ApJS*, **225**, 27

Muratov, A. L., Kere  , D., Faucher-Gigu  re, C.-A., et al. 2015, *MNRAS*, **454**, 2691

Muratov, A. L., Kere  , D., Faucher-Gigu  re, C.-A., et al. 2017, *MNRAS*, **468**, 4170

Nelson, D., Pillepich, A., Springel, V., et al. 2019, *MNRAS*, **490**, 3234

Noeske, K. G., Weiner, B. J., Faber, S. M., et al. 2007, *ApJL*, **660**, L43

Nomoto, K., Kobayashi, C., & Tominaga, N. 2013, *ARA&A*, **51**, 457

Oke, J. B., & Gunn, J. E. 1983, *ApJ*, **266**, 713

Olivares, V., Treister, E., Privon, G. C., et al. 2016, *ApJ*, **827**, 57

Oppenheimer, B. D., Crain, R. A., Schaye, J., et al. 2016, *MNRAS*, **460**, 2157

Osterbrock, D. E., & Ferland, G. J. 2006, *Astrophysics of Gaseous Nebulae and Active Galactic Nuclei* (Sausalito, CA: University Science Books)

Pandya, V., Somerville, R. S., Angl  s-Alc  zar, D., et al. 2020, *ApJ*, **905**, 4

Pavesi, R., Sharon, C. E., Riechers, D. A., et al. 2018, *ApJ*, **864**, 49

Peeples, M. S., & Shankar, F. 2011, *MNRAS*, **417**, 2962

Peeples, M. S., Werk, J. K., Tumlinson, J., et al. 2014, *ApJ*, **786**, 54

Peng, Y.-j., & Maiolino, R. 2014, *MNRAS*, **443**, 3643

Pettini, M., & Pagel, B. E. J. 2004, *MNRAS*, **348**, L59

Pettini, M., Shapley, A. E., Steidel, C. C., et al. 2001, *ApJ*, **554**, 981

Pilyugin, L. S., & Thuan, T. X. 2011, *ApJL*, **726**, L23

Popping, G., Behroozi, P. S., & Peeples, M. S. 2015, *MNRAS*, **449**, 477

Popping, G., Shivaei, I., Sanders, R. L., et al. 2022, arXiv:2204.08483

Popping, G., Somerville, R. S., & Trager, S. C. 2014, *MNRAS*, **442**, 2398

Price, S. H., Kriek, M., Barro, G., et al. 2020, *ApJ*, **894**, 91

Price, S. H., Kriek, M., Shapley, A. E., et al. 2016, *ApJ*, **819**, 80

Price, S. H., Shimizu, T. T., Genzel, R., et al. 2021, *ApJ*, **922**, 143

Reddy, N. A., Erb, D. K., Pettini, M., Steidel, C. C., & Shapley, A. E. 2010, *ApJ*, **712**, 1070

Reddy, N. A., Pettini, M., Steidel, C. C., et al. 2012, *ApJ*, **754**, 25

Reddy, N. A., Shapley, A. E., Kriek, M., et al. 2020, *ApJ*, **902**, 123

Reddy, N. A., Shapley, A. E., Sanders, R. L., et al. 2018, *ApJ*, **869**, 92

Richard, J., Jones, T., Ellis, R., et al. 2011, *MNRAS*, **413**, 643

Riechers, D. A., Boogaard, L. A., Decarli, R., et al. 2020, *ApJL*, **896**, L21

Riechers, D. A., Carilli, C. L., Walter, F., & Momjian, E. 2010, *ApJL*, **724**, L153

Rudie, G. C., Steidel, C. C., Pettini, M., et al. 2019, *ApJ*, **885**, 61

Runco, J. N., Shapley, A. E., Sanders, R. L., et al. 2021, *MNRAS*, **502**, 2600

Saintonge, A., & Catinella, B. 2022, *ARA&A*, **60**, 319

Saintonge, A., Catinella, B., Cortese, L., et al. 2016, *MNRAS*, **462**, 1749

Saintonge, A., Catinella, B., Tacconi, L. J., et al. 2017, *ApJS*, **233**, 22

Saintonge, A., Lutz, D., Genzel, R., et al. 2013, *ApJ*, **778**, 2

Salpeter, E. 1955, *ApJ*, **121**, 161

Sanders, R. L., Jones, T., Shapley, A. E., et al. 2020a, *ApJL*, **888**, L11

Sanders, R. L., Shapley, A. E., Jones, T., et al. 2021, *ApJ*, **914**, 19

Sanders, R. L., Shapley, A. E., Kriek, M., et al. 2015, *ApJ*, **799**, 138

Sanders, R. L., Shapley, A. E., Kriek, M., et al. 2016, *ApJ*, **816**, 23

Sanders, R. L., Shapley, A. E., Kriek, M., et al. 2018, *ApJ*, **858**, 99

Sanders, R. L., Shapley, A. E., Reddy, N. A., et al. 2020b, *MNRAS*, **491**, 1427

Sandstrom, K. M., Leroy, A. K., Walter, F., et al. 2013, *ApJ*, **777**, 5

Sargent, M. T., Daddi, E., Béthermin, M., et al. 2014, *ApJ*, **793**, 19

Schruba, A., Leroy, A. K., Walter, F., et al. 2012, *AJ*, **143**, 138

Scoville, N., Lee, N., Vanden Bout, P., et al. 2017, *ApJ*, **837**, 150

Scoville, N., Sheth, K., Aussel, H., et al. 2016, *ApJ*, **820**, 83

Seko, A., Ohta, K., Yabe, K., et al. 2016, *ApJ*, **819**, 82

Shapley, A. E., Cullen, F., Dunlop, J. S., et al. 2020, *ApJL*, **903**, L16

Shapley, A. E., Erb, D. K., Pettini, M., Steidel, C. C., & Adelberger, K. L. 2004, *ApJ*, **612**, 108

Shapley, A. E., Reddy, N. A., Kriek, M., et al. 2015, *ApJ*, **801**, 88

Shapley, A. E., Sanders, R. L., Salim, S., et al. 2022, *ApJ*, **926**, 145

Shapley, A. E., Sanders, R. L., Shao, P., et al. 2019, *ApJL*, **881**, L35

Shivaei, I., Popping, G., Rieke, G., et al. 2022, *ApJ*, **928**, 68

Silverman, J. D., Daddi, E., Rodighiero, G., et al. 2015, *ApJL*, **812**, L23

Silverman, J. D., Rujopakarn, W., Daddi, E., et al. 2018, *ApJ*, **867**, 92

Skelton, R. E., Whitaker, K. E., Momcheva, I. G., et al. 2014, *ApJS*, **214**, 24

Solimano, M., González-López, J., Barrientos, L. F., et al. 2021, *A&A*, **655**, A42

Solomon, P. M., Downes, D., Radford, S. J. E., & Barrett, J. W. 1997, *ApJ*, **478**, 144

Speagle, J. S., Steinhardt, C. L., Capak, P. L., & Silverman, J. D. 2014, *ApJS*, **214**, 15

Steidel, C. C., Erb, D. K., Shapley, A. E., et al. 2010, *ApJ*, **717**, 289

Steidel, C. C., Rudie, G. C., Strom, A. L., et al. 2014, *ApJ*, **795**, 165

Steidel, C. C., Strom, A. L., Pettini, M., et al. 2016, *ApJ*, **826**, 159

Storey, P. J., & Zeippen, C. J. 2000, *MNRAS*, **312**, 813

Strom, A. L., Steidel, C. C., Rudie, G. C., et al. 2017, *ApJ*, **836**, 164

Strom, A. L., Steidel, C. C., Rudie, G. C., Trainor, R. F., & Pettini, M. 2018, *ApJ*, **868**, 117

Suzuki, T. L., Onodera, M., Kodama, T., et al. 2021, *ApJ*, **908**, 15

Swinbank, A. M., Papadopoulos, P. P., Cox, P., et al. 2011, *ApJ*, **742**, 11

Tacconi, L. J., Genzel, R., Neri, R., et al. 2010, *Natur*, **463**, 781

Tacconi, L. J., Genzel, R., Saintonge, A., et al. 2018, *ApJ*, **853**, 179

Tacconi, L. J., Genzel, R., Smail, I., et al. 2008, *ApJ*, **680**, 246

Tacconi, L. J., Genzel, R., & Sternberg, A. 2020, *ARA&A*, **58**, 157

Tacconi, L. J., Neri, R., Genzel, R., et al. 2013, *ApJ*, **768**, 74

Teplitz, H. I., McLean, I. S., Becklin, E. E., et al. 2000, *ApJL*, **533**, L65

Topping, M. W., Shapley, A. E., Reddy, N. A., et al. 2020a, *MNRAS*, **495**, 4430

Topping, M. W., Shapley, A. E., Reddy, N. A., et al. 2020b, *MNRAS*, **499**, 1652

Topping, M. W., Shapley, A. E., Sanders, R. L., et al. 2021, *MNRAS*, **506**, 1237

Torrey, P., Vogelsberger, M., Hernquist, L., et al. 2018, *MNRAS*, **477**, L16

Torrey, P., Vogelsberger, M., Marinacci, F., et al. 2019, *MNRAS*, **484**, 5587

Tremonti, C. A., Heckman, T. M., Kauffmann, G., et al. 2004, *ApJ*, **613**, 898

Troncoso, P., Maiolino, R., Sommariva, V., et al. 2014, *A&A*, **563**, A58

van der Wel, A., Franx, M., van Dokkum, P. G., et al. 2014, *ApJ*, **788**, 28

Vincenzo, F., Matteucci, F., Belfiore, F., & Maiolino, R. 2016, *MNRAS*, **455**, 4183

Wang, T.-M., Magnelli, B., Schinnerer, E., et al. 2022, *A&A*, **660**, A142

Weldon, A., Reddy, N., Topping, M., et al. 2022, *MNRAS*, **515**, 841

Whitaker, K. E., Franx, M., Leja, J., et al. 2014, *ApJ*, **795**, 104

Wilson, C. D. 1995, *ApJL*, **448**, L97

Wolfire, M. G., Hollenbach, D., & McKee, C. F. 2010, *ApJ*, **716**, 1191

Yates, R. M., Kauffmann, G., & Guo, Q. 2012, *MNRAS*, **422**, 215

Zahid, H. J., Kashino, D., Silverman, J. D., et al. 2014, *ApJ*, **792**, 75

Zahid, H. J., Kewley, L. J., & Bresolin, F. 2011, *ApJ*, **730**, 137